3D Ideal Linear Peeling Ballooning Theory in Magnetic Fusion Devices

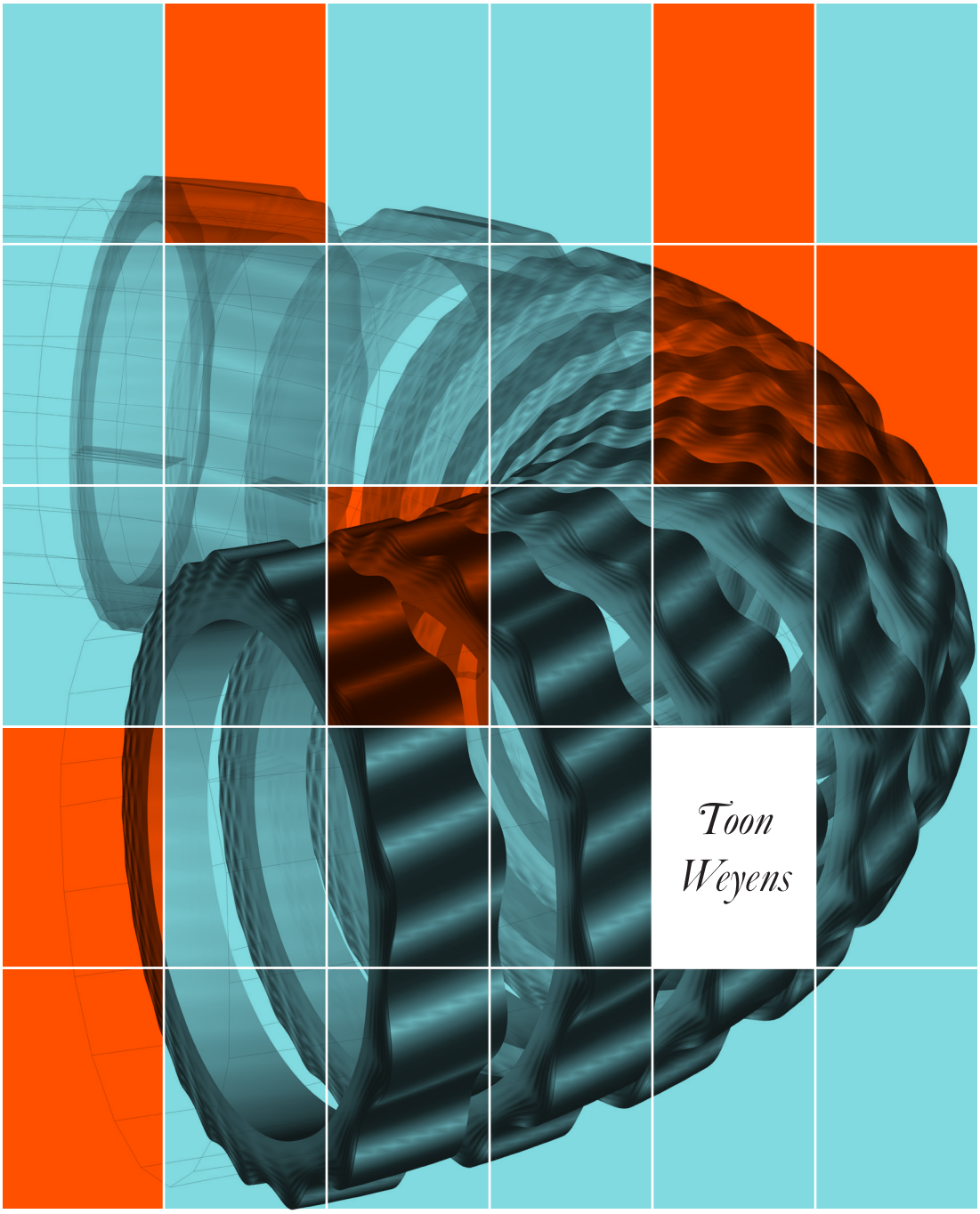

Toon Weyens

3D Ideal Linear Peeling Ballooning Theory in Magnetic Fusion Devices

This research was sponsored in part by DGICYT (Dirección General de Investigaciones Científicas y Tecnológicas) of Spain under Project No. ENE2012-38620-C02-02 and Project. No. ENE2015-68265, and also in part by EUROFUSION-WP14-EDU and through FUSENET mobility funding. This work was carried out within the framework of the Erasmus Mundus International Doctoral College in Fusion Science and Engineering (FUSION-DC). ITER is the Nuclear Facility INB no. 174. The views and opinions expressed herein do not necessarily reflect those of the ITER Organization

A catalogue record is available from the Eindhoven University of Technology Library.

Weyens, Toon
3D Ideal Linear Peeling Ballooning Theory in Magnetic Fusion Devices
Universidad Carlos III de Madrid, 2012–2016
Technische Universiteit Eindhoven, 2016
ISBN: 978-94-6233-498-4
NUR: 928

Cover: *A perturbation of the ballooning kind*
Montage by *Studio Pictobot*

Printed by *Gildeprint*

© 2016 Toon Weyens

3D Ideal Linear Peeling Ballooning Theory in Magnetic Fusion Devices

PROEFSCHRIFT

ter verkrijging van de graad van doctor aan de Technische Universiteit Eindhoven, op gezag van de rector magnificus, prof.dr.ir. F. P. T. Baaijens, voor een commissie aangewezen door het College voor Promoties, in het openbaar te verdedigen op woensdag 1 februari 2017 om 16:00 uur

door

Toon Weyens

geboren te Heusden-Zolder, België

Dit proefschrift is goedgekeurd door de promotoren en de samenstelling van de promotiecommissie is als volgt:

voorzitter:	prof. dr. ir. G.M.W. Kroesen
1e promoter:	prof. dr. ir. G.T.A. Huijsmans
2e promoter:	prof. dr. L.R. Sánchez Fernández (Universidad Carlos III de Madrid)
leden:	dr. A. Loarte (ITER Organization)
	prof. dr. L. García Gonzalo (Universidad Carlos III de Madrid)
	prof. dr. N.J. Lopes Cardozo
	dr. J.R. Martín Solís (Universidad Carlos III de Madrid)
	prof. dr. ir. B. Koren

Het onderzoek dat in dit proefschrift wordt beschreven is uitgevoerd in overeenstemming met de TU/e Gedragscode Wetenschapsbeoefening.

Summary

3D Ideal Linear Peeling Ballooning Theory in Magnetic Fusion Devices

Nuclear fusion is the fundamental process that generates heat and light in the stars but it is also a promising potential candidate for the generation of energy by man. However, where in the center of stars the combination of extreme temperatures with extreme pressure is what drives light elements close enough together for them to fuse and release part of their combined mass as energy, on earth only extreme temperatures can be employed. Matter at these temperatures exists in the state of plasma, where the atoms are stripped clean of their electrons. In the resulting physical system the presence of long term electromechanical forces between the charged particles can lead to violent collective behavior. Therefore, the general question of confining hot plasma in a stable way is crucial in order to achieve fusion. One strategy of doing this is by employing powerful magnetic fields to guide the charged particles around a toroidal configuration. This work is about a class of instabilities that these configurations are susceptible to, called high-n instabilities.

High-n instabilities are instabilities that have strong localization around the magnetic field lines that confine the plasma, and they have previously been identified as possible culprits for some significant processes that occur in magnetic configurations, such as the periodic release of energy through Edge-Localized Modes (ELMs), or even the complete loss of confinement during disruptions, during which a large amount of energy is released to the reactor walls, damaging them.

However, whereas much work has been performed in this field, the analysis of high-n instabilities in realistic 3-D geometries, including the effects of the deformation of the plasma edge, has not yet been done yet in a systematic and dedicated manner. Therefore, in the first part of this work a suitable theoretical framework is developed. Here, the simplification can be made that only modes pertaining to the same field line couple, through their high-n nature. This reduces the dimensionality of the problem by one, but at the same time does not pose any limitations on the 3-D aspects of the instabilities.

One of the results of the theory is a system of coupled ordinary differential equations that can be solved for an eigenvalue, the sign of which determines whether the mode formed by the corresponding eigenvector is unstable or not. The solution of these equations, however, is something that has to be done using numerical techniques, so to this end the numerical code PB3D is developed. This stands for **P**eeling-**B**allooning in **3**-**D**, two modes that are described well through high-n theory. PB3D can treat the stability of various equilibrium codes such a VMEC and HELENA in a modular way, is parallelized making use of the message-passing interface (MPI) and is optimized for speed. The code is verified making use of physical criteria and by comparisons with two other, well-established numerical codes that have ranges of applicability bordering on that of PB3D. The first one, MISHKA, is a general-n stability code for axisymmetric equilibria, whereas the second one, COBRA, can treat general 3-D cases, but only in the $n \to \infty$ limit, with a static edge.

The successful introduction of PB3D paves the way for a multitude of potential applications concerning 3-D edge effects. It can be investigated, for example, how many previous findings concerning peeling-ballooning modes in axisymmetric configurations change or not when 3-D effects are introduced. The theory of high-n stability of axisymmetric equilibria, for example, in the past has shed light on the dynamics of ELMs, and how this changes by including 3-D effects is a topic of interest. This is true even more so as recently the relevance of ELM control has risen due to the potentially dangerous behavior of ELMs in the next generation nuclear fusion reactors. A strategy for controlling them also intrinsically relies on applying 3-D resonant magnetic

perturbations. The study of these effects with PB3D is planned in the near future in the ITER Organization.

Before that, in this work, as a first concrete application, the modification of the stability of the pedestal of a High-confinement plasma equilibrium configuration by a toroidal field ripple is considered. These so-called H-mode configurations are characterized by a steep pressure gradient near the plasma edge, called the pedestal, which increases the temperature and pressure attainable in the core. Therefore, they are often seen as vital in order to achieve fusion. In practice, however, a degradation of the pedestal size is often observed, due to 3-D modifications of the equilibrium, such as the periodic ripple in the toroidal magnetic field due to the discreteness of the toroidal field coils. It was observed here that the application of a toroidal ripple in the shape of the poloidal cross section in the order of a percent, lead to a substantial decrease in the highest possible pedestal pressure, in the order of 30-40%. This substantiates good qualitative agreement with experimental results, where degradations of similar magnitude were observed.

Toon Weyens
2012 – 2016

Acknowledgments

This Ph.D. project has been an intensely interesting occupation for the past four and a half years, a period in which I have learned an enormous amount. However, it hasn't always been easy. I count myself lucky, therefore, that I have been surrounded by many people that have been essential in bringing it all to a good end.

I wish to thank the people at the Universidad Carlos III de Madrid for the wonderful times living in this amazing city, the folks at ITER for the unique, stimulating international environment and the colleagues at the University of Eindhoven for welcoming me into their efficient, pleasant and modern workplace.

Furthermore, I am very grateful for my supervisors: Luís García helped me through the difficult first months, and promptly set me on the right track for my research. Alberto Loarte was extraordinarily helpful and always made time for me, no matter how busy he was. I also enjoyed the daily conversations in the car as he always kindly allowed me to hitch a ride back from work. Guido Huijsmans has been invaluable in the whole project due to his expertise and the gift of his commitment. Raúl Sánchez was the one who started it all, by introducing him to the topic of 3-D edge high-n stability, giving me the opportunity to prove myself, and guiding me through it all with spectacular competence.

Apart from this, special thanks also go to Ramón Solís for his unwavering benevolence as program director, José Miguel Reynolds for the interesting conversations on all possible topics and his kind hospitality, the FUSENET staff for the formidable events, Clazien Saris, Hélène Kemperman and Toñi Rubio Cano for helping me out so many times, Karin Raijmakers for taking very good care of her kiendjes, and Niek Lopes Cardozo for the exceptional quality of his professionalism, that has taught me so

much more than I realized, and for being an exemplary, caring leader.

Finally, all of this was also supported by the fantastic family that I am lucky to have, and by my loving Mirella. I could not have done this without you.

This research was sponsored in part by DGICYT (Dirección General de Investigaciones Científicas y Tecnológicas) of Spain under Project No. ENE2012-38620-C02-02 and Project. No. ENE2015-68265, and also in part by EUROFUSION-WP14-EDU and through FUSENET mobility funding.

This work was carried out within the framework of the Erasmus Mundus International Doctoral College in Fusion Science and Engineering (FUSION-DC).

ITER is the Nuclear Facility INB no. 174. The views and opinions expressed herein do not necessarily reflect those of the ITER Organization

Table of Contents

List of Figures

List of Tables

Chapter 1

Introduction

The nitrogen in our DNA, the calcium in our teeth, the iron in our blood, the carbon in our apple pies were made in the interiors of collapsing stars. We are made of starstuff.

Carl Sagan, *Cosmos*

Of all the limited resources that humanity fights over, the fossil fuels that traditionally cover most of its energy consumption often pose the gravest issues. The fact stands that the unparalleled boom Western economies experienced during and following the Industrial Revolution in the last centuries, are for a very large part driven by traditional cycles of exploration and development of deposits of coal, oil and natural gas. Furthermore, the external costs of centuries worth of greenhouse gas emissions are only slowly becoming internalized in global decision making. To this end, traditional nuclear energy, where large and heavy ions are split by neutrons in nuclear processes, can be instrumental in mitigating greenhouse gas emissions, but ultimately it faces the same problems of scarcity of resources, though on a slower scale; as well as the additional problems of catastrophic accidents and of proliferation. Therefore, renewable energy is often championed as an inexhaustible energy source, that suffers from none of these disadvantages. However, attainable power densities are generally way below what is needed [Mac08] with worldwide consumption additionally expected even to rise sharply [IEA]. Another power source is needed.

The answer could be found by looking at the stars, where nuclear fusion processes occur. These are related to the nuclear processes employed in current nuclear fission devices, but instead of breaking up heavy nuclei, light nuclei are fused, in order to release large amounts of energy. The benefit of being able to imitate on earth these processes, is that the fuel would be virtually inexhaustible. The most feasible process envisioned on earth, for example, is the fusion of deuterium and tritium, the two heavier isotopes of hydrogen, into Helium [Fre08, Chap. 2]:

$$\mathrm{D} + \mathrm{T} \rightarrow \mathrm{He} + \mathrm{n} + 17.6\ \mathrm{MeV}\ , \tag{1.1}$$

where a neutron is liberated as well as 17.6 MeV. Deuterium can be filtered out of regular water, while tritium, which is lightly radioactive, can be formed through transmutation of lithium, abundantly available in the earth's crust, using the fast neutron. The major difficulty, however, is to overcome the strong Coulomb barrier between the positively charged nuclei of these two elements when getting them close enough together in order to fuse and convert part of their combined mass for energy. In the interior of stars it is the extreme pressure that unfailingly performs that job, but here on earth one is bound to use even more extreme temperatures, typically of the order of 100 million degrees Celsius. At these temperatures hydrogen is in the fourth state of matter where all ions are stripped clean of their electrons, called the plasma state.

Despite the formidable challenges of achieving these temperatures, scientific efforts have been very dedicated. Bridged were even the fault lines that firmly stretched across the globe when the drums of nuclear arms race still marked the rhythm of the Cold War, Soviet scientists working side by side with their Western counterparts.[1] The road has been long, initial optimism gave way to pessimism, which gave way to optimism again, and research is now nearing the metaphorical doorway behind which can be glimpsed a virtually inexhaustible source of energy, almost within reach.

This work has to be understood as a contribution in this grand research corpus oriented towards a new energy source. It is situated in the study of the *stability* of the hot plasma in the most popular confinement devices that have been invented to lock it up, called the *magnetic toroidal devices*. Naturally, any contact with a solid (or liquid, for the matter) confinement

[1] In the winter of 1969/1969, UK scientists visited their Soviet counterparts in Moscow to verify their incredible announcement that they had reached temperatures of 1keV (more than 10 million °C), using their newly-developed diagnostic device, called Thomson Scattering [Pea+69]. This was a defining moment in favor of the tokamak, championed by the Russians (see subsection 1).

box will unrelentingly damage it at the temperatures of interest for nuclear fusion, as well as degrade plasma confinement. Furthermore, as it consists of charged particles, the plasma is capable of a very rich variety of physical phenomena, so confining it in a stable way is a very tough question.

In the next section, some concepts necessary for the correct understanding of the main problem are introduced, such as an explanation concerning the toroidal devices mentioned already in the last paragraph as well as the physical models employed. Afterwards, in section 1.2 the problem is situated properly as a well-defined area inside the big picture of the stability of toroidal devices in which understanding is lacking. This paves the way for the exact statement of the problem and a breakdown of the solution employed to approach it in section 1.3. Finally, relevant research goals are stated 1.4.

1.1 Introductory Concepts

1 - Toroidal confinement devices

As a possible solution to the issue of plasma confinement, toroidal confinement devices employ powerful magnetic fields to guide the charged particles of the plasma along in donut-shaped fashion. In figure 1.1, a so-called *tokamak* is sketched, which is an (quasi-)axisymmetric device, meaning that the cross-section is an invariant of the toroidal angle (i.e. the long way around the torus). However, non-axisymmetric toroidal devices also exist, and some of the most popular variants are grouped under the term *stellarators*.

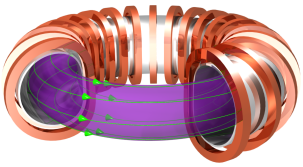

Figure 1.1
Sketch of a tokamak, a popular toroidal confinement device[2]

Both types have their advantages and disadvantages[3], but as their general confinement strategy they all use a strong magnetic field that is generated through the torus around which the particles move in spirals, called *cyclotron motion*, effectively tying them to the field lines while they are heated to the blazing temperatures at which hydrogen isotopes can fuse, in the

[2] [*source*: IPP, Dr. Christian Brandt]
[3] See for example [Sta10, chap. 4] or [Fre08, sec. 6.6].

order of hundreds of millions of Kelvin.[4] The reason why tokamaks are axisymmetric is because part of the confining magnetic field is generated through a toroidal current induced through a transformer of which the secondary winding is formed by the plasma, whereas the magnetic field coils are placed around the torus in axisymmetric fashion. Stellarators, on the other hand, create the entire magnetic field through complex 3-D coils.

The toroidal confinement scheme works well and its development is furthest advanced compared to all other confinement schemes, but it is subject to possibly violent and unstable behavior, triggered by the steep gradients that inherently exist in such physical configurations. The magnitude of the temperature gradient, for example, can be appreciated by the realization that just outside of the vessel containing the hot plasma, the toroidal field coils that generate the strong guiding magnetic field have to be cooled to temperatures close to the absolute zero, as they are made of superconducting materials for large devices, due to the large currents they support.

2 - Physical models

To reach a thorough understanding of the behavior of plasma there are multiple types of physical models that can be used. The particular model employed here is called *Magnetohydrodynamics* (MHD) and it bears resemblance to the model that results in the well-known Navier-Stokes equations used in Fluid Dynamics (FD). Though MHD is inherently more complicated than FD due to the long-range electromagnetic forces inherent to moving electrical charges, as described through Maxwell's equations, the two models both share the benefits of using a *fluid* abstraction of the behavior of the individual particles, allowing for efficient mathematical descriptions—as opposed to a *particle* treatment that keeps track of the individual characteristics of particles and is therefore more general but also more complicated.[5] The basic equations of MHD can be summarized by evolution equations for density ρ, momentum $\rho\boldsymbol{v}$, pressure p and magnetic field $\mathbf{B}$ [GP04].

It is important to note that, formally, the fluid treatment is only strictly valid in certain regions of relevant parameter space. Yet, for nuclear fusion plasmas, the results derived from MHD are often important outside their strict region of validity, the cause of which is the potent anisotropy introduced by the strong confining magnetic field, that in a sense splits the

[4] To put this number in perspective: The hottest of flames, which are also a form of plasma, only reach temperatures in the order of *thousands* of Kelvin.

[5] Through statistical methods, fluid treatments can generally be formally derived from the physically more correct particle treatments.

behavior of the plasma into behavior *parallel* to the field lines and behavior *perpendicular* to them. In fact, due to the importance of the magnetic field, in this work the words *parallel* and *perpendicular* always implicitly refer to it, unless stated otherwise. Whereas MHD is generally a poor model for the parallel plasma dynamics, it does rather well for the perpendicular dynamics, which is more important for the issue of confinement.

3 - Flux surfaces

Toroidal magnetic field configurations lead to the very important concept of *flux surfaces*. In short, as there are no magnetic monopoles, the magnetic field lines trace out lines on nested surfaces in the torus. Except for the degenerate case where the magnetic fields close *exactly* on themselves after a number of turns around the major axis of the torus, the flux surfaces can be assumed to be covered by them.[6] Therefore, it can be assumed that a magnetic field line pertaining to a flux surface can never leave it in ideal MHD, as for this resistive effects are necessary.

Subsequently, the whole concept of flux surfaces provides another way of looking at magnetic toroidal confinement, as the plasma particles are constrained to follow the field lines through their cyclotron motion and hence stay in the flux surfaces.

Clearly, however, this is an idealized picture, as effects such as particle drifts and non-linearities such as collisions between particles and particle-field interactions indeed lead to movement across the flux surfaces. Movement across flux surfaces can be modeled in a variety of ways, ranging from a simple diffusion approximation, to fractional diffusion, to full-turbulence descriptions. However, these are not in the scope of this work and henceforth, the concept of nested flux is used and the direction normal to the flux surfaces is called the *normal direction*.

4 - Scale analysis & Linearization

From a mathematical standpoint, the equations obtained through fluid treatments, such as MHD or ordinary FD, reduce to a coupled system of differential equations, generally nonlinear and challenging to analyze directly. Therefore, one often uses the complementary approaches of *scale analysis* and *linearization* of said equations. The former technique is geared towards getting the most out of an analysis while using the least complicated means possible, by identifying the dominant terms in the equations, so that increasing accuracy comes at additional cost. In phenomena that vary slowly relative to light speed, for example, the current displacement

[6] The question of whether they are covered ergodically can be analyzed through so-called KAM theory, named after the initials of its designers; see for example [LL83].

term in Maxwell's equations can be neglected. Furthermore, a parameter can be introduced, to benefit important terms for a certain class of problems and disregard the others, as is done in chapter 3. The latter technique, on the other hands, gets rid of non-linearities by looking at small *perturbations* of steady-state situations, *equilibria*, the advantage of which is that it allows one to tap into the vast reserve of mathematical techniques for linear models, a very mature subject.

Specifically, in this work, the perturbations (subscripts 1) of equilibria (subscripts 0) are described using the perturbation vector $\boldsymbol{\xi}(\mathbf{r}, t)$ as a function of time t and space $\mathbf{r}$, defined through the relation

$$\frac{d\boldsymbol{\xi}}{dt} = \boldsymbol{v}_1 \,, \tag{1.2}$$

where $\boldsymbol{v}_1(\mathbf{r}, t)$ is a small perturbation of the velocity $\boldsymbol{v}(\mathbf{r}, t)$ of the plasma, superimposed on the equilibrium velocity $\boldsymbol{v}_0(\mathbf{r})$:

$$\boldsymbol{v}(\mathbf{r}, t) = \boldsymbol{v}_0(\mathbf{r}) + \boldsymbol{v}_1(\mathbf{r}, t) \,, \tag{1.3}$$

where for the static equilibria chosen here, $\boldsymbol{v}_0 = 0$. Employing these plasma perturbations, the MHD equations can be combined into a fluid equivalent of Newton's second law:

$$\rho_0 \frac{\partial^2 \boldsymbol{\xi}}{\partial t^2} = \mathbf{F}\left(p_1(\boldsymbol{\xi}), \mathbf{B}_1(\boldsymbol{\xi}), \rho_1(\boldsymbol{\xi})\right) \,, \tag{1.4}$$

where the *force operator* $\mathbf{F}$ depends on the perturbed pressure, magnetic field and density, but not on time.

5 - Normal Modes & Eigenvalues

For equations such as equation 1.4, an additional mathematical technique called *normal mode analysis* is of interest, where one looks at perturbative motion resulting from a harmonic excitation, described through a complex phase as:

$$\boldsymbol{\xi}(\mathbf{r}, t) = \boldsymbol{\xi}(\mathbf{r})\, e^{-i\omega t} \,, \tag{1.5}$$

where in the remainder of this work, the time-invariant $\boldsymbol{\xi}$ on the right-hand side is employed, but possible confusion concerning the symbols can unequivocally be avoided by explicitly stating the independent variables.

As the term *normal* implies, the results for harmonic excitations of different complex frequencies ω are decoupled for linear systems and therein lies the strength of the approach: each normal mode is orthogonal to the others and can be investigated individually. This then leads to the familiar concept of *eigenvalues* and corresponding *eigenvectors* through the translation of the time-derivatives into multiplications by factors $i\omega$. In particular, as the order of the time-derivative in equation 1.4 is two, a factor $-\omega^2$ appears.

6 - Extended energy principle

A final ingredient necessary is the *Extended Energy Principle* [GP04, sec. 6.6], which uses normal modes of ideal linear MHD to treat toroidal devices as the union of a plasma region surrounded by a vacuum that is supposed to decay at infinity. Here, *ideal* implies that there are no loss-terms and *linear* refers to the linearization process mentioned above. The surface between plasma and vacuum, also called the edge, can in principle support a jump in the tangential magnetic field through a skin current. Note that the perpendicular magnetic field is zero at the surface, as the magnetic field lines have to lie in magnetic flux surfaces by definition. As the name implies, the Extended Energy Principle, through the combined system of plasma and vacuum, is an extension of the Energy Principle introduced in [Ber+58], which at its turn can be understood as a particular way of stating stability theory, similar to the way it is done in Quantum Mechanics.

1.2 Situation

1 - Linear ideal high-n modes

The study of stability of plasmas, being a subject of considerable importance due to the potential for (costly) damage to reactor vessel walls from being exposed to plasma of temperatures far above sublimation temperatures of solids if confinement is not perfect, has received ample interest.

However, in the general stability picture there exists an important possibility of using a promising different approach in the subclass of so-called *high*-n modes, which can be described appropriately through ideal linear MHD. High-n modes, also called *short wavelength* modes, are normal modes described through *perturbative* analysis of MHD equilibria, where a difference of scale is introduced through this large number $n \gg 1$. This means that the modes have a spatial structure that varies quickly as compared to the length scales of the equilibrium. However, basic stability considerations lead to the observation that for rapidly varying modes to be unstable, they should nevertheless vary on equilibrium scales *along* the magnetic fields, leading to the concept of *fluted* modes [Fre87, sec. 8.11], illustrated in figure 1.2.

The main reason why the stability of high-n modes is important, is the fact that they are angularly localized and therefore have low inertia, so that they are easily excited by the sources of free energy in the plasma (the steep gradients mentioned previously). Simultaneously, they can have a rather extended radial mode structure throughout the plasma, so they are able to couple energy from the hot core to the (comparatively) cold walls [GJ68, sec. 7].

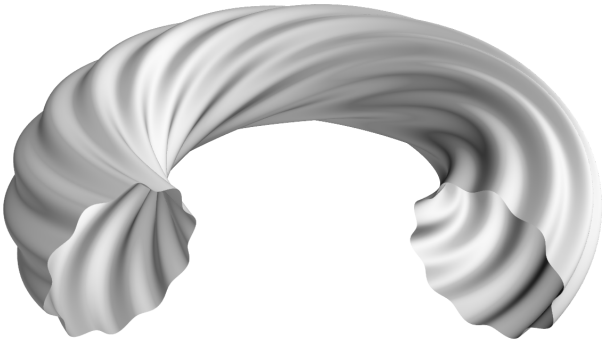

Figure 1.2
Sketch of a fluted perturbation of a toroidal surface, elongated along magnetic field lines that spiral around the torus, in this case they go once round toroidally for every poloidal turn.

The new approach in the high-$\mathfrak{n}$ stability picture in which this work is situated will be the topic of the next section. However, before getting to it, the situation is explored in more detail here, from a historical point of view.

2 - Eikonal mathematics

In the framework of linear ideal MHD the separation of scales can be expressed by use of an *eikonal formulation* for the perturbation $\boldsymbol{\xi}(\mathbf{r})$ of the form [CHT79]:

$$\boldsymbol{\xi} = \hat{\boldsymbol{\xi}} \exp(\mathrm{i}\mathfrak{n}S) , \tag{1.6}$$

where $\mathfrak{n} \gg 1$ and $S(\mathbf{r})$ is the eikonal, defined through the relation:

$$\mathbf{B} \cdot \nabla S = 0 , \tag{1.7}$$

where $\mathbf{B}(\mathbf{r}) \approx \mathbf{B}_0(\mathbf{r})$. Indeed, employing this assumption, the parallel and perpendicular dynamics enter at different orders:

$$\begin{aligned} \nabla_\parallel \boldsymbol{\xi} &= \left(\nabla_\parallel \hat{\boldsymbol{\xi}}\right) \exp(\mathrm{i}\mathfrak{n}S) && \sim \mathcal{O}(1) , \\ \nabla_\perp \boldsymbol{\xi} &= \left(\nabla_\perp \hat{\boldsymbol{\xi}} + \mathrm{i}\mathfrak{n}\nabla_\perp S \cdot \hat{\boldsymbol{\xi}}\right) \exp(\mathrm{i}\mathfrak{n}S) \\ &\approx \mathfrak{n}\left(\mathrm{i}\nabla_\perp S \cdot \hat{\boldsymbol{\xi}}\right) \exp(\mathrm{i}\mathfrak{n}S) && \sim \mathcal{O}(\mathfrak{n}) , \end{aligned} \tag{1.8}$$

where the subscripts $_\parallel$ and $_\perp$ refer to the parallel and perpendicular components, respectively.

When, additionally, certain judicious orderings are assumed for the envelope function $\hat{\boldsymbol{\xi}}$ as a function of the perpendicular coordinates, the separation of parallel and perpendicular derivatives of the eikonal carries on to a separation of the ideal linear MHD stability equations. The lowest-order equation then contains information of only the eigenvalues $\lambda = \omega^2$ that appear through the use of the normal modes as explained at the end of section 1.1. It can then be understood that the stability of the normal modes

is determined by the sign of λ, a positive λ implying an infinitely oscillating solution through a real ω and a negative λ an exponential solution through an imaginary ω. Finally, the envelope is determined by the higher orders.

3 - Ballooning & Peeling modes

Originally, for *axisymmetric bulk* cases—meaning modes that are far from the plasma edge and pertain to equilibria that have a symmetry in the toroidal direction[7]—it was found that assuming a certain[8] ordering leads to Gaussian envelope shapes [CHT79, eq. 37]. In later work, the important *edge* situation was approximated using a different[9] ordering, leading to Airy functions for the envelope instead of Gaussians [Con+98, eq. 59]. By this is meant that the edge of the plasma itself can be perturbed, which implies a perturbation of the surrounding system. The modes described through these assumptions are often referred to as *ballooning modes* and the lowest-order equation describing its stability as the *ballooning equation*.

Independently of these ballooning modes, in [Lor75], a whole different class of modes was described, which have a different structure[10] and crucially depend on the existence of a rational surface just outside of the plasma edge, meaning a flux surface where $q = \frac{m}{n}$. For these modes, called *peeling modes*, edge effects are clearly always important.

The subject of peeling as well as ballooning modes is at the core of this work and explored in more detail in the next chapters.

4 - 3-D Eikonal approach

Though the ballooning modes of the previous subsection were investigated in axisymmetric equilibrium situations, general considerations concerning the eikonal approach are valid in 2-D (i.e. axisymmetry) as well as in 3-D. In [Cor82a], for example, results are given for general 3-D cases. Subsequently, numerical codes such as COBRA [Sán+00] and a specific module of TERPSICHORE [And+91] were designed, that can solve for the ballooning stability of the flux surfaces of 3-D configurations using the eikonal approach.

In contrast, the peeling-theory put forth by [Lor75] was already inherently 3-D, but thanks to the strong normal localization of the modes, the resulting equations are less involved than for ballooning modes. These equations correspond, in fact, to an extended *Mercier criterion*, which is a simple criterion for (in)stability of interchange modes making use of quantities

[7] Note that in this work the term "axisymmetry" always refers to the equilibrium of which stability is calculated—the perturbations are generally 3-D.

[8] The normal dependence of the mode envelopes are to vary on the scale $\sim \mathcal{O}\left(n^{1/2}\right)$.

[9] The normal variation is then on the scale $\sim \mathcal{O}\left(n^{2/3}\right)$.

[10] The normal variation is now extra fast, on the scale $\sim \mathcal{O}\left(n^{2}\right)$.

integrated over the flux surfaces [Mer60], similar to the Rayleigh-Taylor instability in non-magnetized fluids.

5 - Troubling eikonals

Apart from its apparent theoretical utility, however, there are three serious problems with using eikonal theory.

First of all, though it is not very difficult to design an acceptable eikonal that satisfies the necessary requirement that $\mathbf{B} \cdot \nabla S = 0$, the condition for periodicity in poloidal and toroidal angles is then lost in general. Mathematical tools exist to reintroduce periodicity. For example, the eikonal representation can be interpreted as an integral transform, similar to the Fourier and Laplace transforms, that removes the periodicity constraints of physical solutions, so that on the infinite domain the mathematical problem is simplified [HN90]. However, for the inverse transformation, called the *ballooning transform*, to exist, the requirement is placed on the solutions in ballooning space to have limited bandwidth in the normal direction. In other words, for any given mode number n, above mode amplitudes $\hat{\xi}$ need to be nearly constant across neighboring rational flux surfaces.

Apart from these considerations concerning the reconstruction of the physical solution, the ability to have more arbitrary mode shapes of the envelope is lost when an eikonal description is employed with an assumed ordering of the envelope. This is a very important limitation since the theoretic cases are but limit cases. A mode can, for example, exhibit features of both ballooning and peeling modes, but does not necessarily have to be one of the two.

Finally, the correct treatment of the modes at the plasma edge is another element that requires a more elaborate study than the theoretical orderings described above that lead to mode envelopes of the shape of the Airy function. Also here more general possibilities are required.

6 - Fourier theory

As an alternative, in order to avoid the difficulties associated with the eikonal treatment described above, general Fourier modes can always be used. The price to pay in this case is the increase of complexity[11] of the resulting equations. In particular, the neat decoupling of the problem in an equation that describes the eigenvalue and higher-order equations that describe the envelope is then impossible. Instead, the theory yields coupled equations for the different flux surfaces, however still containing an eigenvalue. As a consequence, analytic solutions of these equations becomes

[11] The term *complexity* refers to "having many components" and is not necessarily related to the notion of *complicated* that refers to "difficulty", though in this case it probably is.

difficult and one has to resort to computational techniques.

7 - Axisymmetric ELITE

The Fourier treatment, making use of the extended energy principle, combined with numerical solutions constituted the philosophy behind the numerical code *ELITE* [Wil+02] that, though still employing the condition of axisymmetry of the equilibrium of which it calculates stability, does away with the eikonal of the theoretical approach and uses Fourier modes instead for the calculation of high-n stability. As a consequence of using Fourier modes, the results that can be described using ELITE are of a more general nature, though the ballooning and peeling (un)stable regimes can still be identified.

ELITE has contributed to the explanation of a variety of phenomena in axisymmetric toroidal configurations, such as identifying certain types of *Edge Localized Modes* (ELMs) as a periodic cycling between the two regimes. ELMs are periodic outburst of energy regularly observed in the so-called *High-confinement* (H-mode) regimes[12] of modern tokamaks, which can be approximated using axisymmetry, and their control is of great importance, as next-generation devices they may be quite detrimental to both the confinement and the device [Loa+14]. In fact, a promising tool to control ELMs is the usage of helical windings called perturbation coils, which locally break axisymmetry through *resonant magnetic perturbations* (RMPs) and thus driving the ELMs unstable before they have a chance to grow big [Eva+06]. Ironically, much of the research concerning this is done using axisymmetric codes, while their utility depends on them being inherently 3-D.

1.3 This work: A different approach

The new approach in the high-n stability picture mentioned in the beginning of the previous section can now be specified further. It is situated in the *general 3-D high*-n ideal linear MHD stability *valid for edge situations*.

Part of this approach, as explained in the previous section, lies in not using an eikonal treatment, as periodicity is a nontrivial issue; as they are not generally valid near the edge of plasmas; and since for them to be useful, a certain ordering in the normal localization of the normal modes must be assumed. In this work, as in the ELITE philosophy, a Fourier description

[12] The H-mode was a great improvement compared to the previous *L-mode* (L-mode) regime, and is nowadays seen as a necessary condition for success.

Table 1.1
Situation of current work (in gray) within previous high-n work. Whereas bulk treatment are only valid far from the edge, edge treatments are free to move it.

2-D equilibrium	
bulk	*edge*
eikonal theory [CHT79]	eikonal theory [Con+98] Fourier ELITE [Wil+02]
3-D equilibrium	
bulk	*edge*
eikonal theory [Cor82a]	Fourier theory [Wey+14]
eikonal COBRA [Sán+00]	Fourier **PB3D** [Wey+16]

of the modes is used instead. This enables the theory to take into account correctly the influence of edge effects and surrounding vacuum. A second part of the approach used in this work, and in contrast with ELITE, is that the entire treatment is done in 3-D. Therefore, when the equilibrium configurations are restricted to axisymmetry, the domain of validity of ELITE is recovered, but it is much wider in general. Table 1.1 gives an overview of this work in relation to previous high-n work.

Before information concerning the work plan is stated in the subsections 2, 3 and 4 below, it is important to look at the justification and motivation in subsection 1. The work described in the work plan is done as the doctoral project of the author, supervised by *prof. Dr. Raúl Sánchez* from the *Universidad Carlos III de Madrid* and *prof. Dr. Guido Huijsmans* from the *Eindhoven University of Technology*, but part of the work is performed at the *ITER organization* at Cadarache, in collaboration with *Dr. Alberto Loarte*. Furthermore, *prof. Dr. Luís García* from the Universidad Carlos III de Madrid acts as an additional supervisor. Finally, in subsection 5, some short information is given about other codes of interest, some of which are referred to later in this document.

1 - Justification & motivation

As explored in table 1.1, the treatment of 3-D edge situations is indeed the last piece missing in the high-n picture, probably due to the tedious work it requires. But clearly, the inherent aesthetic beauty of completing a puzzle is not the reason why this research is important. However, beside the fact that unknown topics should be investigated before they are concluded to be important or not, there are aspects of 3-D edge high-n stability that

result in expected relevance.

First of all, it should be recalled that peeling-ballooning modes, described through edge high-n theory, are of interest since they are easily excited but have the capacity for detrimental coupling of hot core power to the cold device walls. Indeed, the results from axisymmetric codes hint that the stability boundaries are clearly relevant to phenomena such as ELMs. However, there are many non-axisymmetric effects, such as the *helical perturbation coils* that deliberately break axisymmetry in order to control these ELMs, ferritic *Test-Blanket modules* (TBM) for tritium breeders and *toroidal field ripple* due to the discreteness of the toroidal field coils. As a side note it should be stated that, generally, the further away from the plasma core and the closer to the plasma edge, the more important 3-D effects become as the axisymmetric approximation holds less and less.

Apart from the configurations with imperfect or broken axisymmetry, there is also the very important class of inherent 3-D configurations, such as *stellarators*, that needs full 3-D studies. It is clear, also, that these studies too must include the effects of the edge, not only for the peeling modes that are inherently dependent on the detailed edge situation through the presence of an important rational surface just outside the edge, but also for edge ballooning modes, that can be modified by the edge.

Note that these two aspects can be thought of as moving in the vertical, respectively the horizontal direction in table 1.1, towards the bottom-right.

2 - High-n 3-D edge theory

The 3-D treatment pursued in this work is performed by not making the common assumption of axisymmetry on the plasma equilibrium whose stability is investigated. This then leads to more involved expressions, relying on tensorial calculus in curvilinear coordinates, as opposed to the pseudo-Cartesian treatment that can be applied to 2-D equilibria. However, by employing a modified flux coordinate system, which will be explained in the next chapter, as well as the high-n assumption on the modes, the anisotropy introduced by the magnetic field lines can be readily exploited in order to reduce the dimensionality of the problem by one. This means that, perhaps surprisingly, the final problem to be solved is mathematically of the *same complexity* as the axisymmetric problem. Actually, it just a consequence of the fluted nature of the modes.

Deriving this high-n 3-D edge theory is the first major task of this work, and it is presented in chapter 3.

3 - the PB3D numerical code

A suitable result of the theoretical derivations of the 3-D ideal linear MHD stability will consist of a coupled set of ordinary differential equations of second order, containing an eigenvalue. The solution thereof is done using numerical techniques, for the equilibrium configurations provided by certain equilibrium codes. A new numerical code **PB3D**, which stands for **P**eeling-**B**allooning in **3**-**D**, is developed, that performs this.

It is then important to verify whether the PB3D code performs its task well. This is done by comparing results with established codes, both for the stability of an axisymmetric equilibrium as well as a 3-D equilibrium.

Developing and verifying PB3D is the second major task of this work, and it is presented in chapter 4.

4 - 3-D edge application

The PB3D numerical code can then be employed for a great deal of situations, as stated above. In this document a first application is explored. It is chosen to investigate what is the influence of a toroidal field ripple on the ideal linear edge stability, as this is quite an important and realistic problem.

Providing a first real application of PB3D is the third major task of this work, and it is presented in chapter 5.

5 - Other codes

Finally, it should be noted that there are also a large zoo of numerical codes that investigate MHD stability in more general situations, without employing the high-n assumption, referred to here as *general codes*. General codes enjoy the benefit of being able to investigate the entire spectrum, where high-n codes are specifically tuned to the unstable side, as it are the unstable modes that behave according to it. This generality can also make them less fast than codes such as PB3D that are specialized for the specific goal of investigating instabilities, like the relevant peeling-ballooning instability. The following short and not exhaustive list of other codes is given:

- **CASTOR** is an axisymmetric linear code that additionally contains non-ideal resistive effects [Ker+98]. It uses the Galerkin method to approximate the spectrum to arbitrary precision.
- **MISHKA** is related to CASTOR that has been much optimized for speed but that does not include resistive effects [Mik+97].
- **CAS3D** is an extension of CASTOR for non-axisymmetric equilibria, used extensively for the design of stellarators [Sch93].

- **TERPSICHORE** made use of the Cray architecture of the 1990's to perform non-axisymmetric linear stability analysis [And+90].

- **JOREK** does not employ the scale separation between equilibria and their stability, but instead evolves the MHD equations, in non-linear fashion [HC07]. The stability of the configuration is then expressed by a profile that evolves to a stable configuration. Furthermore, it has the advantage of being able to simulate the non-linear regimes that occur afterwards.

1.4 Research Goals

The information from the previous sections leads directly to some questions that are to be answered in the scope of this work: The overall research goal that motivates this work can be stated as follows:

Main Issue *Assess the importance / the effect of 3-D effects on MHD stability in magnetic fusion devices.*

In order to address this, the construction of a theoretical framework will be investigated, based on the concept of high-n MHD stability:

Question 1 *How can the ideal high-n MHD stability be theoretically described for fully 3-D equilibria while allowing for edge effects?*

Having finished this endeavor, the next step will be to build a code, which will be called PB3D (**P**eeling-**B**allooning in **3**-**D**), that solves the equations resulting from the theory in a numerical way:

Question 2 *What is an efficient way of implementing this stability theory in a numerical code?*

Question 3 *How does PB3D compare to other codes in terms of verification and validation?*

Finally this numerical implementation of the 3-D stability theory is to be applied to an important example of axisymmetry breaking in a tokamak, as a first proof of principle:

Question 4 *What is the influence of a toroidal ripple on the stability boundaries of a realistic tokamak, from the ideal linear stability point of view?*

Question 1 is answered in chapter 3, questions 2 and 3 in chapter 4 and question 4 in chapter 5. Finally, proposed for further work, the following

examples can then be given:

Suggestion 1 *Apart from toroidal ripple, what happens with the modification of ideal linear edge stability by other kinds of 3-D perturbations, such as RMP coils? Specifically, what is the importance of the actual shape of the 3-D modification?*

Suggestion 2 *Are there any extra (un)stable regions of parameter space that exist for 3-D equilibria, similar to the regions defined by peeling and ballooning stability for axisymmetric cases?*

The numerical tool PB3D will provide a tool specifically tailored to attack these problems.

1.5 Document Structure

This introductory chapter is followed by chapter 2, which gives a very concise overview of the relevant known theory in the field, up to an explanation of the energy principle.

Afterwards, chapter 3 contains the first original work, treating the theory concerning 3-D high-n ideal linear MHD for Peeling-Ballooning normal modes in more detail. As stated in the previous section, a suitable result of this theory is a system of ordinary differential equations of second order that can be solved for an eigenvalue which corresponds to the time behavior of the perturbation.

Subsequently, in chapter 4, the numerical solution of this system of equations is discussed through the new code PB3D, including the technique of discretization used and the general strategies employed. Also, the issue of verification is treated, through comparison to established numerical codes as well as physical considerations.

After this, chapter 5 is concerned with the first application of PB3D to a real application of physical interest, namely the investigation of the modification of the ideal linear edge stability boundary due to a toroidal field ripple in a realistic tokamak geometry.

To conclude, the work is evaluated and discussed shortly in chapter 6.

Chapter 2

Overview of Theory

To describe the behavior of a hot plasma theoretically, many different degrees of abstraction can be used, each with its own assumptions and simplifications, which result in a certain complexity and domain of physical validity.

Of interest to this work is the Magnetohydrodynamical (MHD) viewpoint, which treats plasma as a fluid in a way similar to that used in ordinary fluid dynamics. More specifically, the extended energy principle is used, which is built from MHD theory. This will therefore be the end point of this chapter. To get a more complete overview, however, the steps that lead to the theory of MHD are also worth having a look at, starting from the most elementary approach where the plasma particles are described individually, and building up abstraction step by step, making assumptions on the way, and necessarily shrinking the domain of validity. Note that, clearly, there is no pretension of rigor, as the only goal is to give an overview which can be helpful to understand the rest of this work.

In a first section, the steps leading from a fundamental particle picture of the plasma to a statistical one through the *Boltzmann equation* are considered. Afterwards, in section 2.2, the topic of interest is the mathematical procedure of taking moments to perform averaging of velocities in order to get to a *fluid description* of the plasma. Subsequently, section 2.3 treats further simplifications that allow for a description of the plasma with a single fluid, such as the description with *MHD*. Finally, using MHD, in section 2.4, the extended energy principle is explained.

2.1 The Boltzmann equation

When a gas is heated sufficiently, at some point it experiences a change of state, transitioning to plasma. Ideally, in a plasma all the atoms are stripped clean of their electrons. However, in contrast to these so-called *hot plasmas*, there exists a continuum in the degree of ionization, described through the *Saha ionization equation* which results from quantum mechanics [Fri08].

1 - Liouville's theorem

The isolated whole of N plasma particles, with N an arbitrary number, can be described using Hamiltonian mechanics through *Liouville's theorem*, which works in *phase space* [Har04]. This is the mathematical space that consists of $6N + 1$ dimensions: 3 for the physical position of each particle in space, 3 more for its velocity, and 1 for time. Using the concept of the distribution function f^N for N particles that describes the probability of finding a particle at a certain position and with a certain velocity, denoted by

$$f^N\left(\mathbf{r}_1, \mathbf{r}_2, \ldots \mathbf{r}_N, \boldsymbol{v}_1, \boldsymbol{v}_2, \ldots, \boldsymbol{v}_N\right) , \tag{2.1}$$

Liouville's theorem describes the preservation of this distribution function in time:

$$\frac{df^N}{dt} = \frac{\partial f^N}{\partial t} + \sum_{i=1}^{N} \left(\boldsymbol{v}_i \cdot \nabla_{\mathbf{r}_i} f^N + \frac{\partial \boldsymbol{v}_i}{\partial t} \cdot \nabla_{\boldsymbol{v}_i} f^N \right) = 0 , \tag{2.2}$$

where the subscript denotes the variables in which the nabla operator works.

2 - BBGKY hierarchy

To reduce complexity, integrations are done on the complete $(6N + 1)$-D distribution function. To this end, the *reduced distribution functions*

$$f^r\left(\mathbf{r}_1, \boldsymbol{v}_1\right) = \int f^N \, d\boldsymbol{x}_{\mathbf{r}+1} \, d\boldsymbol{x}_{r+2} \ldots d\boldsymbol{x}_N \, d\boldsymbol{v}_{\mathbf{r}+1} \, d\boldsymbol{v}_{r+2} \ldots d\boldsymbol{v}_N , \tag{2.3}$$

are introduced, that describe the probability of finding r particles in a particular point of phase-space. The so-called *BBGKY*-hierarchy is then followed, which is named after its inventors. It is called a hierarchy as through performing integrations on the full distribution function f^N, it yields equations that link the ascending reduced distribution functions f^r to each other.

3 - Boltzmann and Vlasov closure

To be of a practical form, therefore, this system needs to be cut at some point and here a first assumption is made. This procedure is called *closure* and the result is an equation of the form

$$\frac{\partial f}{\partial t} + \boldsymbol{v} \cdot \nabla_{\boldsymbol{r}} f + \boldsymbol{a} \cdot \nabla_{\boldsymbol{v}} f = \left(\frac{\partial f}{\partial t}\right)_{\text{coll}} \tag{2.4}$$

where now the superscript 1 is left out in $f \equiv f^1$ and $\boldsymbol{a}$ is the acceleration. The right-hand side describes the force due to collisions and multiple forms of various exist of complexity are possible. This equation is called the *Boltzmann equation*. Note that not considering higher orders of reduced distribution functions implies that the influence a particle has over another is limited, that they behave rather independently.

Finally, if the system can be assumed to be collisionless, the Boltzmann equation reduces to the Vlasov equation:

$$\frac{\partial f}{\partial t} + \boldsymbol{v} \cdot \nabla_{\boldsymbol{r}} f + \boldsymbol{a} \cdot \nabla_{\boldsymbol{v}} f = 0 \,. \tag{2.5}$$

The theory of the Boltzmann and Vlasov equations is often called *kinetic theory* as velocity space is still an independent variable. These equations much simpler than the original Liouville equations, but they are still $(6+1)$-dimensional. This means that there is a wide area of applicability where many simplifications can still be made.

2.2 Fluid descriptions

1 - Taking moments

To further simplify the kinetic description of the plasma, where velocity is still an independent variable, mathematical moments of the distribution function f are taken [Bel08]. These are integrals over velocity space of powers of the velocity. The first few are, for example, the particle density n_α and the average velocity u_α:

$$n_\alpha = \int f \, d\boldsymbol{v} \,, \tag{2.6}$$

$$\boldsymbol{u}_\alpha = \int \boldsymbol{v} f \, d\boldsymbol{v} \,, \tag{2.7}$$

but there exist infinitely many. Not all, however, have clear physical meaning such as the two above. Note that now the subscript α has been used to avoid confusion with the reduced distribution function terminology of order

i: α refers to a particular species here, either a particular ion type or the electrons.

Integrating the moments of the Boltzmann or Vlasov equation over velocity space, an infinite number of equations is yielded, each connecting a particular moment to moments of a higher order, similarly to the BBGKY hierarchy, where equations coupled reduced distribution functions of different orders. Again, to be practical, these equations have to be cut at some point, and closed using physical assumptions. The result is then a series of equations that describe the time-evolution of the different moments of the distribution function.

2 - Deviations away from equilibrium

In practice, closure is normally done after taking the moments of just 1, $\boldsymbol{v}$, v^2, yielding a continuity equation, a momentum equation and an energy equation, respectively. Furthermore, splitting off the average part of the velocity, which results in quantities $\boldsymbol{v}_\alpha = \boldsymbol{v} - \boldsymbol{u}_\alpha$, is often useful to get to a closure formulation as it helps to consider deviations f^i ($i > 0$) of the distribution function away from the Maxwellian form [GP04]:

$$f_\alpha^0 \propto \exp\left(-\frac{m_\alpha v_\alpha^2}{2kT_\alpha}\right), \tag{2.8}$$

where k is the Boltzmann constant and m_α is the mass and T_α the temperature of species i, defined to be proportional to the average value of $\boldsymbol{v}_\alpha$:

$$T_\alpha = \frac{m_\alpha}{3k}\left\langle v_\alpha^2 \right\rangle . \tag{2.9}$$

Since the Maxwellian distribution is the state of a system at thermal equilibrium, as is known from statistical physics, it is the state towards which a distribution function tends to evolve. Considering the deviations thereof are therefore of physical interest for closure. This is where the collision force comes into play, as appropriate expressions must be designed to link these to lower-order moments. The most known set of equations is called the Braginskii equations [Bra65], and they are used often in numerical codes, such as B2 [RBB05]. Note that in order for the plasma to evolve towards the Maxwellian equilibrium, its particles must experience sufficient collisions as a necessary relaxation process.[1] In other words: fluid descriptions imply slow time scales or high-collisionality.

[1] As stated in chapter 1, this is not completely true: In the case of magnetic nuclear fusion plasmas, the anisotropy introduced by the strong magnetic field tends to take the role of collisions to thermalize the plasma.

To recapitulate, the end result of taking moments of the Boltzmann or Vlasov equation, combined with appropriate closure to limit the number of equations, sets of equations can be obtained that describe the plasma in terms of its individual fluids or species, such as electrons and various ion types. These take the form of evolution equations that describe the time evolution of macroscopic plasma quantities such as density, momentum and temperature, depending on the closure. Often, however, having multiple species in the description of the plasma contains still a lot of information. In this case, there exists the possibility to simplify things and to go to a single-fluid description, of which MHD is one very often used possibility.

2.3 Magnetohydrodynamics

A single-fluid description can be derived from a multi-fluid description by making additional assumptions. More exactly, another assumptions is made considering the length scales in the plasma [GP04], on top of the assumptions of independent particles for the Boltzmann or Vlasov description of section 2.1 and of slow time scales or high-collisionality for the multi-fluid models of section 2.2.

1 - Quasi-neutral ideal plasma

In MHD, the length scales considered must be of sufficient size for the plasma to be quasi-neutral; i.e. they must be *macroscopic*. By this is meant that any local imbalance in the ratio between positive charges due to ions and negative charges due to electrons, at least for non-exotic plasmas, is quickly balanced by the movement of the agile small electrons. Furthermore, this also means that the cyclotron motion of charged particles around a magnetic field line, described in section 1.1 is averaged out in time on MHD time- and length scales.

Subsequently, in this work *ideal MHD* is used, which is a statement about the conductive properties of the plasma. It means that the plasma resistivity is so low that any resistive effect unfolds on time scales much slower than the ones interested in. At high temperatures, this is an easy condition to satisfy, as plasma resistivity drops to very low values.[2]

[2] So low, in fact, that it seems to be next to impossible to achieve plasma fusion with only Ohmic heating; i.e. heating that that occurs by driving a current through the plasma.

2 - MHD equations

The resulting system of ideal MHD equations now take the much more manageable form:

$$\frac{\partial \rho}{\partial t} + \nabla \cdot (\rho \boldsymbol{v}) = 0 \,, \tag{2.10}$$

$$\rho \left(\frac{\partial \boldsymbol{v}}{\partial t} + \boldsymbol{v} \cdot \nabla \boldsymbol{v} \right) + \nabla p - \rho \nabla \Phi - \frac{1}{\mu_0} (\nabla \times \mathbf{B}) \times \mathbf{B} = 0 \,, \tag{2.11}$$

$$\frac{\partial p}{\partial t} + \boldsymbol{v} \cdot \nabla p + \gamma p \nabla \cdot \boldsymbol{v} = 0 \,, \tag{2.12}$$

$$\frac{\partial \mathbf{B}}{\partial t} - \nabla \times (\boldsymbol{v} \times \mathbf{B}) = 0 \,, \tag{2.13}$$

with Φ the gravitational potential, γ the adiabatic constant, μ_0 the vacuum permeability and $\mathbf{B}$ the magnetic field. Furthermore, the density ρ, momentum $\rho\boldsymbol{v}$ and pressure p are average values of all the plasma species:

$$\rho = \sum_{\alpha} n_\alpha m_\alpha \,, \tag{2.14}$$

$$\rho \boldsymbol{v} = \sum_{\alpha} \mathbf{u}_\alpha n_\alpha m_\alpha \,, \tag{2.15}$$

$$p = \sum_{\alpha} p_\alpha \equiv n_\alpha k T_\alpha \,, \tag{2.16}$$

with $m_\alpha, n_\alpha, \mathbf{u}_\alpha$ and T_α defined in the previous section. Note that Maxwell's equations were used in the closure, as can be seen in the appearance of terms such as $\frac{1}{\mu_0}(\nabla \times \mathbf{B})$.

2.4 The extended energy principle

1 - Normal modes

The ideal MHD model is now complete and ready to be used. This last section describes one of its applications, the extended energy principle. As stated in chapter 1, the extended energy principle is constructed from through performing normal mode analysis on the linearized ideal MHD equations. This means that the plasma is assumed to be perturbed from an equilibrium state by harmonic perturbations ξ defined as

$$-i\omega\xi = \boldsymbol{v}_1 \,, \tag{2.17}$$

where ω is the (complex) frequency of the normal mode and $\boldsymbol{v}_1$ is the first-order perturbation of the equilibrium plasma velocity $\boldsymbol{v}_0$, which is zero for stationary equilibria. The imaginary factor comes from the derivative of the complex exponent of the normal mode $\sim e^{-i\omega t}$.

2 - Linearization

The linearization of the MHD equations then results from assuming the perturbed quantities to be much smaller than the equilibrium quantities (except for the velocity for stationary plasmas) and neglecting products of perturbed terms. Equations 2.10, 2.11 and 2.13 then reduce to [GP04]:

$$\rho_1 = -\nabla \cdot (\rho_0 \boldsymbol{\xi}) \ , \tag{2.18}$$

$$\mathbf{B}_1 = \nabla \times (\boldsymbol{\xi} \times \mathbf{B}_0) \ , \tag{2.19}$$

$$p_1 = -\boldsymbol{\xi} \cdot \nabla p_0 - \gamma p_0 \nabla \cdot \boldsymbol{\xi} \, , \tag{2.20}$$

$$\tag{2.21}$$

which can be filled in into the linearized version of equation 2.11, yielding a form of Newton's second law, namely equation 1.4 for normal modes:

$$-\rho_0 \omega^2 \boldsymbol{\xi} = \mathbf{F}\left(p_1(\boldsymbol{\xi}), \mathbf{B}_1(\boldsymbol{\xi}), \rho_1(\boldsymbol{\xi})\right) \ , \tag{2.22}$$

with the force operator defined as

$$\mathbf{F} \equiv -\nabla p_1 - \mathbf{B}_0 \times (\nabla \times \mathbf{B}_1) + (\nabla \times \mathbf{B}_0) \times \mathbf{B}_1 + \nabla \Phi_0 \nabla \cdot (\rho_0 \boldsymbol{\xi}) \ . \tag{2.23}$$

With some algebra, it can be shown that this force operator is Hermitian:

$$\int \boldsymbol{\eta}^* \cdot \mathbf{F}(\boldsymbol{\xi}) \, \mathrm{d}V = \int \boldsymbol{\xi} \cdot \mathbf{F}(\boldsymbol{\eta}^*) \, \mathrm{d}V \, , \tag{2.24}$$

where the integral runs over the volume of the system. This Hermiticity is an expression of the fact that there are no loss terms in ideal MHD.

3 - Rayleigh quotient

Using the property of Hermiticity, the *Rayleigh quotient* Λ can be defined as:

$$\Lambda \equiv \frac{\delta W}{\mathsf{K}} \, , \tag{2.25}$$

where δW is the perturbed potential energy of the system and K is related to the kinetic energy:

$$\delta W \equiv \frac{1}{2} \int \boldsymbol{\xi}^* \cdot \mathbf{F}(\boldsymbol{\xi}) \, \mathrm{d}V \, , \tag{2.26}$$

$$\mathsf{K} \equiv \frac{1}{2} \int \rho \boldsymbol{\xi}^* \boldsymbol{\xi} \, \mathrm{d}V \, . \tag{2.27}$$

It can be shown that the stationary values of the Rayleigh quotient are equal to the square of the complex normal mode frequency $\Lambda_{\mathrm{stat}} = \omega^2$. Note that they have to be real.

Complete expressions for the quantities introduced here are given in chapter 3, for the extended energy principle, where the system consists of a toroidal plasma of general shape, connected to a surrounding vacuum through the plasma edge, on which a skin current is allowed run. The advantage of using a variational principle such as the Rayleigh Quotient is then that the interface conditions at the plasma edge are automatically satisfied.

The extended energy principle is one of the foundations of this work. In the next chapter, a theoretical exposition follows.

Chapter 3

3-D Edge Theory

The content of this chapter was published in ***Physics of Plasmas*** *by T. Weyens, R. Sánchez, L. García and A. Loarte under the name* ***Three-dimensional linear peeling-ballooning theory in magnetic fusion devices*** *[Wey+14]. It is reproduced here, with the permission of AIP Publishing. The typography has been adapted to the style of this document.*

The creation of ideal linear high-n theory for 3-D edge toroidal magnetic configurations is the first major task of this work. The derivation is described in this chapter. Use is made of the extended energy principle, where the perturbation is described through Fourier modes in the angular variables. The flutedness of the modes then leads to the condition $nq - m \sim \mathcal{O}(1)$, while both $n \gg 1$ and $m \gg$, which is used to order the terms of the potential and kinetic energy.

An important consequence of the flutedness of the perturbation is that only modes that correspond to the same field line can be assumed to couple, so that the result for different field lines can be calculated independently. This reduces the complexity of the mathematical problem so that ultimately it is of the same order as for the axisymmetric case.

To find the normal mode eigenvalues and eigenvectors, use is then made of the Rayleigh-Quotient, which is defined as the ratio between the perturbed potential energy and the kinetic energy, and the stationary values of which correspond to the Eigenvalues. In a first step the perturbation is decomposed in the normal direction (to the flux surfaces), the parallel direction (to the magnetic field) and the geodesic direction, perpendicular to both, and the parallel and geodesic components of the different Fourier modes are minimized as a function of the normal components. Euler mini-

mization is then employed to calculate the minimized energy, with the end result being a coupled set of second-order ordinary differential equations in the normal components of the Fourier modes of the perturbation that contain an Eigenvalue. This has to be solved numerically.

Abstract

Ideal Magnetohydrodynamics (MHD) theory is extended to fully 3D magnetic configurations to investigate the linear stability of intermediate to high-n peeling-ballooning modes, with n the toroidal mode number. These are are thought to be important for the behavior of Edge Localized Modes (ELMs) and for the limit of the size of the pedestal that governs the high confinement H-mode. The end point of the derivation is a set of coupled second order ordinary differential equations with appropriate boundary conditions that minimize the perturbed energy and that can be solved to find the growth rate of the perturbations. This theory allows of the evaluation of 3D effects on edge plasma stability in tokamaks such as those associated with the toroidal ripple due to the finite number of toroidal field coils, the application of external 3D fields for ELM control, local modification of the magnetic field in the vicinity of ferromagnetic components such as the test blanket modules (TBMs) in ITER, etc.

3.1 Introduction

The magnetohydrodynamic (MHD) model is inherently limited in scope and applicability by the strong assumptions behind it. Yet, despite its relative simplicity, it has been shown to be surprisingly applicable, mainly due to the strong anisotropy between the parallel and perpendicular dynamics. Furthermore, MHD theory can generally be used as a baseline for the behavior of plasma dynamics [GP04]. Important here are the MHD instabilities that may ultimately limit the performance of fusion devices.

There is a variety of MHD instabilities that can occur in plasma and they can be categorized in various ways: One of them is the distinction between internal instabilities, that do not disturb the plasma boundary, and external ones, that do. Alternatively, they can be global, spanning an extended range within the plasma, or localized. Lastly, another way of classification instabilities is by considering the main mechanism that drives them. These turn out to be the parallel current and the pressure gradient, hence the denotation "current driven" or "pressure driven" [Fre87; Wes78].

Two important modes of instabilities that have been identified in current

devices are the *peeling mode*, which is a global, current driven mode that can be thought of as a limiting case of the external interchange mode [WM99], and the *ballooning mode*, which is a localized pressure driven mode. Note, however, that here and henceforth the words local and global indicate a localization around particular field lines versus delocalization in the entire flux surface, respectively, and are not directly connected to the radial extent. Coupled, the peeling-ballooning modes are thought to be important for the limiting behavior of some modern devices, as they are able to cause periodically erupting *edge localized modes* (ELMs). These limit the size of the pressure gradient in the *pedestal*, which is one of the main characteristics of the high confinement *H-mode* [Sny+02]. Therefore, it is of importance to correctly understand the physics behind the peeling-ballooning mode and to be able to simulate it accurately.

There exist fairly complete analytic theories for both the localized, pressure driven ballooning mode [CHT79; Con+98] and the global, current driven peeling mode [Lor75]. Since the main interest for ELMs lies in describing the instabilities of the outer layers of the plasma, these theories take into account the approximate effect of the perturbation of the plasma edge. However, bringing these two theories together required some effort, since the theory of peeling modes is formulated for global modes, whereas the theory of ballooning modes employs an asymptotic, so-called "high-n" (where n refers to the toroidal mode number) ordering that is valid only for localized modes, and breaks down for more extended modes. It is clear, then, that a purely analytically theory is difficult to conceive and one has to resort to simulations.

One strategy has been to drop the high-n ordering which, though useful for analytically understanding of the ballooning modes, cannot easily describe the peeling modes, and to simulate the plasma with the full MHD model without approximation in the toroidal mode number. Codes such as MISHKA [Mik+97] and KINX [Deg+97] are very successful at describing the phenomena of peeling-ballooning modes and accurate results have been obtained [Huy05]. However, since these codes are not very fast, they are not always suitable for parameter studies, so a main step in this domain has been the development of the linear numerical code ELITE, that indeed employs a high-n ordering at the plasma edge, but also keeps higher order terms to correctly describe the intermediate n peeling-ballooning modes [Wil+02].

ELITE has been successful at describing peeling-ballooning phenomena and has allowed the subsequent study of the linear properties of ELMs

[Sny+02; Sny+04; Web12]. However, the main limitation of ELITE and the theory behind it, is the fact that it is valid only for *axisymmetric* configurations. This allows for many simplifications, yet it can present an important limitation to the generality of the predicted results. For example, stellarators are inherently 3D and thus need 3D theory to be accurately described. But also tokamaks, that can be approximated quite well by the assumption of axisymmetry, experience some degree of three dimensionality. The ripple due to the discrete toroidal coils, for example, breaks axisymmetry. Also, in recent years, the effects of resonant 3D fields on the edge of tokamak plasmas have received increased attention because of their capability to control the energy losses and power fluxes to plasma facing components caused by ELMs, which can lead to unacceptable erosion rates of these components in tokamak fusion reactors such as ITER [Eva+06].

In this work a full 3D theory is developed in the same spirit as the axisymmetric theory behind ELITE, yet without employing the limiting axisymmetric assumption. It differs from pure analytic 3D ballooning mode theory and 3D peeling mode theory in two ways. Firstly, no assumptions are made on the form of the plasma perturbation, such as the *ballooning description* used to derive the general 3D ballooning mode equation [Cor82b]. Secondly, the treatment of the plasma edge is not done in an approximate fashion, as in [Con+98] for 2D ballooning modes, [Cor99] for 3D ballooning modes or [Lor75] for peeling modes: The inclusion of the effects due to the perturbation of the plasma surface is done as in ELITE, through the actual calculation of the perturbed energy of the plasma boundary and the surrounding vacuum, employing the extended energy principle [Ber+58].

The structure of this paper is as follows: In the next section, the major analytic derivation of the 3D peeling-ballooning theory is developed. This is done in steps, described in various subsections. The results, which consist of a coupled set of second-order linear differential equations whose solution provides the growth rate of the system, are then discussed in section 3.3 and interesting features are pointed out, as well as the parallels with the 2D work performed earlier. After that, in section 3.4, conclusions are stated and finally, appendices give more details about longer derivations.

3.2 Derivation

1 - Preliminaries

The starting point is the extended energy principle, which describes the system as if consisting of a body of plasma, separated from a conducting wall by a vacuum layer [Ber+58]. The energy of the whole system, comprised of

kinetic energy and potential energy of the plasma, a possible edge current at the plasma surface and the magnetic energy of the surrounding vacuum, is perturbed linearly and the eigenvalues corresponding to this perturbation can be found from the stationary values of the *Rayleigh quotient*:

$$\Lambda\left[\boldsymbol{\xi}, \mathbf{Q}_{\mathrm{v}}\right] \equiv \frac{\delta W\left[\boldsymbol{\xi}, \mathbf{Q}_{\mathrm{v}}\right]}{\mathrm{K}\left[\boldsymbol{\xi}\right]} \equiv \frac{\delta W_{\mathrm{p}}\left[\boldsymbol{\xi}\right] + \delta W_{\mathrm{s}}\left[\xi_{\mathrm{n}}\right] + \delta W_{\mathrm{v}}\left[\mathbf{Q}_{\mathrm{v}}\right]}{\frac{1}{2}\int_{\mathrm{p}} \rho\left|\boldsymbol{\xi}\right|^{2} \mathrm{d}\mathbf{r}} \,. \tag{3.1}$$

The different terms are given by [GP04]:

$$\begin{cases} \delta W_{\mathrm{F}}\left(\boldsymbol{\xi}\right) = \dfrac{1}{2}\displaystyle\int_{\mathrm{p}} \mathrm{d}\mathbf{r} \left[\frac{\left|\mathbf{Q}\right|^{2}}{\mu_{0}} - \boldsymbol{\xi}^{*}\cdot\mathbf{j}\times\mathbf{Q} + \gamma \mathrm{p}\left|\nabla\cdot\boldsymbol{\xi}\right|^{2} + \right. \\ \qquad\qquad \left. + \left(\boldsymbol{\xi}\cdot\nabla \mathrm{p}\right)\nabla\cdot\boldsymbol{\xi}^{*}\right] \\ \delta W_{\mathrm{s}}\left(\xi_{\mathrm{n}}\right) = \dfrac{1}{2}\displaystyle\int_{\mathrm{s}} \mathrm{dS}\left[\left|\mathbf{n}\cdot\boldsymbol{\xi}\right|^{2}\mathbf{n}\cdot\left[\!\left[\nabla\left(\mu_{0}\mathrm{p} + \frac{\mathrm{B}^{2}}{2}\right)\right]\!\right]\right]_{\mathrm{s}} \\ \delta W_{\mathrm{v}}\left(\mathbf{Q}_{\mathrm{v}}\right) = \dfrac{1}{2}\displaystyle\int_{\mathrm{v}} \mathrm{d}\mathbf{r}\left[\frac{\left|\mathbf{Q}_{\mathrm{v}}\right|^{2}}{\mu_{0}}\right] \,, \end{cases} \tag{3.2}$$

where $[\![\cdot]\!]$ denotes a jump and $\boldsymbol{\xi}$ and $\mathbf{Q}_{\mathrm{v}}$ are the plasma displacement and the vacuum magnetic field perturbation, which have to satisfy only the *essential boundary conditions*:

$$\begin{cases} \boldsymbol{\xi} \text{ regular} & \text{(on V)} \\ \mathbf{n}\cdot\nabla\times\left(\boldsymbol{\xi}\times\mathbf{B}_{\mathrm{v}}\right) = \mathbf{n}\cdot\mathbf{Q}_{\mathrm{v}} & \text{(on S)} \\ \mathbf{n}\cdot\mathbf{Q}_{\mathrm{v}} = 0 & \text{(on exterior wall } W_{\mathrm{v}}) \,. \end{cases} \tag{3.3}$$

$\delta\mathbf{B} = \mathbf{Q} = \nabla\times\left(\boldsymbol{\xi}\times\mathbf{B}\right)$ is the perturbation of the plasma magnetic field and all the other symbols have their usual meaning.

For the plasma potential energy, an equivalent form [GJ68] is used:

$$\begin{aligned} \delta W_{\mathrm{F}} = \frac{1}{2}\int \mathrm{d}\mathbf{r}\left[\frac{1}{\mu_{0}}\left|\overline{\mathbf{Q}}\right|^{2} + \gamma \mathrm{p}\left|\nabla\cdot\boldsymbol{\xi}\right|^{2}\right. \\ \left. -2\left(\boldsymbol{\xi}\cdot\nabla \mathrm{p}\right)\left(\boldsymbol{\kappa}\cdot\boldsymbol{\xi}^{*}\right) - \sigma\left(\boldsymbol{\xi}^{*}\times\mathbf{B}\right)\cdot\overline{\mathbf{Q}}\right] \,, \end{aligned} \tag{3.4}$$

where $\boldsymbol{\kappa} = \hat{\mathbf{b}}\cdot\nabla\hat{\mathbf{b}} = \frac{1}{\mathrm{B}^{2}}\nabla_{\perp}\left(\mu_{0}\mathrm{p} + \frac{\mathrm{B}^{2}}{2}\right)$ is the curvature, $\sigma \equiv \frac{\mathrm{J}_{\parallel}}{\mathrm{B}}$ is proportional to the parallel current and $\overline{\mathbf{Q}}$ is defined as follows:

$$\overline{\mathbf{Q}} = \mathbf{Q} - \mathbf{B}\frac{\mu_{0}\boldsymbol{\xi}\cdot\nabla \mathrm{p}}{\mathrm{B}^{2}} = \mathbf{Q}_{\perp} - \mathbf{B}\left[\nabla\cdot\boldsymbol{\xi}_{\perp} + 2\boldsymbol{\xi}_{\perp}\cdot\boldsymbol{\kappa}\right] \,. \tag{3.5}$$

In equation 3.4 the first term can be identified as the stabilizing term due to the perturbation of the magnetic field and the second one due to the perturbation of the plasma. The other two terms show the main driving terms for instabilities, due to the pressure gradient and the parallel current, as discussed in section 3.1.

2 - Plasma perturbation and other quantities

In what follows, the same flux coordinates (ψ, θ, ζ) as in [DG83] are used:

$$\mathbf{B} = \nabla\zeta \times \nabla\psi + q(\psi)\nabla\psi \times \nabla\theta \,, \tag{3.6}$$

which, by defining the field line label $\alpha = \zeta - q(\psi)\theta$, can be brought into Clebsch form in the new (α, ψ, θ) coordinate system:

$$\mathbf{B} = \nabla\alpha \times \nabla\psi \,, \tag{3.7}$$

where the Jacobian $\mathcal{J}(\alpha, \psi, \theta)$ is identical to the Jacobian in the flux coordinates $\mathcal{J}(\psi, \theta, \zeta)$. In this coordinate system, the parallel derivative reduces to $\mathbf{B} \cdot \nabla = \frac{1}{\mathcal{J}} \frac{\partial}{\partial\theta}$. Note that θ has lost its immediate poloidal significance and now rather means "along the magnetic field line".

In the spirit of [GJ68, eq. A.6], the *plasma perturbation* ξ is decomposed in a normal, a geodesic and a parallel component:

$$\xi = X\frac{\nabla\psi}{|\nabla\psi|^2} + U\frac{\nabla\psi \times \mathbf{B}}{B^2} + W\mathbf{B} \,. \tag{3.8}$$

Employing this, the three components of $\overline{\mathbf{Q}}$, defined in 3.5, are given by:

$$\begin{cases} \nabla\psi \cdot \overline{\mathbf{Q}} = \dfrac{1}{\mathcal{J}}\dfrac{\partial X}{\partial\theta} \\ \dfrac{\nabla\psi \times \mathbf{B}}{|\nabla\psi|^2} \cdot \overline{\mathbf{Q}} = \dfrac{1}{\mathcal{J}}\dfrac{\partial U}{\partial\theta} - SX \\ \mathbf{B} \cdot \overline{\mathbf{Q}} = -B^2\left[\nabla \cdot \xi_\perp + 2\xi \cdot \boldsymbol{\kappa}\right] \,. \end{cases} \tag{3.9}$$

with the total (or local) shear S [GJ68] in the (α, ψ, θ) coordinate system:

$$\begin{aligned} S &= -\frac{\nabla\psi \times \mathbf{B}}{|\nabla\psi|^2} \cdot \nabla \times \left(\frac{\nabla\psi \times \mathbf{B}}{|\nabla\psi|^2}\right) \\ &= -\frac{1}{\mathcal{J}}\frac{\partial\Theta^\alpha}{\partial\theta} \,, \end{aligned} \tag{3.10}$$

where $B_i = \mathbf{B} \cdot \boldsymbol{e}_i$ and $\Theta^i = \frac{\nabla\psi}{|\nabla\psi|^2} \cdot \nabla u^i$, with u^i one of the coordinates (ψ, θ, ζ).

The curvature lacks a parallel component and, aiming for later compactness of results, the normal and geodesic components are defined as follows:

$$\begin{cases} \kappa_n = \dfrac{\nabla\psi}{|\nabla\psi|^2}\cdot\boldsymbol{\kappa} = \dfrac{\nabla\psi}{|\nabla\psi|^2\,B^2}\cdot\nabla\left(\mu_0 p + \dfrac{B^2}{2}\right) \\ \kappa_g = \dfrac{\nabla\psi\times\mathbf{B}}{B^2}\cdot\boldsymbol{\kappa} = -\dfrac{1}{2p'}\dfrac{1}{\mathcal{J}}\dfrac{\partial\sigma}{\partial\theta}\,, \end{cases} \tag{3.11}$$

with $\sigma = \frac{\mathbf{B}}{B^2}\cdot\frac{\nabla\times\mathbf{B}}{\mu_0}$ proportional to the parallel current. Use is made of the fact that the current is divergence-free, implying:

$$\nabla\cdot(\mathbf{B}\sigma) - \frac{2}{B^4}\nabla\left(\frac{B^2}{2}\right)\cdot\mathbf{B}\times\nabla p = 0\,. \tag{3.12}$$

3 - Fourier representation of the perturbation

As mentioned in section 3.1, the modes considered in this work are intermediate to high-n in nature. More specifically, this means that these modes are assumed to have a spectral content that is much higher than the spectral content of the equilibrium quantities. This condition is used further on to make key simplifications.

In this work, a Fourier representation is used, of which the advantages are, on the one hand, that the periodicity constraints that the modes have to comply with are inherently satisfied, and, on the other hand, that the separation of spectra of the equilibrium and the perturbation can be performed mathematically. Furthermore, a Fourier representation does not fail near the plasma edge, as is the case for the higher orders of theory using the ballooning representation, frequently used in theoretical studies [HM03; CHT79].

To avoid large stabilization of the plasma potential energy due to excitation of Alfvèn and fast magnetosonic waves (the term containing $\overline{\mathbf{Q}}$ in equation 3.4), the allowable perturbations have to approximately follow the magnetic field and thus have a *fluted shape*, similarly to the case of normal ballooning modes. Mathematically, this translates in the condition that the parallel derivative be of order 1 and thus:

$$\frac{\partial}{\partial\theta} \sim \mathcal{O}(1)\,. \tag{3.13}$$

This reduces the order of the normal and geodesic components of $\overline{\mathbf{Q}}$ to $\mathcal{O}(1)$ and the only remaining term of order $\mathcal{O}\left(\epsilon^{-1}\right)$ is $\nabla\cdot\boldsymbol{\xi}_\perp$, with ϵ a small parameter that will be defined later. Clearly, not both the derivatives in α and ψ can be chosen of order $\mathcal{O}(1)$, as this would prevent the perturbations

from being localized at all. However, their combination in the divergence can indeed be of order $\mathcal{O}(1)$.

Subsequently, the stabilizing term due to sound waves that compress the plasma (the term containing $\nabla \cdot \boldsymbol{\xi}$ in equation 3.4) is assumed to be minimized to zero by correctly adjusting the parallel component of the perturbation to cancel out the contribution $\nabla \cdot \boldsymbol{\xi}_\perp$ due to the perpendicular components (all of order $\mathcal{O}(1)$), though strictly speaking there exist theoretical cases where this is not possible, such as the Z-pinch [Fre82]. Thus, the plasma is assumed to be incompressible, suppressing the stabilizing sound waves.

To derive the corresponding criteria relating the two components X and U of $\boldsymbol{\xi}_\perp$, in the (ψ, θ, ζ) coordinate system, the Fourier representation in the variables $\epsilon^{-1}\alpha$ and $\epsilon^{-1}\theta$ is presented, with n the toroidal and m the poloidal mode number:

$$\begin{cases} X\left(\psi, \epsilon^{-1}\theta, \epsilon^{-1}\zeta\right) = \sum_{m,n} \hat{X}_{m,n}(\psi)\, e^{i[n\zeta - m\theta]} \\ U\left(\psi, \epsilon^{-1}\theta, \epsilon^{-1}\zeta | \theta, \zeta\right) = \sum_{m,n} \hat{U}_{m,n}(\psi|\theta, \zeta)\, e^{i[n\zeta - m\theta]} \end{cases}, \tag{3.14}$$

where the notation $\left(\psi, \epsilon^{-1}\theta, \epsilon^{-1}\zeta | \theta, \zeta\right)$ means that an additional periodic slow variation of the Fourier amplitude $U_{m,n}$ is allowed, as is customary in *multiple-scale analysis* [BO99]. It will be seen that this is necessary to cancel secular terms that will appear to ultimately yield a solution that is indeed periodic.

Transforming to the (α, ψ, θ) coordinate system, yields

$$e^{i[n\zeta - m\theta]} \to e^{i[n\alpha + (nq - m)\theta]}, \tag{3.15}$$

which means that the condition that the parallel derivatives be of order $\mathcal{O}(1)$ reduces to

$$nq - m \sim \mathcal{O}(1), \tag{3.16}$$

with q the safety factor.

This has the consequence that the perturbations, though with both $m \sim \mathcal{O}\left(\epsilon^{-1}\right)$ and $n \sim \mathcal{O}\left(\epsilon^{-1}\right)$, lie clustered around the line with slope q, as seen in figure 3.1, which represents the separation between the spectral content of the equilibrium quantities and the perturbation. This anisotropy has an important implication: The modes do not couple for different magnetic field lines (represented by the coordinate α), but only along magnetic field lines (represented by θ), so the double summation reduces to a single summation over m.

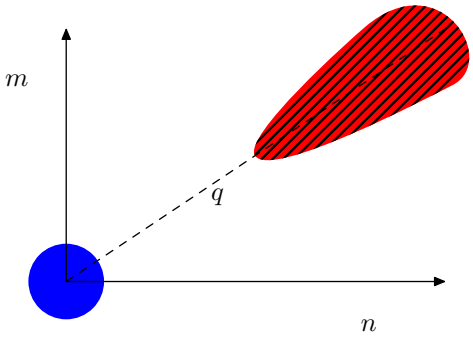

Figure 3.1
A sketch of the assumed spectra of the equilibrium quantities (blue) and the perturbation (red, hatched). The horizontal axis indicates the toroidal wave number $\mathfrak{n}$ and the vertical axis the poloidal wave number $\mathfrak{m}$.

This result can be indicated symbolically by considering the following representation for the plasma potential energy that explicitly shows the coupling between a mode with mode numbers $\mathfrak{n}$ and $\mathfrak{m}$ and a mode with $\mathfrak{n}'$ and $\mathfrak{m}'$, and where $A = A(\alpha, \psi, \theta)$ represents equilibrium quantities:

$$\begin{aligned}
&\sum_{\mathfrak{m},\mathfrak{n}} \left[\int d\theta \int d\alpha A e^{i[\mathfrak{n}-\mathfrak{n}']\alpha} e^{i[(\mathfrak{n}q-\mathfrak{m})-(\mathfrak{n}'q-\mathfrak{m}')]\theta} \right] X_{\mathfrak{m},\mathfrak{n}} X^*_{\mathfrak{m}',\mathfrak{n}'} \\
&= \sum_{\mathfrak{m},\mathfrak{n}} \left[\int d\theta \left[\int d\alpha A e^{i[\mathfrak{n}-\mathfrak{n}']\alpha} \right] e^{i[(\mathfrak{n}q-\mathfrak{m})-(\mathfrak{n}'q-\mathfrak{m}')]\theta} \right] X_{\mathfrak{m},\mathfrak{n}} X^*_{\mathfrak{m}',\mathfrak{n}'} \\
&\approx \frac{1}{2\pi} \sum_{\mathfrak{m},\mathfrak{n}} \left[\int d\theta A \delta^{\mathfrak{n}'}_{\mathfrak{n}} e^{i[(\mathfrak{n}q-\mathfrak{m})-(\mathfrak{n}'q-\mathfrak{m}')]\theta} \right] X_{\mathfrak{m},\mathfrak{n}} X^*_{\mathfrak{m}',\mathfrak{n}'} \\
&\approx \frac{1}{2\pi} \sum_{\mathfrak{m}} \left[\int d\theta A e^{i(\mathfrak{m}'-\mathfrak{m})\theta} \right] X_{\mathfrak{m}} X^*_{\mathfrak{m}'} \Big|_{\mathfrak{n}=\mathfrak{n}'},
\end{aligned} \tag{3.17}$$

implying that, though the equilibrium quantities vary across the magnetic field lines, in the coordinate α, they are quasi-constant in the $\mathfrak{n}\alpha$ scales on which the perturbations vary, effectively removing A from the integral in α. The same cannot be done for the integral along the magnetic field lines in θ, since the perturbations vary as slowly as the equilibrium quantities due to their flutedness.

Note that the integral along θ is a field-line average: *Toroidal information about the equilibrium is preserved*, since the magnetic field line varies toroidally. This in contrast to the axisymmetric case where the line average can be reduced to an average in the poloidal angle, as in [Wil+02].

Therefore, ultimately, the Fourier representations for X and U used are:

$$\begin{cases} X = \sum_m \hat{X}_m(\psi)\, e^{i[n\alpha+(nq-m)\theta]} \\ U = \sum_m \hat{U}_m(\psi|\alpha,\theta)\, e^{i[n\alpha+(nq-m)\theta]} \end{cases}, \tag{3.18}$$

with the exponents containing both terms of order $\mathcal{O}(1)$ and of order $\mathcal{O}(n)$ with ϵ from now on chosen to be equal to n^{-1}.

4 - Minimizing plasma perturbation

In a first step, the fast variation across the magnetic field lines, in the coordinate $n\alpha$ is introduced by inserting only the fast part of the full Fourier representations of equation 3.18

$$\begin{cases} X = \hat{X}(\psi,\theta)\, e^{in\alpha} \\ U = \hat{U}(\psi,\theta|\alpha,\theta)\, e^{in\alpha} \end{cases}, \tag{3.19}$$

into the condition $\nabla\cdot\xi_\perp \sim \mathcal{O}(1)$. To this end, an ordering technique for the normal perturbation X is applied as follows:

$$X = X^{(0)} + X^{(1)} + \dots, \tag{3.20}$$

with $\left|X^{(k)}\right| / \left|X^{(k+1)}\right| \sim \mathcal{O}(n)$. Doing the same for the other components, a condition for the first orders $X^{(0)}$ and $U^{(0)}$ is derived:

$$\hat{U}^{(0)} = \left(-\Theta^\alpha + \frac{i}{n}\left(\frac{\partial}{\partial\psi} + \Theta^\theta\frac{\partial}{\partial\theta}\right)\right)\hat{X}^{(0)}. \tag{3.21}$$

[Note that the θ component has been included for the term in X, even though it is formally of lower order than the other two. This is done in hindsight by realizing that it is the most convenient way for the geodesic perturbation to be periodic (see further below), simplifying the two-scale analysis. The same result could be obtained by considering the problem in the unmodified flux coordinates (ψ,θ,ζ), but would require a little bit more work.]

Subsequently, the second order can be minimized as well making use of the first order result. Collecting terms in the divergence and combining them with the curvature term yields an expression correct up to order $\sim\mathcal{O}\left(n^{-1}\right)$

$$0 = \left(in\Theta^\alpha + \frac{\partial}{\partial\psi} + \Theta^\theta\frac{\partial}{\partial\theta}\right)\hat{X} + in\hat{U} + \hat{Q}\left(\hat{X}\right), \tag{3.22}$$

where the second-order operator $\hat{Q}$ is defined as:

$$\begin{aligned}\hat{Q}(\beta) = &\left[\frac{1}{\mathcal{J}}\frac{\partial}{\partial u^i}\left(\mathcal{J}\Theta^i\right) + 2\kappa_n\right]\beta \\ &+ \left[2\kappa_g + \frac{1}{\mathcal{J}}\frac{\partial \mathcal{J}}{\partial \alpha} - \frac{1}{\mathcal{J}}\frac{\partial}{\partial \theta}\left(\frac{B_\alpha}{B^2}\right) - \frac{1}{\mathcal{J}}\frac{B_\alpha}{B^2}\frac{\partial}{\partial \theta} + \frac{\partial}{\partial \alpha}\right] \times \\ &\times \left[\left(-\Theta^\alpha + \frac{i}{n}\left(\frac{\partial}{\partial \psi} + \Theta^\theta \frac{\partial}{\partial \theta}\right)\right)\beta\right] .\end{aligned} \tag{3.23}$$

This eliminates the parallel component of the magnetic terms and reduces the entire stabilizing magnetic term to order $\sim \mathcal{O}(1)$.

In a second step, the previous expression for Q is now simplified by inserting the remainder of the Fourier representation for the coordinate $(nq - m)\theta$, the slow coordinate along the magnetic field:

$$\begin{cases} \hat{X} = \sum_m \hat{X}_m(\psi)\, e^{i(nq-m)\theta} \\ \hat{U} = \sum_m \hat{U}_m(\psi|\alpha,\theta)\, e^{i(nq-m)\theta} , \end{cases} \tag{3.24}$$

For ease of notation, in what follows, the hat is left out and it is to be understood implicitly that Fourier modes are treated. In any case, the presence of a subscript m denotes a (complete) Fourier mode.

Using above, the condition 3.22 becomes:

$$U_m = \left(-\Theta^\zeta + \frac{m}{n}\Theta^\theta + \frac{i}{n}\frac{\partial}{\partial \psi}\right) X_m + \frac{i}{n} Q_m(X_m) , \tag{3.25}$$

relating U_m to X_m, with $\Theta^\zeta \equiv \Theta^\alpha + q'\theta + \Theta^\theta q$ and

$$Q_m(X_m) = \left(Q_m^0 + Q_m^1 \frac{i}{n}\frac{d}{d\psi}\right)(X_m) , \tag{3.26}$$

where Q_m^0 and Q_m^1 only depend on equilibrium quantities. They are calculated in the appendix:

$$\begin{cases} Q_m^0 = \dfrac{B_\alpha q' + \mathcal{J}\mu_0 p'}{B_\theta} + \left(-\Theta^\zeta + \Theta^\theta \dfrac{m}{n}\right) Q_m^1 \\ \qquad\qquad + \dfrac{nq - m}{n}\dfrac{\mathcal{J}\mathbf{B}\cdot\nabla\psi\times\nabla\Theta^\theta}{B_\theta} \\ Q_m^1 = -i(nq - m)\dfrac{B_\alpha}{B_\theta} . \end{cases} \tag{3.27}$$

Note that the term proportional to Q_m in equation 3.25 is an order of magnitude smaller than the other terms and that U_m indeed has a slow-varying component in the coordinates α and θ. Also note that the relative strength of the dependence on ψ is not important. Inserting the expression thus obtained for the modes U_m into equation 3.4 then yields an expression for the plasma potential energy, as a function of the normal displacement X_m only, correct up to second order in n.

Summarizing, by first requiring the entire stabilizing magnetic energy to be finite and of order $\mathcal{O}(1)$, leading to fluted modes, and subsequently minimizing the magnetic compressional energy to zero, above expression for the geodesic component of the Fourier modes U_m was derived, expressed as a function of X_m (eq. 3.25). This allowed for the complete description of the plasma potential energy as a function of the normal component X_m.

Finally, mixing the different orders of the terms, this expression can be split into a linear part and a part corresponding to the first derivative:

$$U_m = \left(U_m^0 + U_m^1 \frac{i}{n} \frac{\partial}{\partial \psi} \right) (X_m) \ , \tag{3.28}$$

with:

$$\begin{cases} U_m^0 = -\Theta^\zeta + \Theta^\theta \dfrac{m}{n} + \dfrac{i}{n} Q_m^0 \\ U_m^1 = 1 + \dfrac{i}{n} Q_m^1 \ , \end{cases} \tag{3.29}$$

where Q_m^0 and Q_m^1 are defined in equation 3.27. U_m can thus be seen as a linear differential operator, acting on the modes of the normal perturbation. In what follows, it is found useful to assign a symbol to the parallel derivative of U in θ, which can be written out compactly:

$$\frac{\partial U_m}{\partial \theta} = \left(DU_m^0 + DU_m^1 \frac{i}{n} \frac{\partial}{\partial \psi} \right) (X_m) \ , \tag{3.30}$$

with

$$\begin{cases} DU_m^0 = i(nq - m) U_m^0 + \dfrac{\partial U_m^0}{\partial \theta} \\ DU_m^1 = i(nq - m) U_m^1 + \dfrac{\partial U_m^1}{\partial \theta} \ . \end{cases} \tag{3.31}$$

5 - Minimization of plasma potential energy

To obtain the expression for the plasma potential energy it is useful to define the adjoint of the linear operator U_k^*:

$$\langle U_k(\alpha), \beta \rangle_\psi = \langle \alpha, U_k^T(\beta) \rangle - \left[\mathcal{J} \frac{i}{n} U_k^{1*} \alpha^* \beta \right]_{\psi_a}^{\psi_s} , \tag{3.32}$$

where the boundary term, with ψ_a a flux surface deep inside the plasma and ψ_s at the plasma edge, arises from the fact that external modes are considered, which do not necessarily vanish at the limits of integration. The inner product is defined as:

$$\langle \alpha, \beta \rangle_\psi = \int_{\psi_a}^{\psi_s} \mathcal{J} \alpha^* \beta \, d\psi , \tag{3.33}$$

and the operator U_k^T as:

$$U_k^T(\beta) = \left(U_k^{T,0} + U_k^{T,1} \frac{i}{n} \frac{\partial}{\partial \psi} \right) \beta , \tag{3.34}$$

with

$$\begin{cases} U_k^{T,0} = U_k^{0*} + \dfrac{1}{\mathcal{J}} \dfrac{i}{n} \dfrac{\partial}{\partial \psi} \left(U_k^{1*} \mathcal{J} \right) \\ U_k^{T,1} = U_k^{1*} , \end{cases} \tag{3.35}$$

and equivalently for DU from equation 3.30.

Now, the series of equation 3.18 is introduced into the plasma potential energy, given by equation 3.4, making use of the above expression of the adjoint operators U_k^T and DU_k^T. In the appendix it is shown that this reduces to a volume integral with three types of terms concerning the coupling of the modes m and k ($\equiv m'$): Those proportional to the amplitude of the mode X_m, those proportional to the first derivative in ψ of X_m and those proportional to the second, and all terms also proportional to the amplitude X_k^* of mode k. This is accompanied by a surface integral, with two types of terms. The expression for the plasma potential energy then has the form:

$$\frac{1}{2} \sum_{k,m} \int_{\psi_a}^{\psi_s} d\psi \left[\int d\theta \mathcal{J} X_k^* e^{i(k-m)\theta} PV_{k,m} \right] X_m , \tag{3.36}$$

with $PV_{k,m}$ a 2^{nd} order differential operator

$$PV_{k,m} = PV_{k,m}^0 + PV_{k,m}^1 \left(\frac{i}{n} \right) \frac{d}{d\psi} + PV_{k,m}^2 \left(\frac{i}{n} \right)^2 \frac{d^2}{d\psi^2} , \tag{3.37}$$

along with a surface term:

$$\frac{1}{2}\sum_{k,m}\int d\theta \mathcal{J} X_k^* e^{i(k-m)\theta} PSk, mX_m\Big|_{\psi_s}, \tag{3.38}$$

with

$$PS_{k,m} = PS^0_{k,m} + PS^1_{k,m}\left(\frac{i}{n}\right)\frac{d}{d\psi}. \tag{3.39}$$

The coefficients $PV^i_{k,m}$ and $PS^i_{k,m}$ are given by:

$$\begin{cases} PV^0_{k,m} = \widetilde{PV}^0_{k,m} + \dfrac{1}{\mathcal{J}}\dfrac{i}{n}\dfrac{\partial}{\partial\psi}\left(\mathcal{J}\widetilde{PV}^{1*}_{m,k}\right), \\ PV^1_{k,m} = \left(\widetilde{PV}^1_{k,m} + \widetilde{PV}^{1*}_{m,k}\right) + \dfrac{1}{\mathcal{J}}\dfrac{i}{n}\dfrac{\partial}{\partial\psi}\left(\mathcal{J}\widetilde{PV}^2_{k,m}\right), \\ PV^2_{k,m} = \widetilde{PV}^2_{k,m}, \\ PS^0_{k,m} = -\dfrac{i}{n}\widetilde{PV}^{1*}_{m,k}, \\ PS^1_{k,m} = -\dfrac{i}{n}\widetilde{PV}^2_{k,m}, \end{cases} \tag{3.40}$$

with

$$\begin{cases} \widetilde{PV}^0_{k,m} = \dfrac{1}{\mu_0}\dfrac{|\nabla\psi|^2}{\mathcal{J}^2 B^2}\left(DU^{0*}_k - \mathcal{J}S\right)\left(DU^0_m - \mathcal{J}S\right) + \dfrac{1}{\mathcal{J}}\dfrac{\partial\sigma}{\partial\theta}\left(U^{0*}_k + U^0_m\right) \\ \qquad\qquad + \dfrac{\sigma}{\mathcal{J}}\left(i\left(nq-m\right)U^{0*}_k - i\left(nq-k\right)U^0_m\right) + S\sigma - 2p'\kappa_n \\ \qquad\qquad + \dfrac{1}{\mu_0}\dfrac{\left(nq-k\right)\left(nq-m\right)}{\mathcal{J}^2|\nabla\psi|^2} \\ \widetilde{PV}^1_{k,m} = \dfrac{1}{\mu_0}\dfrac{|\nabla\psi|^2}{\mathcal{J}^2 B^2}\left(DU^{0*}_k - \mathcal{J}S\right)DU^1_m + \dfrac{U^1_m}{\mathcal{J}}\dfrac{\partial\sigma}{\partial\theta} - \sigma\dfrac{U^1_m}{\mathcal{J}}i\left(nq-k\right) \\ \widetilde{PV}^2_{k,m} = \dfrac{1}{\mu_0}\dfrac{|\nabla\psi|^2}{\mathcal{J}^2 B^2}DU^1_m DU^{1*}_k. \end{cases} \tag{3.41}$$

The two derivative terms in $PV^i_{k,m}$ are crucial for hermiticity of the plasma potential energy. This can best be seen by inserting equations 3.41 and 3.40 into equation 3.36 and canceling the surface terms from equation 3.38. The integrand of equation 3.36, including the double summation, then can be written in tensorial notation:

$$\left(\mathbf{X}^*\right)^T \mathbf{P}\,\mathbf{X} \tag{3.42}$$

where a factor $\mathcal{J}/2$ has been left out, with $\mathbf{X} = \left(X_m e^{-im\theta}\right)^T$ and the elements of the tensor $\mathbf{P}$ given by:

$$\begin{aligned} P_{k,m} =& \widetilde{PV}^0_{k,m} - \frac{i}{n}\frac{\overleftarrow{\partial}}{\partial\psi}\widetilde{PV}^{1*}_{m,k} + \widetilde{PV}^1_{k,m}\frac{i}{n}\frac{\overrightarrow{\partial}}{\partial\psi} \\ & - \frac{i}{n}\frac{\overleftarrow{\partial}}{\partial\psi}\widetilde{PV}^2_{k,m}\frac{i}{n}\frac{\overrightarrow{\partial}}{\partial\psi} , \end{aligned} \tag{3.43}$$

which are indeed hermitian. The arrows indicate whether the derivatives act on the right or on the left.

6 - Edge and vacuum energy

The edge term, given in equation 3.2, is associated with a sheet current $\mathbf{J}_s$ running on the edge of the plasma that provokes a discontinuity in the magnetic field on either side of the last flux surface of the plasma and is given by applying Ampère's law:

$$\mathbf{J}_s = \hat{\mathbf{n}} \times [\![\mathbf{B}]\!] \ . \tag{3.44}$$

Though a theoretical possibility, in practice an equilibrium edge current is unusual and therefore left out [Jar10]. In addition, by considering the essential boundary conditions of equation 3.3, it can be seen that the inclusion of an equilibrium edge current would lead to a highly stabilizing vacuum:

$$\mathbf{Q}_v \cdot \nabla\psi = \mathbf{B}_v \cdot \nabla X \quad \text{at s} \ . \tag{3.45}$$

Indeed, the derivative of X in the direction of $\mathbf{B}_v$ is of order $\mathcal{O}(n)$ if $\mathbf{B} \neq \mathbf{B}_v$, which would imply that the vacuum perturbation $\mathbf{Q}_v$ be of that order as well, leading to a large vacuum stabilization. This is to be avoided.

The vacuum energy, also given in equation 3.2, is always stabilizing and should be minimized while respecting the essential boundary conditions of equation 3.3. Since the vacuum is current-free, the vacuum magnetic perturbation $\mathbf{Q}_v$ satisfies

$$\nabla \cdot \mathbf{Q}_v = \nabla \times \mathbf{Q}_v = 0 \ , \tag{3.46}$$

which implies that it can be represented by a scalar potential ϕ that has to obey Laplace's equation:

$$\nabla^2\phi = 0 \ , \tag{3.47}$$

connected to the plasma by the essential boundary condition and assumed to vanish at infinity:

$$\nabla\psi \cdot \nabla\phi = \begin{cases} \mathbf{B} \cdot \nabla X & \text{at s} \\ 0 & \text{at w} \end{cases} , \tag{3.48}$$

Then, the vacuum energy term can be rewritten as:

$$\begin{aligned}\delta W_v &= \frac{1}{2\mu_0}\int_v d\mathbf{r}\,[\nabla\cdot(\phi\nabla\phi^*)]\\ &= \frac{1}{2\mu_0}\int_{\partial v} d\mathbf{S}\cdot(\nabla\phi^*)\,\phi\\ &= -\frac{1}{2\mu_0}\int_s \mathcal{J}\,(\mathbf{B}\cdot\nabla X^*)\,\phi\,d\theta\,d\alpha\,,\end{aligned} \tag{3.49}$$

where the negative sign is due to the difference between the definition of the outward normal of the plasma volume and the direction of increasing magnetic flux. The perturbation is assumed to vanish at the surrounding wall, located far away from the plasma, which is justified since peeling-ballooning perturbations are assumed to be radially localized to some extent. ϕ is to be solved with Laplace's equation as a function of the plasma perturbation X at the edge.

This is done conveniently using Green's method, based on Green's second identity [Jar10; Cha97]:

$$\nabla\cdot(a\nabla b) = a\nabla^2 b + \nabla a\cdot\nabla b\,, \tag{3.50}$$

which, upon interchanging a and b, taking the difference between both equations and integrating over a volume yields:

$$\int_v \left(a\nabla^2 b - b\nabla^2 a\right) dV = \int_{\partial v} (a\nabla b - b\nabla a)\cdot d\mathbf{S}\,. \tag{3.51}$$

This equation is used by setting $a = \phi\,(\mathbf{r})$ and $b = G_N\,(\mathbf{r},\mathbf{r}') = \frac{1}{|\mathbf{r}-\mathbf{r}'|} + F\,(\mathbf{r},\mathbf{r}')$, a modified Green's function for Neumann boundary conditions [Jac98] for the laplacian in three dimensions, with $\nabla^2 G = -\delta\,(\mathbf{r}-\mathbf{r}')$ and F a function that is symmetric in its arguments and satisfies:

$$\begin{cases}\nabla^2 F\left(\mathbf{r},\mathbf{r}'\right) = 0\\ \nabla\psi\cdot\nabla G_N = -\dfrac{4\pi}{\partial v}\,,\end{cases} \tag{3.52}$$

with ∂v the total surface surrounding the volume. Choosing this equal to the vacuum volume and evaluating at a point in the plasma edge, this yields an expression for the vacuum potential [AW05]:

$$\phi\,(\mathbf{r}) = \langle\phi\rangle + \iint_{\partial v} G_N\left(\mathbf{r},\mathbf{r}'\right)\nabla'\phi\left(\mathbf{r}'\right)\cdot d\mathbf{S}'\,, \tag{3.53}$$

where $\langle\phi\rangle$ is the average value of the potential over the whole surface.

Since the perturbation is assumed to vanish at the surrounding wall, the more complicated treatment of low n codes such as VACUUM [Cha97], that take into account the image currents in the surrounding wall, is not needed here. So upon introducing the boundary conditions from equation 3.48 and realizing that the average potential goes to zero due to the surrounding wall, assumed to be at infinity, equation 3.53 becomes:

$$\phi(\mathbf{r}) = -\iint_s G_N(\mathbf{r},\mathbf{r}')\, \jmath\mathbf{B}(\mathbf{r}') \cdot \nabla' X(\psi)\, d\alpha'\, d\theta' \,. \tag{3.54}$$

Inserting this relation between the potential and the plasma perturbation $X_{m,s}(\psi)$ at the edge of the plasma into equation 3.49 yields:

$$\delta W_v = \frac{1}{2} \sum_{k,m} X_k^* \left[\iint_s \jmath\, d\theta\, d\alpha \iint_s \jmath\, d\theta'\, d\alpha' V S_{k,m} \right] X_m \,, \tag{3.55}$$

with the Hermitian coefficients $VS_{k,m}$ given by:

$$\begin{aligned} VS_{k,m} = & \frac{1}{\mu_0} \frac{G_N(\mathbf{r},\mathbf{r}')}{\jmath^2} e^{i[n(\alpha'-\alpha)+(nq-m)\theta'-(nq-k)\theta]} \times \\ & \times (nq-m)(nq-k) \,. \end{aligned} \tag{3.56}$$

7 - Kinetic energy

Finally, the last ingredient in the extended spectral variational principle described in subsection 1 is the plasma kinetic energy, given by:

$$K[\xi] = \frac{\omega^2}{2} \int_p \rho |\xi|^2 \, d\mathbf{r} \,, \tag{3.57}$$

where ρ is the density of the plasma.

Now, as stated above, in subsection 4, the minimization of the plasma compressional energy to zero by adjusting the parallel component is relatively simple, and unaffected by the kinetic energy if the kinetic energy of the parallel component is neglected. Not doing this would raise the complexity of the problem, as the number of equations that has to be solved would double. As the applicability and accuracy of the parallel dynamics of the basic ideal MHD theory are questionable, this is not a major simplification and, in any case, it represents a worst-case scenario since the plasma sound waves are stabilizing [Fre82].

Since in the (perpendicular) plasma kinetic energy no derivatives of the perturbation appear, these terms do not influence the minimization of the magnetic compression term of the plasma potential energy performed in

subsection 4 and the results obtained there relating the geodesic perturbation U to the normal perturbation X are introduced in above formula for the plasma kinetic energy:

$$\begin{aligned} K_\perp &= \frac{\omega^2}{2}\int_p dr\rho \left[\frac{1}{|\nabla\psi|^2}|X|^2 + \frac{|\nabla\psi|^2}{B^2}|U|^2\right] \\ &= \frac{\omega^2}{2}\int_p dr\rho \sum_{k,m} e^{i(k-m)\theta}\left[\frac{1}{|\nabla\psi|^2}X_k^* X_m + \frac{|\nabla\psi|^2}{B^2}U_k^*(X_k^*)\,U_m(X_m)\right] \\ &= \frac{\omega^2}{2}\int_p dr \sum_{k,m} X_k^* e^{i(k-m)\theta}\left[\frac{\rho}{|\nabla\psi|^2} + U_k^T\frac{\rho|\nabla\psi|^2}{B^2}U_m\right](X_m)\ , \end{aligned} \tag{3.58}$$

where the operators work on everything to their right, resulting in volume and surface coefficients equivalent to the ones used equations 3.36 and 3.38:

$$\begin{cases} \widetilde{KV}^0_{k,m} = \dfrac{\rho}{|\nabla\psi|^2} + \dfrac{|\nabla\psi|^2}{B^2}U_k^{0*}U_m^0\rho \\ \widetilde{KV}^1_{k,m} = \dfrac{|\nabla\psi|^2}{B^2}U_k^{0*}U_m^1\rho \\ \widetilde{KV}^2_{k,m} = \dfrac{|\nabla\psi|^2}{B^2}U_k^{1*}U_m^1\rho\ . \end{cases} \tag{3.59}$$

Using the same arguments as in subsection 5, the integrand of the plasma kinetic energy integral can be written in a Hermitian form equivalent to equation 3.42.

3.3 Discussion

In the previous section, expressions were found for the potential energy due to the plasma, which was described by three volume coefficients $PV^i_{k,m}$ and two surface coefficients $PS^i_{k,m}$, the plasma kinetic energy, described by $KV^0_{k,m}$ and $KS^0_{k,m}$, and the potential energy due to the edge and vacuum, of which the former is neglected and the latter is described by $VS_{k,m}$.

By taking the Euler minimization with respect to each of the M amplitudes of the Fourier modes X^*_k, an equation in the M unknowns X_m is obtained. The result can be summarized by the following equation that has

to be solved for every field line:

$$\sum_m \left\{ \left\langle e^{i(k-m)\theta} V^0_{k,m} \right\rangle_\theta + \left\langle e^{i(k-m)\theta} V^1_{k,m} \right\rangle_\theta \left(\frac{i}{n}\right) \frac{d}{d\psi} + \left\langle e^{i(k-m)\theta} V^2_{k,m} \right\rangle_\theta \left(\frac{i}{n}\right)^2 \frac{d^2}{d\psi^2} \right\} X_m = 0, \tag{3.60}$$

for $k = m_0 \ldots m_0 + M$ and with the *field-line average* $\langle\cdot\rangle_\theta$ defined as:

$$\langle A \rangle_\theta = \int_{-\infty}^{\infty} \mathcal{J} A \, d\theta \,, \tag{3.61}$$

with the coefficients $V^i_{k,m}$ given by:

$$V^i_{k,m} = PV^i_{k,m} - \omega^2 KV^i_{k,m} \,, \tag{3.62}$$

from equations 3.40 and an equivalent for $KV^i_{k,m}$.

The restriction due to the normalization of the plasma kinetic energy using a Lagrange multiplier ω^2 is mathematically equivalent to the minimization of the Rayleigh quotient of equation 3.1 with an eigenvalue ω^2 and the appropriate boundary conditions shown below [AW05].

This is a system of M ordinary differential equations of second degree for the M different amplitudes X_m. Two boundary conditions are needed, the first one being the assumption that the perturbation vanishes deep into the plasma. The second boundary condition comes by minimizing the surface contributions from the plasma potential and kinetic energy and from the vacuum term, which leads to N equations:

$$\sum_m \left\{ \left\langle e^{i(k-m)\theta} S^0_{k,m} \right\rangle + \left\langle e^{i(k-m)\theta} S^1_{k,m} \right\rangle \frac{i}{n} \frac{\partial}{\partial \psi} + + \delta^{vac}_{k,m} \right\} X_m = 0 \,, \tag{3.63}$$

where the *surface coefficient* $PS_{k,m}$ are given by equations 3.40 and and equivalent for $KS_{k,m}$ and the vacuum term is given by the integrand of equation 3.55. These M equations provide a relation between the plasma perturbation of the M modes at the boundary.

The solution of this system of equations has to be done numerically. This will be the subject of a future paper.

1 - Identification of terms

The terms due the plasma potential energy, given by equation 3.40, clearly show the intuitive structure of equation 3.4, where the stabilizing and potentially destabilizing terms can be identified:

- The stabilizing magnetic terms, described by $\frac{1}{\mu_0}\left|\overline{\mathbf{Q}}\right|^2$, have only a normal and a geodesic component, as the parallel component is minimized to zero. The normal component, reflected in the fifth term of $\widetilde{PV}^0_{k,m}$, relates to $\frac{1}{\mathcal{J}}\frac{\partial X}{\partial \theta}$ of equation 3.9 whereas the geodesic component is reflected in the first terms of $\widetilde{PV}^0_{k,m}$, $\widetilde{PV}^1_{k,m}$ and $\widetilde{PV}^2_{k,m}$ and relates to $\frac{1}{\mathcal{J}}\frac{\partial U}{\partial \theta} - SX$ of equation 3.9.
- The stabilizing plasma compression term is not present as this is minimized to zero by adjusting the parallel component of the perturbation.
- Since the geodesic curvature is related to $\frac{\partial \sigma}{\partial \theta}$ through equation 3.11, the last term of $\widetilde{PV}^0_{k,m}$, along with the part containing the complex conjugate of the second term of $\widetilde{PV}^0_{k,m}$ and the second term of $\widetilde{PV}^{1*}_{m,k}$ represent the destabilizing term due to the pressure gradient. This is the main driving term of the ballooning instability, $-2\left(\xi\cdot\nabla p\right)\left(\kappa\cdot\xi^*\right)$.
- Finally, through equation 3.84, the other part of the second term of $\widetilde{PV}^0_{k,m}$, the third and fourth term of $\widetilde{PV}^0_{k,m}$, the second term of $\widetilde{PV}^1_{k,m}$ and the third terms of $\widetilde{PV}^1_{k,m}$ and $\widetilde{PV}^{1*}_{m,k}$ correspond to the destabilizing term due to the parallel current σ. This is the main driving term of the kink instability, $-\sigma\left(\xi^*\times\mathbf{B}\right)\cdot\overline{\mathbf{Q}}$.

For the plasma kinetic energy, a similar analysis can be easily made, showing that the first term of $\widetilde{KV}^0_{k,m}$ corresponds to the normal part and all the rest to the geodesic part. The parallel part was neglected.

2 - Axisymmetric approximation

In the axisymmetric approximation, employed in [Wil+02] and subsequent papers, a derivation has been done similar to the one in the work presented here, with the major exception that there it is assumed that the plasma equilibrium as well as the perturbations have axisymmetric symmetry. This results in simplifications in the derivations, but also limits the applicability of the results.

The axisymmetric results equivalent to equation 3.62 from [Wil+02] are based on the theory derived in [CHT79]. However, the comparison

between the results from [Wil+02] and the results from this work, with the axisymmetric approximation inserted, is only feasible experimentally, by actually calculating the energy for certain test cases, because the direct axisymmetric results in [Wil+02] are not written in a compact and clearly self-adjoint form, and could be written in a virtually unlimited number of similar ways.

What is shown here, however, is a demonstration of the agreement between the results from [CHT79], on which the direct axisymmetric results are based, with equation 3.4, which is the basis of the 3D theory developed here.

First of all, the "straight field line angle" ω of [Wil+02] is identified as the flux coordinate θ_F which is related to the measure of the length along the magnetic field, since $\mathbf{B} = \frac{1}{\mathcal{J}_F}\boldsymbol{e}_{\theta_F}$ as seen from equation 3.7. Therefore, the following relations between the flux coordinates and the axisymmetric coordinates:

$$\begin{cases} \alpha_F = \zeta_A - \int^{\chi_A} \nu \, d\chi \\ \psi_F = \psi_A \\ \theta_F = \dfrac{1}{q}\displaystyle\int^{\chi_A} \nu \, d\chi \equiv \omega \, , \end{cases} \tag{3.64}$$

to transform from the 3D flux coordinate system $(\alpha_F, \psi_F, \zeta_F)$ used here to the axisymmetric coordinate system $(\psi_A, \chi_A, \zeta_A)$ used in [CHT79] (with the orientation inverted, consistent with subsequent papers), can be found.

Using this, expression 3.27 is simplified for the axisymmetric case and inserted into the expression for the minimizing geodesic perturbation U_m from equation 3.25:

$$\begin{cases} U_m^0 = \dfrac{m}{n}\omega' \left(1 + \dfrac{nq - m}{nq}\dfrac{f^2/R^2}{B^2}\right) \\ \qquad\quad + \dfrac{i}{n}\left(-\dfrac{m}{n}\dfrac{f^2/R^2}{B^2}\dfrac{1}{\nu}\left(\dfrac{\nu}{q}\right)' + \dfrac{1}{\mathcal{J}_A}\dfrac{\partial \mathcal{J}_A}{\partial \psi} + 2\kappa_n\right) \\ U_m^1 = 1 + \dfrac{nq - m}{nq}\dfrac{f^2/R^2}{B^2} \, . \end{cases} \tag{3.65}$$

This expression corresponds to the direct axisymmetric result found in [CHT79, equation 12], which can be seen by inserting the slow dependence $X = X_m e^{-im\omega}$ and $U = U_m e^{-im\omega}$ (the fast ζ-dependence has already been accounted for) and rewriting it for U_m:

$$U_m = \frac{i}{n}\frac{\partial X_m}{\partial \psi} + \frac{m}{n}\omega' X_m + e^{im\omega}\frac{i}{n}Q_{\text{connor}} \, , \tag{3.66}$$

with Q_{connor} given at the bottom of the same page. Indeed, this yields:

$$\begin{aligned} Q_{connor} &= \frac{f^2/R^2}{B^2\nu}\jmath_A Bk_{\|}\left(\frac{1}{n}\frac{\partial X}{\partial\psi}\right) + X\left(\frac{1}{\jmath_A}\frac{\partial\jmath_A}{\partial\psi} + 2\kappa_n\right) \\ &= \left\{\frac{f^2/R^2}{B^2}\left[\frac{nq-m}{nq}\frac{\partial}{\partial\psi} - \left(\frac{m}{n}\left(\frac{1}{\nu}\right)\left(\frac{\nu}{q}\right)' + \omega' im\frac{nq-m}{nq}\right)\right](X_m)\right. \\ &\quad \left. + X_m\left(\frac{1}{\jmath_A}\frac{\partial\jmath_A}{\partial\psi} + 2\kappa_n\right)\right\} e^{-im\omega}\,, \end{aligned} \tag{3.67}$$

which is equivalent to equation 3.65.

Subsequently, inserting the minimized U_m into equation 3.4, assuming axisymmetry and taking the same steps as to get to equation 3.36, inserting fast Fourier modes, [Wil+02, equation 1] could be relatively easily derived, which is the starting point of the theory behind ELITE. Introducing the slow Fourier modes then leads to the axisymmetric equivalent to equation 3.62. As the original derivation in [CHT79] was quite cumbersome, this is a useful alternative that also provides deeper physical insight. The derivation has been verified by the first author but, due to lack of space, is only mentioned here, without reproducing it.

These results hint at the correctness of the 3D theory derived here, at least considering the axisymmetric limit as a verification and the necessary Hermiticity. More thorough comparisons will be the subject of future work.

3.4 Conclusions

Intermediate to high linear n modes in full 3D configurations were investigated theoretically using MHD theory. This is of interest because of peeling-ballooning modes, which are thought to play an important role for the cyclic behavior of ELMs in magnetic fusion reactors and could also clarify some of the issues concerning the limits of the high confinement H-mode observed in many of these devices.

The work presented here builds up on the previous theoretical basis in [GJ68] and [Wil+02], which was based in turn on [CHT79]. The major innovation in this work is that the condition of axisymmetry is relaxed and thus provides results which are more widely applicable than those from previous studies.

Thus, a full 3D treatment of the stability of peeling-ballooning modes with intermediate to high-n mode numbers, valid also near the edge of the

plasma, was developed making use of a Fourier expansion that included a multiple-scale analysis to separate the spectral content of the equilibrium and the perturbation, based on the extended energy principle first cornered by [Ber+58].

The results of the theoretical investigation of this work are a concise Hermitian set of M second order linear differential equations for M poloidally coupled modes resulting from the energy minimization. These equations have to obey two boundary conditions each, one of which is the vanishing of the modes deep inside the plasma and the other one is a relation found by minimizing the surface terms of the energy of the plasma and the vacuum. This system of equations has to be solved numerically, which will be the focus of future work.

The 3D equations derived in this study have been applied to the axisymmetric situation and it has been demonstrated that previous results in this approximation can be reproduced, which provides an initial proof of the correctness of the theoretical model developed here. Further simplified verification of the validity of the 3D approach will be carried out when the numerical implementation of the model is developed. Subsequently, the results will be used to investigate various 3D effects, such as toroidal ripple in tokamaks, the behavior of perturbation coils for the control of ELM, the influence of a TBM module, etc.

Acknowledgments

The authors would like to thank Victor Tribaldos for his input on plasma fusion issues and also Arturo de Pablo for the necessary mathematical interventions.

This research was sponsored in part by DGICYT (Dirección General de Investigaciones Científicas y Tecnológicas) of Spain under Project No. ENE2012-38620-C02-02 and also in part by Comunidad de Madrid Project No. S2009/ENE-1679.

The views and opinions expressed herein do not necessarily reflect those of the ITER Organization.

3.5 Appendices

Calculation of $\mathcal{Q}$

By using

$$\begin{aligned}
&\frac{\partial}{\partial\alpha}\left[\left(-\Theta^{\alpha}+\frac{i}{n}\left(\frac{\partial}{\partial\psi}+\Theta^{\theta}\frac{\partial}{\partial\theta}\right)\right)\left(X_m(\psi)\,e^{i(nq-m)\theta}\right)\right]\\
&=\frac{\partial}{\partial\alpha}\left[\left(-\left(\Theta^{\alpha}+q'\theta+\Theta^{\theta}\frac{nq-m}{n}\right)+\frac{i}{n}\frac{\partial}{\partial\psi}\right)(X_m(\psi))\right]e^{i(nq-m)\theta}\\
&=\left[-\frac{\partial\Theta^{\alpha}}{\partial\alpha}-\frac{\partial\Theta^{\theta}}{\partial\alpha}\frac{nq-m}{n}\right]X_m(\psi)\,e^{i(nq-m)\theta}\,,
\end{aligned} \tag{3.68}$$

equation 3.23 can be described, upon introducing the slow Fourier modes defined in equation 3.24, by the operators Q^0_m and Q^1_m from subsection 4:

$$\begin{cases}
Q^0_m=\left(\dfrac{\partial}{\partial\theta}-\dfrac{nq-m}{n}\dfrac{\partial}{\partial\alpha}\right)\Theta^{\theta}+\dfrac{\Theta^i}{\mathcal{J}}\dfrac{\partial\mathcal{J}}{\partial u^i}+2\kappa_n+\\
\qquad+\dfrac{B_{\alpha}}{\mathcal{J}B^2}\dfrac{\partial}{\partial\theta}\left(\Theta^{\zeta}-\Theta^{\theta}\dfrac{m}{n}\right)+\left(-\Theta^{\zeta}+\Theta^{\theta}\dfrac{m}{n}\right)Q^1_m\\
Q^1_m=-i\,(nq-m)\,\dfrac{B_{\alpha}}{\mathcal{J}B^2}+\dfrac{1}{\mathcal{J}}\dfrac{\partial\mathcal{J}}{\partial\alpha}-\dfrac{1}{\mathcal{J}}\dfrac{\partial}{\partial\theta}\left(\dfrac{B_{\alpha}}{B^2}\right)+2\kappa_g\,.
\end{cases} \tag{3.69}$$

This can be simplified by expressing the pressure balance and the expressions for the curvature components described in subsection 1, explicitly in the (α,ψ,θ) coordinate system, making use of the Clebsch representation for the magnetic field, $\mathbf{B}=\nabla\alpha\times\nabla\psi$. Firstly, the pressure balance becomes:

$$\mu_0 p'\nabla\psi=\frac{1}{\mathcal{J}}\left(\frac{\partial B_{\alpha}}{\partial\theta}-\frac{\partial B_{\theta}}{\partial\alpha}\right)\nabla\alpha+\frac{1}{\mathcal{J}}\left(\frac{\partial B_{\psi}}{\partial\theta}-\frac{\partial B_{\theta}}{\partial\psi}\right)\nabla\psi\,, \tag{3.70}$$

implying that, since the current lies in the magnetic flux surfaces,

$$\frac{\partial B_{\alpha}}{\partial\theta}=\frac{\partial B_{\theta}}{\partial\alpha}\quad\text{and that}\quad\mu_0 p'=\frac{1}{\mathcal{J}}\left(\frac{\partial B_{\psi}}{\partial\theta}-\frac{\partial B_{\theta}}{\partial\psi}\right)\,. \tag{3.71}$$

Introducing this, and the fact that $B_{\theta}=B^2\mathcal{J}$, in the expression for the normal and geodesic curvature:

$$\begin{cases}
\kappa_n=\dfrac{1}{B_{\theta}}\dfrac{\partial B_{\psi}}{\partial\theta}+\dfrac{1}{B_{\theta}}\left(\dfrac{g^{\alpha\psi}}{g^{\psi\psi}}\dfrac{\partial}{\partial\alpha}-\dfrac{\partial}{\partial\psi}+\dfrac{g^{\theta\psi}}{g^{\psi\psi}}\dfrac{\partial}{\partial\theta}\right)\left(\dfrac{B_{\theta}}{2}\right)-\\
\qquad-\dfrac{1}{\mathcal{J}}\left(\dfrac{g^{i\psi}}{g^{\psi\psi}}\dfrac{\partial}{\partial u^i}\right)\left(\dfrac{\mathcal{J}}{2}\right)\\
\kappa_g=\dfrac{\mathcal{J}}{B^2_{\theta}}\left(B_{\theta}\dfrac{\partial}{\partial\alpha}-B_{\alpha}\dfrac{\partial}{\partial\theta}\right)\left(\dfrac{B_{\theta}}{2\mathcal{J}}\right)\,.
\end{cases} \tag{3.72}$$

Therefore, the operator Q^0_m becomes:

$$\begin{aligned} Q^0_m &= \frac{nq-m}{n}\frac{1}{B_\theta}\left(B_\alpha\frac{\partial}{\partial\theta}-B_\theta\frac{\partial}{\partial\alpha}\right)\Theta^\theta+\frac{\partial\Theta^\theta}{\partial\theta}+\frac{B_\alpha}{B_\theta}\left(\frac{\partial\Theta^\alpha}{\partial\theta}+q'\right)+\\ &+\frac{2}{B_\theta}\frac{\partial B_\psi}{\partial\theta}+\frac{1}{B_\theta}\left(\Theta^\alpha\frac{\partial}{\partial\alpha}-\frac{\partial}{\partial\psi}+\Theta^\theta\frac{\partial}{\partial\theta}\right)B_\theta+\\ &+\left(-\Theta^\zeta+\Theta^\theta\frac{m}{n}\right)Q^1_m\\ &=\frac{nq-m}{n}\frac{\mathcal{J}}{B_\theta}\mathbf{B}\cdot\nabla\psi\times\nabla\Theta^\theta+q'\frac{B_\alpha}{B_\theta}+\frac{1}{B_\theta}\left(\frac{\partial B_\psi}{\partial\theta}-\frac{\partial B_\theta}{\partial\psi}\right)+\\ &+\left(-\Theta^\zeta+\Theta^\theta\frac{m}{n}\right)Q^1_m\\ &=\frac{B_\alpha q'+\mathcal{J}\mu_0 p'}{B_\theta}+\left(-\Theta^\zeta+\Theta^\theta\frac{m}{n}\right)Q^1_m+\\ &+\frac{nq-m}{n}\frac{\mathcal{J}\mathbf{B}\cdot\nabla\psi\times\nabla\Theta^\theta}{B_\theta}\,, \end{aligned} \tag{3.73}$$

with $\Theta^\zeta=\Theta^\alpha+q'\theta+q\Theta^\theta$. using the same technique, the operator Q^1_m simplifies to:

$$Q^1_m=-i\,(nq-m)\,\frac{B_\alpha}{B_\theta}\,. \tag{3.74}$$

The axisymmetric limit of these equations corresponds to the work done by [CHT79] and is discussed in subsection 2.

Minimization of plasma potential energy

The series of equation 3.18 is introduced into the plasma potential energy, given by equation 3.4, making use of the expressions for the adjoint operators U_k^T and DU_k^T of 4. This is done here term by term.

Line bending term

The stabilizing magnetic terms were described in subsection 1 by the term $\frac{1}{\mu_0}|Q_\perp|^2$. The parallel component, also called the magnetic compression term, was minimized to zero by the condition of equation 3.25 and the two perpendicular components, also called the line bending terms, are to be calculated independently from

$$\frac{1}{\mu_0}\left(\frac{1}{|\nabla\psi|^2}\left|\frac{1}{\mathcal{J}}\frac{\partial X}{\partial\theta}\right|^2+\frac{|\nabla\psi|^2}{B^2}\left|\frac{1}{\mathcal{J}}\frac{\partial U}{\partial\theta}-SX\right|^2\right)\,, \tag{3.75}$$

Inserting the series of equation 3.18 then results in a contribution

$$\frac{1}{\mu_0}\frac{1}{\mathcal{J}^2\left|\nabla\psi\right|^2}\left|\sum_m i\left(nq-m\right)X_m e^{i[n\alpha+(nq-m)\theta]}\right|^2, \tag{3.76}$$

from the normal component, which directly leads to

$$\frac{1}{\mu_0}\sum_{k,m}X_k^* e^{i(k-m)\theta}\left[\left\{\left(nq-k\right)\left(nq-m\right)\frac{1}{\mathcal{J}^2\left|\nabla\psi\right|^2}\right\}\right]X_m\,, \tag{3.77}$$

and

$$\frac{1}{\mu_0}\frac{\left|\nabla\psi\right|^2}{\mathcal{J}^2B^2}\left|\sum_m\left[DU_m^0-\mathcal{J}S+DU_m^1\frac{i}{n}\frac{\partial}{\partial\psi}\right](X_m)\,e^{i[n\alpha+(nq-m)\theta]}\right|^2, \tag{3.78}$$

from the geodesic component. Extracting the different orders in the ψ derivatives:

$$\begin{aligned}
&\frac{1}{\mu_0}\sum_{k,m}X_k^* e^{i(k-m)\theta}\left[\left(DU_k^{T,0}-\mathcal{J}S+DU_k^{T,1}\frac{i}{n}\frac{\partial}{\partial\psi}\right)\right.\\
&\qquad\left.\left(\frac{\left|\nabla\psi\right|^2}{\mathcal{J}^2B^2}\left(DU_m^0-\mathcal{J}S+DU_m^1\frac{i}{n}\frac{\partial}{\partial\psi}\right)\right)(X_m)\right]\\
=&\frac{1}{\mu_0}\sum_{k,m}X_k^* e^{i(k-m)\theta}\left[\left\{DU_k^{T,1}\frac{\left|\nabla\psi\right|^2}{\mathcal{J}^2B^2}DU_m^1\right\}\left(\frac{i}{n}\right)^2\frac{\partial^2}{\partial\psi^2}+\right.\\
&\quad+\left\{\left(DU_k^{T,0}-\mathcal{J}S\right)\frac{\left|\nabla\psi\right|^2}{\mathcal{J}^2B^2}DU_m^1+DU_k^{T,1}\frac{\left|\nabla\psi\right|^2}{\mathcal{J}^2B^2}\left(DU_m^0-\mathcal{J}S\right)+\right.\\
&\qquad\left.\left.+DU_k^{T,1}\frac{i}{n}\frac{\partial}{\partial\psi}\left(\frac{\left|\nabla\psi\right|^2}{\mathcal{J}^2B^2}DU_m^1\right)\right\}\left(\frac{i}{n}\right)\frac{\partial}{\partial\psi}+\right.\\
&\quad+\left\{\left(DU_k^{T,0}-\mathcal{J}S\right)\frac{\left|\nabla\psi\right|^2}{\mathcal{J}^2B^2}\left(DU_m^0-\mathcal{J}S\right)+\right.\\
&\qquad\left.\left.+DU_k^{T,1}\frac{i}{n}\frac{\partial}{\partial\psi}\left(\frac{\left|\nabla\psi\right|^2}{\mathcal{J}^2B^2}\left(DU_m^0-\mathcal{J}S\right)\right)\right\}\right](X_m)\,,
\end{aligned} \tag{3.79}$$

with the surface term, discussed in equation 3.32 for the adjoint operator

of U_k^* equal to:

$$-\frac{1}{\mu_0}\left[\mathcal{J}\frac{i}{n}DU_k^{1*}X_k^* e^{i(k-m)\theta}\frac{|\nabla\psi|^2}{\mathcal{J}^2B^2}\left(DU_m^0 - \mathcal{J}S + DU_m^1\frac{i}{n}\frac{\partial}{\partial\psi}\right)(X_m)\right]_{\psi_a}^{\psi_s} . \tag{3.80}$$

ballooning term

The term that can be driven unstable by a pressure gradient oriented in the opposite direction than the curvature is the origin of the ballooning and interchange instability and has a contribution to the plasma potential energy equal to

$$-2Xp'\left(X^*\kappa_n + U^*\kappa_g\right) , \tag{3.81}$$

that leads to

$$\begin{aligned}&\sum_{k,m}(-2)\,X_k^* e^{i(k-m)\theta}\left[p'\kappa_n X_m + U_k^T\left(\kappa_g p' X_m\right)\right]\\ =&\sum_{k,m}(-2)\,X_k^* e^{i(k-m)\theta}\left[\left\{\kappa_g p' U_k^{T,1}\right\}\frac{i}{n}\frac{\partial}{\partial\psi}+\right.\\ &\left.+\left\{p'\kappa_n + \left(U_k^{T,0} + U_k^{T,1}\frac{i}{n}\frac{\partial}{\partial\psi}\right)(\kappa_g p')\right\}\right](X_m) ,\end{aligned} \tag{3.82}$$

and a surface term

$$\left[2\mathcal{J}\frac{i}{n}U_k^{1*}X_k^* e^{i(k-m)\theta}p'\kappa_g X_m\right]_{\psi_a}^{\psi_s} . \tag{3.83}$$

kink term

The kink term represents the term that can be driven unstable by a parallel current. It has a contribution equal to

$$\frac{1}{\mathcal{J}}\frac{\partial}{\partial\theta}\left(\sigma X^*\right)U + S\sigma X^* X + \sigma\frac{U^*}{\mathcal{J}}\frac{\partial X}{\partial\theta} , \tag{3.84}$$

which leads to

$$\begin{aligned}
&\sum_{k,m} X_k^* e^{i(k-m)\theta} \left[\frac{1}{\mathcal{J}} \frac{\partial \sigma}{\partial \theta} U_m(X_m) - i(nq-k) \frac{\sigma}{\mathcal{J}} U_m(X_m) + S\sigma X_m + \right. \\
&\qquad \left. + U_k^T \left(\frac{\sigma}{\mathcal{J}} i(nq-m) X_m \right) \right] \\
&= \sum_{k,m} X_k^* e^{i(k-m)\theta} \left[\left\{ \frac{\sigma}{\mathcal{J}} \left(U_k^{T,1} i(nq-m) - U_m^1 i(nq-k) \right) - \right. \right. \\
&\qquad \left. - 2p'\kappa_g U_m^1 \right\} \frac{i}{n} \frac{\partial}{\partial \psi} + \\
&\qquad + \left\{ \frac{\sigma}{\mathcal{J}} \left(i(nq-m) U_k^{T,0} - i(nq-k) U_m^0 \right) + S\sigma - \right. \\
&\qquad \left. \left. - U_k^{T,1} \frac{1}{n} \frac{\partial}{\partial \psi} \left(\frac{\sigma}{\mathcal{J}} (nq-m) \right) - 2p'\kappa_g U_m^0 \right\} \right] X_m \, ,
\end{aligned} \tag{3.85}$$

and surface term

$$\left[\frac{1}{n} U_k^{1*} X_k^* e^{i(k-m)\theta} \sigma (nq-m) X_m \right]_{\psi_a}^{\psi_s} . \tag{3.86}$$

Hermitian form

Combining the contributions from all the terms, the expression for the plasma potential energy now has the form:

$$\frac{1}{2} \sum_{k,m} \int_{\psi_a}^{\psi_s} d\psi \left[\int d\theta \mathcal{J} X_k^* e^{i(k-m)\theta} PV_{k,m} \right] (X_m) \, , \tag{3.87}$$

with

$$PV_{k,m} = PV_{k,m}^0 + PV_{k,m}^1 \left(\frac{i}{n} \right) \frac{d}{d\psi} + PV_{k,m}^2 \left(\frac{i}{n} \right)^2 \frac{d^2}{d\psi^2} \, . \tag{3.88}$$

where the coefficients $PV_{k,m}^i$ can be simplified to a compact and visibly Hermitian form.

The coefficient $PV^0_{k,m}$ is given by a part

$$\begin{aligned}
\widetilde{PV}^0_{k,m} = &\frac{1}{\mu_0}\left\{(nq-k)(nq-m)\frac{1}{\mathcal{J}^2|\nabla\psi|^2}\right\}- \\
&-2\left\{p'\kappa_n+\left(U^{T,0}_k+U^{T,1}_k\frac{i}{n}\frac{\partial}{\partial\psi}\right)(\kappa_g p')\right\} \\
&+\frac{1}{\mu_0}\left\{\left(DU^{T,0}_k-\mathcal{J}S\right)\frac{|\nabla\psi|^2}{\mathcal{J}^2B^2}\left(DU^0_m-\mathcal{J}S\right)+\right. \\
&\qquad\left.+DU^{T,1}_k\frac{i}{n}\frac{\partial}{\partial\psi}\left(\frac{|\nabla\psi|^2}{\mathcal{J}^2B^2}\left(DU^0_m-\mathcal{J}S\right)\right)\right\} \\
&+\left\{\frac{\sigma}{\mathcal{J}}\left(i(nq-m)U^{T,0}_k-i(nq-k)U^0_m\right)+S\sigma-\right. \\
&\qquad\left.-U^{T,1}_k\frac{1}{n}\frac{\partial}{\partial\psi}\left(\frac{\sigma}{\mathcal{J}}(nq-m)\right)-2p'\kappa_g U^0_m\right\} \\
=&\frac{1}{\mu_0}\frac{|\nabla\psi|^2}{\mathcal{J}^2B^2}\left(DU^{0*}_k-\mathcal{J}S\right)\left(DU^0_m-\mathcal{J}S\right)+\frac{1}{\mathcal{J}}\frac{\partial\sigma}{\partial\theta}\left(U^{0*}_k+U^0_m\right)+ \\
&+\frac{\sigma}{\mathcal{J}}\left(i(nq-m)U^{0*}_k-i(nq-k)U^0_m\right)-2p'\kappa_n+S\sigma+ \\
&+\frac{1}{\mu_0}\frac{(nq-k)(nq-m)}{\mathcal{J}^2|\nabla\psi|^2},
\end{aligned} \tag{3.89}$$

and some more terms equal to:

$$\begin{aligned}
&\frac{1}{\mathcal{J}}\frac{\partial\sigma}{\partial\theta}\frac{1}{\mathcal{J}}\frac{i}{n}\frac{\partial}{\partial\psi}\left(U^{1*}_k\mathcal{J}\right)+U^{1*}_k\frac{i}{n}\frac{\partial}{\partial\psi}\left(\frac{1}{\mathcal{J}}\frac{\partial\sigma}{\partial\theta}\right)- \\
&\quad-U^{1*}_k\frac{1}{n}\frac{\partial}{\partial\psi}\left(\frac{\sigma}{\mathcal{J}}(nq-m)\right)+\frac{DU^{1*}_k}{\mu_0}\frac{i}{n}\frac{\partial}{\partial\psi}\left(\frac{|\nabla\psi|^2}{\mathcal{J}^2B^2}\left(DU^0_m-\mathcal{J}S\right)\right)+ \\
&\quad+\frac{1}{\mathcal{J}}\frac{i}{n}\frac{\partial}{\partial\psi}\left(U^{1*}_k\mathcal{J}\right)\frac{\sigma}{\mathcal{J}}i(nq-m)+ \\
&\quad+\frac{1}{\mathcal{J}}\frac{i}{n}\frac{\partial}{\partial\psi}\left(DU^{1*}_k\mathcal{J}\right)\left(\frac{1}{\mu_0}\frac{|\nabla\psi|^2}{\mathcal{J}^2B^2}\left(DU^0_m-\mathcal{J}S\right)\right) \\
&=\frac{1}{\mathcal{J}}\frac{i}{n}\frac{\partial}{\partial\psi}\left(U^{1*}_k\left(\frac{\partial\sigma}{\partial\theta}+\sigma i(nq-m)\right)+DU^{1*}_k\frac{|\nabla\psi|^2}{B^2}\left(\frac{DU^0_m}{\mathcal{J}}-S\right)\right),
\end{aligned} \tag{3.90}$$

which are proportional to the normal derivative of a part of the coefficient $PV^1_{k,m}$, to which the surface term $SV^0_{k,m}$ is proportional as well.

The coefficient $PV^1_{k,m}$ is given by

$$\begin{aligned}
PV^1_{k,m} = \frac{1}{\mu_0}\Bigg\{ & \left(DU^{T,0}_k - \mathcal{J}S\right)\frac{|\nabla\psi|^2}{\mathcal{J}^2B^2}DU^1_m + \\
& + DU^{T,1}_k\frac{|\nabla\psi|^2}{\mathcal{J}^2B^2}\left(DU^0_m - \mathcal{J}S\right) + \\
& + DU^{T,1}_k\frac{i}{n}\frac{\partial}{\partial\psi}\left(\frac{|\nabla\psi|^2}{\mathcal{J}^2B^2}DU^1_m\right)\Bigg\} \\
& + \left\{\frac{\sigma}{\mathcal{J}}\left(U^{T,1}_k i\left(nq-m\right) - U^1_m i\left(nq-k\right)\right) - 2p'\kappa_g U^1_m\right\} \\
& - 2\left\{\kappa_g p' U^{T,1}_k\right\} \\
= & \frac{1}{\mu_0}\frac{|\nabla\psi|^2}{\mathcal{J}^2B^2}\left[\left(DU^{0*}_k - \mathcal{J}S\right)DU^1_m + \left(DU^0_m - \mathcal{J}S\right)DU^{1*}_k\right] \\
& + \frac{1}{\mathcal{J}}\frac{\partial\sigma}{\partial\theta}\left(U^1_m + U^{1*}_k\right) + \frac{\sigma}{\mathcal{J}}\left(U^{1*}_k i\left(nq-m\right) - U^1_m i\left(nq-k\right)\right) \\
& + \frac{1}{\mu_0}\frac{1}{\mathcal{J}}\frac{i}{n}\frac{\partial}{\partial\psi}\left(\frac{|\nabla\psi|^2}{\mathcal{J}B^2}DU^1_m DU^{1*}_k\right) ,
\end{aligned} \tag{3.91}$$

where the last term is proportional to the normal derivative of the coefficient $PV^2_{k,m}$. The other terms of $PV^1_{k,m}$ can be written as the sum of:

$$\widetilde{PV}^1_{k,m} = \frac{1}{\mu_0}\frac{|\nabla\psi|^2}{\mathcal{J}^2B^2}\left(DU^{0*}_k - \mathcal{J}S\right)DU^1_m + \frac{U^1_m}{\mathcal{J}}\left(\frac{\partial\sigma}{\partial\theta} - \sigma i\left(nq-k\right)\right) , \tag{3.92}$$

and its conjugate. Also, the surface term $PS^1_{k,m}$ is proportional to $PV^2_{k,m}$.

The coefficient $PV^2_{k,m}$ is given by

$$PV^2_{k,m} = \widetilde{PV}^2_{k,m} = \frac{1}{\mu_0}\frac{|\nabla\psi|^2}{\mathcal{J}^2B^2}DU^1_m DU^{1*}_k , \tag{3.93}$$

which cannot be simplified any further.

Bringing it all together results in the terms $PV^i_{k,m}$ stated in subsection 5.

Chapter 4

The PB3D Code

The content of this chapter was published in the ***Journal of Computational Physics*** *by T. Weyens, R. Sánchez, L. García and A. Loarte under the name* ***PB3D: A new code for edge 3-D ideal linear peeling-ballooning stability*** *[Wey+16]. The terms of the Creative Commons Attribution - Non Commercial - No Derivatives License (CC BY NC ND) apply. The typography has been adapted to the style of this document.*

In chapter 3, ideal linear high-n theory for 3-D edge toroidal magnetic configurations has been created, with the end result being a coupled set of second-order ordinary linear differential equations in the normal components of the Fourier modes, containing an eigenvalue. The solution of this system of equations has to be done through numerical means. This is where the new numerical code **PB3D** (**P**eeling-**B**allooning in **3**-**D**) comes into play.

This chapter describes how the PB3D code has been designed and implemented. It serves to illustrate the numerical aspects as well, such as the algorithms that were used. Furthermore, the various external libraries are mentioned, of which use is made. All of this is explained through the vision of creating a dedicated, fast code.

Finally, a first example of the applicability of the code is presented, that serves as a first indication for the usefulness of being able to simulate 3-D aspects.

abstract

A new numerical code **PB3D** (**P**eeling-**B**allooning in **3**-**D**) is presented. It implements and solves the intermediate-to-high-n ideal linear magnetohydrodynamic stability theory extended to full edge 3-D magnetic toroidal configurations in previous work [Wey+14]. The features that make PB3D unique are the assumptions on the perturbation structure through intermediate-to-high mode numbers n in general 3-D configurations, while allowing for displacement of the plasma edge. This makes PB3D capable of very efficient calculations of the full 3-D stability for the output of multiple equilibrium codes. As first verification, it is checked that results from the stability code MISHKA [Mik+97], which considers axisymmetric equilibrium configurations, are accurately reproduced, and these are then successfully extended to 3-D configurations, through comparison with COBRA [Sán+00], as well as using checks on physical consistency. The non-intuitive 3-D results presented serve as a tentative first proof of the capabilities of the code.

keywords: PB3D; ideal linear MHD stability; peeling-ballooning; high-n; edge; 3-D

4.1 Introduction

Magnetohydrodynamics (MHD) theory is a mathematically convenient and widely used tool in the study of hot plasmas, such as the ones appearing in toroidal magnetic confinement devices, such as tokamaks and stellarators, even in regions in parameter space where, strictly speaking, the assumptions on which it is based are less valid. Nonetheless, MHD instabilities often lead to a rather hard limit on the stability of toroidal plasma configurations. Hence, it is important to study MHD in detail and the topic of interest in this work is the global ideal linear intermediate-to-high-n MHD stability of edge 3-D toroidal equilibrium configurations, where n is a measure of localization of the instabilities around the magnetic field lines.

The reason for focusing on the high-n assumption (also called "short-wavelength"), is that the resulting modes can be easily excited and can grow quickly, while at the same time spanning a large fraction of the plasma cross-section, which can give them the power to couple energy from the

hot plasma core to the cold surface [GJ68, sec. 7]. However, modes with more intermediate n numbers can also be important. The so-called *peeling-ballooning modes*, for example, are among the most important instabilities, where peeling modes have a distinct intermediate-n nature, whereas ballooning modes are described accurately through high-n theory. Among other things, they have been shown to be a prime candidate to explain the periodic outbursts observed experimentally, called ELMs [Wil+02], which can cause large power fluxes to the components in fusion devices and deteriorate plasma confinement [Loa+14].

Here, the term intermediate-to-high-n therefore refers to an expansion in the parameter n accurate not just up to leading order in n, but also to second order. To preserve clarity, furthermore, in the remainder of this work, the term "high-n" is understood to include "intermediate-n" as well.

The high-n assumption was pioneered theoretically some time ago in the bulk plasma of axisymmetric configurations [CHT79], after which it was extended to edge configurations [Con+98], and also to bulk 3-D configurations [DG83]. An important common aspect of these theories, however, is that they all make use of eikonal formulations for the spatial behavior (and normal modes for the time behavior) of the perturbation vector $\boldsymbol{\xi}(\mathbf{r}, t)$ of the form

$$\boldsymbol{\xi}(\mathbf{r}, t) = \boldsymbol{\xi}(\mathbf{r})\, e^{i\omega t} = \hat{\boldsymbol{\xi}}(\mathbf{r})\, e^{inS(\mathbf{r})} e^{i\omega t}\,, \tag{4.1}$$

where ω is the (complex) frequency of the normal mode and S is the eikonal, defined through

$$\mathbf{B} \cdot \nabla S = 0\,, \tag{4.2}$$

with $\mathbf{B}$ the magnetic field, which through the large factor n decouples the derivatives into a slow derivative parallel to the magnetic field and a fast derivative perpendicular to it. Subsequently, through judicious choices of the form and behavior of the amplitude $\hat{\boldsymbol{\xi}}$, this carries on to decoupling of the MHD equations in different orders. Finally, the lowest order is then decoupled for the flux surfaces, and yields an ordinary differential equation[1], usually known as the *ballooning equation*, that describes the stability for every flux surface separately. Higher orders typically yield the shape of the amplitude function $\hat{\boldsymbol{\xi}}$.

For a full description of a general high-n mode, however, an eikonal cannot be used easily, as it suffers from important limitations, such as the lack of periodicity [HM03] which makes it difficult to reconstruct periodic solutions, the assumed shapes for the perturbation amplitudes, and the difficulty of treating the cases in which the edge of the plasma is perturbed.

[1] Or possibly a set of two if the plasma is compressible. [DG83]

Because of these reasons, as an alternative, general Fourier modes of the form $\sim \hat{\xi}(\psi) \exp[n\zeta - m\theta]$ can be used instead in a (ψ, θ, ζ) coordinate system with ψ a flux coordinate and θ poloidal and ζ toroidal angles. A flux coordinate is a function that monotonously varies across the nested flux surfaces of ideal plasmas (i.e. without resistivity), such as enclosed volume or flux; and it is convenient to deform the angular coordinates so that the magnetic field becomes straight [Boo05]. Furthermore, the correct treatment of edge-perturbed plasmas is also possible, through formally considering the toroidal system as the union of the plasma and a surrounding vacuum, connected by an edge that in theory can support a jump in the magnetic field through a skin current, and by investigating the perturbed potential and kinetic energy of the whole system; a strategy referred to as the *extended energy principle* [GP04].

For axisymmetric equilibria, this was the approach followed by the numerical code ELITE [Wil+02]. In PB3D the approach is more general, as full 3-D configurations are considered, and when they are restricted to axisymmetry, this leads to the same range of validity as the original ELITE[2]. In 3-D, one would expect greater complexity and computational requirements, but an important finding of the theory behind PB3D [Wey+14], is that the numerical problem to be solved is not substantially more complex than that for the axisymmetric case, as the fluted (see subsec. 2) high-n nature of the modes leads naturally to a separation of scales that reduces the dimension of the problem by one.

Apart from this, to motivate the search for a 3-D solution, some examples of 3-D configurations include the breaking of axisymmetry, such as due to the usage of ferromagnetic Tritium Breeder Modules in ITER, discrete toroidal field coils in tokamaks that introduce a toroidal field ripple, or axisymmetry-breaking resonance magnetic perturbation (RMP) coils for ELM control that work by explicitly breaking axisymmetry. Recently, these topics have started attracting ample interest, and mostly so for the RMP coils, as ELM control is becoming very important in the next-generation tokamaks such as ITER.

In [Cha+13], for example, the 3-D corrugation of the plasma edge was identified as one of the key ingredients in the mechanism of ELM control through RMPs, (the simulation of which is a task for which PB3D would be very well suited). As an alternative to full 3-D treatments, perturbative approaches to 3-D effects were used in both [HN13] and [Heg14], where the

[2] ELITE has recently been extended to include a higher order in the expansion in n, not yet present in the PB3D theory.

former is geared mostly towards configurations with magnetic islands, and the latter towards 3-D modifications of otherwise axisymmetric equilibria. Finally, work with the CAS3D code that is able to perform 3-D stability analysis, but which does not employ the high-n assumption, was presented already in [Nüh96]. That research was geared towards stellarators, which are fully 3-D configurations, that can also suffer from instability issues, and where perturbative approaches are not possible.

After this introduction to and situation of the current work, the theoretical model derived in [Wey+14] is shortly summarized in the next section. Subsequently, in sec. 4.3, numerical aspects of the new PB3D code, such as the discretization methods and employed algorithms, are discussed. Following this, in sec. 4.4 information is given about the verification of PB3D, making use of comparisons with numerical codes MISHKA [Mik+97] and COBRA [Sán+00], as well as checks on physical consistency. Finally, in sec. 4.5, a summary follows.

4.2 Theoretical model

The theoretical model on which the PB3D code is based, was developed in [Wey+14] and is shortly summarized here. First, some general information is given about the extended energy principle that is used and afterwards the description of the magnetic field is discussed, as well as the specific form of the perturbations used in this work. Finally, stability is investigated, making use of minimized energy.

1 - Extended energy principle

As discussed in the previous section, the extended principle is used for normal modes with frequency ω. This leads to expressions for the perturbed potential and kinetic energy for the system composed of plasma connected to surrounding vacuum at the plasma edge. It is advantageous to make use of the *Rayleigh Quotient* formulation which identifies eigenvalues ω^2 of the normal modes with stationary values of the quotient Λ, defined as the ratio of perturbed potential and kinetic energy:

$$\Lambda\left[\boldsymbol{\xi}, \mathbf{Q}_\mathrm{v}\right] \equiv \frac{\delta W\left[\boldsymbol{\xi}, \mathbf{Q}_\mathrm{v}\right]}{K\left[\boldsymbol{\xi}\right]} \equiv \frac{\delta W_\mathrm{p}\left[\boldsymbol{\xi}\right] + \delta W_\mathrm{s}\left[\boldsymbol{\xi}\right] + \delta W_\mathrm{v}\left[\mathbf{Q}_\mathrm{v}\right]}{\frac{1}{2}\int_\mathrm{p} \rho \left|\boldsymbol{\xi}\right|^2 \mathrm{d}\mathbf{r}} \,, \tag{4.3}$$

where ρ is the plasma mass density and $\boldsymbol{\xi}$ and $\mathbf{Q}_\mathrm{v}$ are the plasma, respectively the vacuum magnetic field perturbation, and where it is illustrated that the perturbed potential energy is composed of parts corresponding to the

plasma (subscript p), the edge surface (s) and the surrounding vacuum (v):

$$\begin{cases} \delta W_\mathrm{p}\left(\boldsymbol{\xi}\right) = \frac{1}{2}\int_\mathrm{p} \mathrm{d}\mathbf{r}\left[\frac{\left|\mathbf{Q}\right|^2}{\mu_0} - \boldsymbol{\xi}^*\cdot\mathbf{J}\times\mathbf{Q} + \gamma \mathrm{p}\left|\nabla\cdot\boldsymbol{\xi}\right|^2 + \left(\boldsymbol{\xi}\cdot\nabla\mathrm{p}\right)\nabla\cdot\boldsymbol{\xi}^*\right] \\ \delta W_\mathrm{s}\left(\boldsymbol{\xi}\right) = \frac{1}{2}\int_\mathrm{s} \mathrm{dS}\left[\left|\mathbf{n}\cdot\boldsymbol{\xi}\right|^2\mathbf{n}\cdot\left[\!\left[\nabla\left(\mu_0\mathrm{p} + \frac{\mathrm{B}^2}{2}\right)\right]\!\right]\right]_\mathrm{s} \\ \delta W_\mathrm{v}\left(\mathbf{Q}_\mathrm{v}\right) = \frac{1}{2}\int_\mathrm{v} \mathrm{d}\mathbf{r}\left[\frac{\left|\mathbf{Q}_\mathrm{v}\right|^2}{\mu_0}\right] . \end{cases} \tag{4.4}$$

Here, $\mathbf{J}$ is the plasma current, defined through $\mu_0\mathbf{J} = \nabla\times\mathbf{B}$, p is the plasma pressure, γ the adiabatic constant, $\mathbf{n}$ the unit vector normal to the plasma edge surface and the quantity $\mathbf{Q}$ is the perturbation of the magnetic field

$$\mathbf{Q} = \nabla\times\left(\boldsymbol{\xi}\times\mathbf{B}\right) . \tag{4.5}$$

An advantage of the generalized energy principle, is that the perturbations only need to satisfy the *essential boundary conditions*

$$\begin{cases} \boldsymbol{\xi} \text{ regular} & \text{(on p)} , \\ \mathbf{n}\cdot\nabla\times\left(\boldsymbol{\xi}\times\mathbf{B}_\mathrm{v}\right) = \mathbf{n}\cdot\mathbf{Q}_\mathrm{v} & \text{(on s)} , \\ \mathbf{n}\cdot\mathbf{Q}_\mathrm{v} = 0 & \text{(on exterior wall)} , \end{cases} \tag{4.6}$$

as the natural boundary conditions are already taken into account automatically.

2 - Magnetic field and Fourier modes

Fourier modes are used in the angular coordinates θ and ζ, which in this work are chosen so that the magnetic field

$$\mathbf{B} = \nabla\zeta\times\nabla\psi + \mathrm{q}(\psi)\nabla\psi\times\nabla\theta , \tag{4.7}$$

appears straight with its pitch constant on each flux surface and given by the *safety factor* $\mathrm{q}\left(\psi\right) = \frac{\mathrm{d}\zeta}{\mathrm{d}\theta}$, with as flux coordinate the scaled enclosed poloidal flux $\psi = \frac{\psi_\mathrm{pol}}{2\pi}$. To further simplify the situation, the toroidal coordinate, is replaced by the *field line label* $\alpha = \zeta - \mathrm{q}\theta$, the resulting magnetic field being proportional to the covariant unit vector in the θ direction:

$$\mathbf{B} = \frac{1}{\mathcal{J}}\boldsymbol{e}_\theta , \tag{4.8}$$

with $\mathcal{J}$ the Jacobian, which is why θ is called the *parallel coordinate* or *magnetic coordinate*.[3] In the resulting $\left(\alpha,\psi,\theta\right)$ coordinate system, the Fourier

[3] This is the for the case when the enclosed poloidal flux is used as normal coordinate. If the toroidal flux is used, the parallel coordinate is not θ but ζ. PB3D is capable of this, but the rest of the discussion is limited to using the poloidal flux as normal coordinate.

modes then have the form:

$$\xi(\alpha, \psi, \theta) = \hat{\xi}(\psi)\, e^{i[(nq-m)\theta - n\alpha]} . \tag{4.9}$$

From basic stability considerations, it can be seen that acceptable high-n modes must be *fluted* [Fre87, sec. 8.11], meaning that their parallel dependence should be of the same order as the equilibrium variations, as opposed to their fast perpendicular dependence. The introduction of the α coordinate then leads to a natural separation of these two length scales that decouples the modes that belong to different field lines as is illustrated in [Wey+14, fig. 1]. This is expressed in the exponent of eq. 4.9 through the condition $\frac{nq-m}{n} \ll 1$.

3 - Minimized perturbed energy

Employing the Fourier form of the perturbations of eq. 4.9 in the expressions for the perturbed energies of eqs. 4.4, through the analytic minimization of certain stabilizing term the different components of the perturbation can all be written in terms of the normal component $X = \nabla\psi \cdot \xi$, and through the decoupling of modes belonging to different field lines, the mode vector of the perturbation, $\mathbf{X} = (X_1, X_2, \ldots, X_M)^T$ contains only M components due to the θ dimension. The resulting expressions for the perturbed plasma potential and kinetic potential then reduce to integrals over ψ of bi-linear form relating the vector of the modes of ξ to the perturbed energies:

$$\delta W_p = \frac{1}{2}\int_v \mathbf{X}^* \overline{\mathbf{P}} \mathbf{X}\, d\psi , \tag{4.10}$$

$$K = \frac{1}{2}\int_v \mathbf{X}^* \overline{\mathbf{K}} \mathbf{X}\, d\psi , \tag{4.11}$$

where the tensors $\overline{\mathbf{P}}$ and $\overline{\mathbf{K}}$ are both of the same form, so they can be bundled by defining the Lagrangian

$$\overline{\mathbf{L}} = \overline{\mathbf{P}} - \omega^2 \overline{\mathbf{K}} , \tag{4.12}$$

with elements $\overline{L}_{k,m}$ given by, using non-standard terminology, *magnetic average modes* of the quantities $L_{k,m}$, defined as

$$\overline{L}_{k,m} = \int_\alpha \mathcal{J} e^{i(k-m)\theta} L_{k,m}\, d\theta , \tag{4.13}$$

where the integration runs along a field line with label α. Note that this is a consequence of the fact that only modes pertaining to the same field

lines are coupled. Also note that the Lagrangian formulation is equivalent to using the Rayleigh Quotient.

The quantities $L_{k,m} = P_{k,m} - \omega^2 K_{k,m}$ are second order differential operators with elements of the form

$$L_{k,m} = L^0_{k,m} + \frac{\overleftarrow{d}}{d\psi} L^{1*}_{m,k} + L^1_{k,m} \frac{\overrightarrow{d}}{d\psi} + \frac{\overleftarrow{d}}{d\psi} L^2_{k,m} \frac{\overrightarrow{d}}{d\psi} , \tag{4.14}$$

which are Hermitian, since $L^0_{k,m}$ and $L^2_{k,m}$ are individually so. This expresses the fact that there are no losses in ideal MHD. The arrows in above equation indicate the direction in which the derivatives are to be taken.

Apart from this, the perturbed energy of the vacuum reduces to a surface term $\delta^{vac}_{k,m}$, and it can be shown that a perturbed skin current on the plasma edge is not allowed as it would be very stabilizing, so that the contribution due to the edge is zero.

Finally, Euler minimization of the Rayleigh Quotient in the different functions $X^*_k(\psi)$ leads to a coupled set of second-order ordinary differential equations (ODEs) of the functions $X_m(\psi)$ that contain an eigenvalue ω^2 due to the time derivatives present in the kinetic energy as related to the square of the velocity. Furthermore, the necessary partial integrations that translate normal derivatives of the complex conjugate functions X^*_k, introduce boundary terms at the edges of the integration boundaries in ψ, which leads to a contribution at the plasma edge, which is added to the contribution $\delta^{vac}_{k,m}$ due to the vacuum—the contribution at the plasma center vanishes as the perturbations are assumed to vanish there; core instabilities are not the interest of high-n theory.

Therefore, the resulting system of equations is of the form

$$\sum_m \left\{ \bar{L}^0_{k,m} X_m - \left(\bar{L}^{1*}_{m,k} X_m \right)' + \bar{L}^1_{k,m} X'_m - \left(\bar{L}^2_{k,m} X'_m \right)' \right\} = 0 , \tag{4.15}$$

and a total surface contribution

$$\sum_m \left\{ \left(\delta^{vac}_{k,m} + \bar{L}^{1*}_{m,k} \right) X_m + \bar{L}^2_{k,m} X'_m \right\} = 0 , \tag{4.16}$$

with the primes indicating normal derivatives. With $k = 1 \ldots M$ and $m = 1 \ldots M$, these are M equations for M functions X_m, containing an eigenvalue ω^2, and the second equation serves as a boundary condition for the first, combined with the boundary condition of vanishing perturbations at the plasma center, mentioned earlier.

Expressions for the elements of the tensors $P^j_{k,m}$, pertaining to the plasma potential energy δW_p, and $K^j_{k,m}$, to the plasma kinetic energy K are given for $j = 0 \dots 2$ by:

$$\begin{cases} P^0_{k,m} = \dfrac{1}{\mu_0}\dfrac{|\nabla\psi|^2}{\mathcal{J}^2 B^2}\times \\ \qquad \times \left(DU^{0*}_k - \mathcal{J}S - \mu_0\sigma\dfrac{\mathcal{J}B^2}{|\nabla\psi|^2}\right)\left(DU^0_m - \mathcal{J}S - \mu_0\sigma\dfrac{\mathcal{J}B^2}{|\nabla\psi|^2}\right) \\ \qquad - \dfrac{\sigma}{\mathcal{J}}\left(\mathcal{J}S + \mu_0\sigma\dfrac{\mathcal{J}B^2}{|\nabla\psi|^2}\right) + \dfrac{(nq-k)(nq-m)}{\mu_0\mathcal{J}^2|\nabla\psi|^2} - 2p'\kappa_n \\ P^1_{k,m} = \dfrac{1}{\mu_0}\dfrac{|\nabla\psi|^2}{\mathcal{J}^2 B^2}\left(DU^{0*}_k - \mathcal{J}S - \mu_0\sigma\dfrac{\mathcal{J}B^2}{|\nabla\psi|^2}\right)DU^1_m \\ P^2_{k,m} = \dfrac{1}{\mu_0}\dfrac{|\nabla\psi|^2}{\mathcal{J}^2 B^2}DU^1_m DU^{1*}_k\,, \end{cases} \tag{4.17}$$

and

$$\begin{cases} K^0_{k,m} = \dfrac{\rho}{|\nabla\psi|^2} + \dfrac{|\nabla\psi|^2}{B^2}U^{0*}_k U^0_m \rho \\ K^1_{k,m} = \dfrac{|\nabla\psi|^2}{B^2}U^{0*}_k U^1_m \rho \\ K^2_{k,m} = \dfrac{|\nabla\psi|^2}{B^2}U^{1*}_k U^1_m \rho\,, \end{cases} \tag{4.18}$$

where S is the shear, σ is the parallel current and κ_n and κ_g are the normal and geodesic components of the curvature:

$$S = -\frac{1}{\mathcal{J}}\frac{\partial\Theta^\alpha}{\partial\theta}\,, \tag{4.19}$$

$$\sigma = \frac{\epsilon_{ijk}}{\mu_0}\frac{1}{B^2\mathcal{J}}\frac{\partial B_j}{\partial u^i}B_k\,, \tag{4.20}$$

$$\kappa_n = \frac{\nabla\psi}{|\nabla\psi|^2 B^2}\cdot\nabla_\perp\left(\mu_0 p + \frac{B^2}{2}\right)\,, \tag{4.21}$$

$$\kappa_g = -\frac{1}{2p'}\frac{1}{\mathcal{J}}\frac{\partial\sigma}{\partial\theta}\,, \tag{4.22}$$

making use of the covariant components of the magnetic field $B_i = g_{\theta,i}/\mathcal{J}$ and the following definition for Θ^i:

$$\Theta^i = \frac{\nabla\psi\cdot\nabla u^i}{\nabla\psi\cdot\nabla\psi}\,. \tag{4.23}$$

Subsequently, the quantities U_m^i and DU_m^i, for $i = 0, 1$, correspond to the geodesic component of the plasma perturbation $U = \frac{\nabla\psi \times \mathbf{B}}{|\nabla\psi|^2} \cdot \boldsymbol{\xi}$, minimized as a function of the normal component X, and the parallel derivative:

$$U_m = \left[U_m^0 + U_m^1 \frac{d}{d\psi} \right] (X_m) \,, \tag{4.24}$$

$$DU_m^i = \frac{\partial U_m^i}{\partial \theta} + i\,(nq - m)\, U_m^i \,, \tag{4.25}$$

where

$$\begin{cases} U_m^0 = -\left(\Theta^\alpha + q'\theta\right) + \\ \qquad + \frac{i}{n}\frac{1}{B_\theta}\left[B_\alpha q' + \mathcal{J}\mu_0 p' + i\,(nq - m)\left(B_\alpha q'\theta - B_\psi\right)\right] \\ \qquad + \frac{i}{n}\frac{1}{B_\theta}\frac{nq - m}{n}\mathcal{J}\mathbf{B}\cdot\nabla\psi\times\nabla\left(\Theta^\theta e^{i(nq-m)\theta}\right) e^{-i(nq-m)\theta} \,, \\ U_m^1 = \frac{i}{n}\left(1 + \frac{nq - m}{n}\frac{B_\alpha}{B_\theta}\right) \,. \end{cases} \tag{4.26}$$

and the remaining quantities have their usual meaning.

A discussion concerning the physical meaning of the different terms in above equations is given in [Wey+14].

4.3 Numerical aspects of PB3D

In this section, first the discretization of the system of ODEs is discussed, followed by a subsection considering the code structure and a section giving information about the used algorithms.

1 - Discretization

In PB3D, functions $X_m(\psi)$ are discretized using finite differences at I normal positions ψ_i. The M different modes are then bundled at each of these I normal positions into the new vector $\mathbf{X}$ of size $I \times M$ whose components $X_{mi} \equiv X_m(\psi_i)\, e^{-im\theta}$.

Subsequently discretizing the differential operators of eqs. 4.15 and 4.16 then naturally leads to a generalized eigenvalue problem of the form:

$$\mathbf{A}\mathbf{X} = \lambda \mathbf{B}\mathbf{X} \,, \tag{4.27}$$

with $\mathbf{A}$ and $\mathbf{B}$ matrices corresponding to the potential and kinetic energy, $\mathbf{X}$ the eigenvector and $\lambda = \omega^2$ the eigenvalue, so that $\lambda > 0$ denotes stability

and $\lambda < 0$ instability. The discretized boundary condition (eq. 4.16) enters in the last rows and columns of the matrices and the other boundary condition, the vanishing of the discretization at the plasma center, at the first rows and columns.

Importantly, if the discretization is done judiciously, **A** and **B** are Hermitian, reflecting the energy-conserving nature of ideal MHD in a numerical way. Though PB3D can handle this process using central differences of arbitrary order, for the sake of illustration, only the results for the first order are described here, using

$$\begin{aligned} f^{(1)} &= \frac{f_{i+1} - f_{i-1}}{\Delta} - \frac{\Delta^2}{6} f^{(3)} + \mathcal{O}\left(\Delta^4\right) \\ &\approx \frac{f_{i+1} - f_{i-1}}{\Delta} \,, \end{aligned} \tag{4.28}$$

with constant step size $\Delta = \psi_{i+1} - \psi_i$. Defining the discretized Lagrangian as $\mathbf{L} \equiv \mathbf{A} - \lambda \mathbf{B}$, the generalized eigenvalue equation becomes

$$\mathbf{L}\mathbf{X} = 0 \,, \tag{4.29}$$

where now the bar notation is left out as henceforth all the quantities are assumed to be magnetic average modes.

Discretizing the Euler eq. 4.15, the bulk of the matrix **L** is found to be given by the superposition along the diagonal of a Hermitian *stencil* consisting of nine $(M \times M)$ blocks of the form

$$\begin{pmatrix} \left(\frac{1}{2\Delta}\right)^2 \mathbf{L}_i^2 & -\frac{1}{2\Delta}\mathbf{L}_i^{1\dagger} & -\left(\frac{1}{2\Delta}\right)^2 \mathbf{L}_i^2 \\ -\frac{1}{2\Delta}\mathbf{L}_i^1 & \mathbf{L}_i^0 & \frac{1}{2\Delta}\mathbf{L}_i^1 \\ -\left(\frac{1}{2\Delta}\right)^2 \mathbf{L}_i^2 & \frac{1}{2\Delta}\mathbf{L}_i^{1\dagger} & \left(\frac{1}{2\Delta}\right)^2 \mathbf{L}_i^2 \end{pmatrix} . \tag{4.30}$$

The matrix **L** is adapted at the first and last normal position $i = 1$ and $i = I$ to incorporate the boundary conditions. At the first position, the perturbation is set to zero by introducing an artificial eigenvalue λ_{BC} and adapting the first row and column block of the matrices **A** and **B** to

$$\mathbf{A}_{ij} = \begin{cases} \nVdash \lambda_{BC} & \text{if} \quad i = j = 1 \\ 0 & \text{if} \qquad \text{else} \end{cases} \quad \text{and} \quad \mathbf{B}_{ij} = \begin{cases} \nVdash & \text{if} \quad i = j = 1 \\ 0 & \text{if} \qquad \text{else} \end{cases} . \tag{4.31}$$

The stencil at the last position $i = I$ is modified using the boundary condition from eq. 4.16

$$\begin{matrix} 0 & \frac{1}{2\Delta}\delta^{\text{vac}} & 0 \\ \frac{1}{2\Delta}\delta^{\text{vac}} & \mathbf{L}_I^{0,\text{mod}} & 0 \\ 0 & 0 & 0 \end{matrix} , \tag{4.32}$$

with

$$\mathbf{L}_I^{0,\text{mod}} = \mathbf{L}_I^0 - \left(\mathbf{L}_I^1 + \delta^{\text{vac}}\right)\left(\mathbf{L}_I^2\right)^{-1}\left(\mathbf{L}_I^1 + \delta^{\text{vac}}\right)^\dagger . \tag{4.33}$$

Finally, it is interesting to note that the stencil from eq. 4.30, which resulted from the discretization of the Euler equation (eq. 4.15), can also be interpreted directly as the terms in the Lagrangian by considering the quadratic form $\frac{1}{2}\mathbf{X}^\dagger\mathbf{L}\mathbf{X}$ as the discretized version of

$$\mathcal{L} = \delta W - K = \frac{1}{2}\int_V \mathbf{X}^*\left(\overline{\mathbf{P}} - \omega^2\overline{\mathbf{V}}\right)\mathbf{X}\,\mathrm{d}\psi , \tag{4.34}$$

the discretized integral reduced to a summation in the quadratic form. Indeed, the factors of the stencil that builds up $\mathbf{L}$ have a clear connection to the terms of the operators $\mathbf{V}^j$ and $\mathbf{K}^j$ in eq. 4.14, the terms for $j = 0$ ending up in the central elements of the stencil, the terms with $j = 1$ in the main row and column and the terms with $j = 2$ in the diagonal elements. As a consequence, it can be seen that an extension to higher orders central differences is straightforward: The stencil of eq. 4.30 then just grows in size and the factors change. Practically, apart from an easy way to implement general discretization orders, this is of importance as well as it can be seen that explicit storage of (only the nonzero elements of) the matrix will contain a lot of redundant information. It is then better to make use of so-called *matrix-free methods*, where only the operations of the matrix on vectors or matrices are defined in the numerical code.

2 - Code structure

PB3D is written in a modular way, so that it can be run using the output of various equilibrium codes and to make the stability calculation customizable.

The essence of PB3D consists of four major parts called drivers: the *input driver*, the *equilibrium driver*, the *perturbation driver* and the *solution driver*. There is also a standalone program called POST that does the post-processing of PB3D output, with a single driver. The different drivers function completely independently, to allow for easy modularization, with communication between them going exclusively through optimized HDF5

channels using an output data file, for the large data-sets, as well as some minor global variables for book-keeping. Apart from this, PB3D makes use of the technique of *Richardson extrapolation* [Pre07, sec. 16.4] as well as methods of keeping the memory usage below a threshold, on three different levels. Finally, the whole PB3D code is parallelized using MPI to make efficient use of modern computing resources. Figure 4.1 explains this general structure.

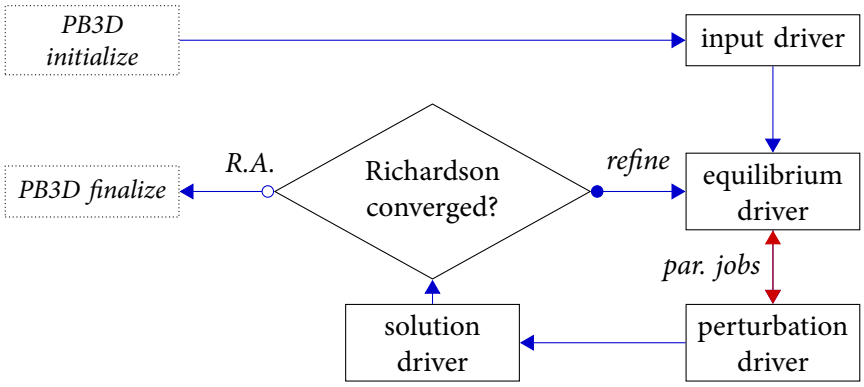

Figure 4.1
PB3D general flowchart. In every Richardson level, it is checked whether the relative error between successive levels falls below a threshold. If not, the parallel grid is *refined*;

(*continued caption*) If so, Richardson extrapolation (*R.A.*) is applied to get an approximation of higher precision. An explanation for the double arrow labeled *par. jobs* is given below, in the paragraph concerning the equilibrium driver. PB3D outputs the relevant variables using HDF5 at completion of each driver, and reads them in the subsequent drivers, but this is not portrayed here.

Note that to find the straight field line coordinates, a similar procedure is done as in [Sán+00], i.e. by finding the zero's of

$$\alpha - \zeta + q\theta = 0 \,, \tag{4.35}$$

but here a variant of Brent's algorithm, called Zhang's algorithm [Zha11], is used.

Subsequently, a word should be said about the ways in which PB3D treats the perturbation mode numbers. One can either choose between prescribing them manually, setting a primary mode number n (fast-varying field line label α; no coupling) and the secondary mode number m (slowly-varying parallel coordinate θ; coupling). However, it is usually more efficient to use the *fast version*, where the user prescribes only the number of secondary modes numbers. PB3D will then automatically calculate the mode numbers that are closest to resonance $nq \approx m$. Not only does this greatly reduce the number of modes, and thus the computing time necessary, but it will also result in matrices $\mathbf{A}$ and $\mathbf{B}$ that are much better conditioned as the whole theory behind PB3D is built on this resonant condition.

Finally, in the next paragraphs, some more information is given about the method of Richardson extrapolation, as well as on so-called *energy reconstruction*.

Richardson Extrapolation Richardson extrapolation is used in PB3D to get better approximations to the numerical integrals of the field lines averages. Use is made of explicit knowledge of the discretization scheme, so that the results for numerical grids with equal boundaries but different numbers of points are combined to reduce the error further. More exactly, for equidistant step size $\Delta\psi$ and discretization through finite differences of order 1, the difference between the true mathematical operator in eq. 4.15 and the discretized version is indicated by the operator

$$\delta\bar{L}[X] = \sum_{l=1}^{\infty} \frac{\Delta\psi^{2l}}{(2l+1)!} \times \\ \times \left[\bar{L}^1 X^{(2l+1)} - \left(\bar{L}^{1\dagger} X\right)^{(2l+1)} - \sum_{j=0}^{\infty} \frac{\Delta\psi^{2j}}{(2j+1)!} \left(\bar{L}^2 X^{(2j+1)}\right)^{(2l+1)} \right] , \tag{4.36}$$

where the superscripts indicate normal derivatives. For general discretization orders p, this can be written as

$$\delta\bar{L} = \sum_{l=1}^{\infty} a_l \Delta\psi^{2pl} . \tag{4.37}$$

Assuming the same kind of dependence on the resulting eigenvalue as well, the information from the solutions of R of different step sizes can be combined, yielding a recursive formula for $\lambda_r^{(R)}$ [DB03, p. 270]

$$\lambda_r^{(R)} = \lambda_{r-1}^{(R)} + \frac{\lambda_{r-1}^{(R)} - \lambda_{r-1}^{(R-1)}}{2^{2pr} - 1} \quad \text{for } r = 1 \dots R , \tag{4.38}$$

with $\lambda_0^{(R)}$ the eigenvalue. This expression is then an approximation of order $\mathcal{O}\left(\Delta\psi^{2p(R+1)-1}\right)$ to the physical eigenvalue.

The fact that the parallel grids used in PB3D are equidistant, with the set of points of a certain Richardson level r equal to the set of points of the previous level $r-1$, *plus* the set of intermediary points, has implications. An important advantage is that for Newton-Cotes formulas of order 1 and 3 (i.e. trapezoidal rule and Simpson's 3/8 rule), not only the *points* but the entire *integrals* calculated for the previous Richardson levels can be used in the

calculation of the integrals of the current level, which cuts memory usage almost by half. For these Newton-Cotes rules, the integral I_r calculated with all the points of a Richardson level $r > 1$ is given by:

$$I_r = \frac{I_{r-1}}{2} + K_r \,, \tag{4.39}$$

where K_r is a combination of only the new points for this Richardson level (i.e. the intermediary points with respect to the points of level $r - 1$), differing slightly from the general Newton-Cotes formulas to account for boundary effects.[4]

As explained in fig. 4.1, after each Richardson level $r > 1$, PB3D checks whether the relative difference between the eigenvalue found in this level and the previous level is lower than a certain threshold. If so, Richardson extrapolation is applied to combine the eigenvalues calculated for all the previous levels $1 \ldots r$ into the approximation with the lowest error. If convergence is not yet reached, the process starts again after refining the parallel grid by adding the intermediate points, as stated above. Again, it should be noted that the calculations for the next Richardson level will then only use these intermediary points, i.e. half the refined grid, which is not a general feature of Richardson extrapolation schemes. Note that, as the eigenvectors are a function of the normal coordinate only, the eigenvectors found for the current Richardson level can be used easily as a first guess for the next one, sometimes drastically cutting computing time.

Finally, the modular structure of PB3D grants the opportunity for restart. A simulation that has been done up to Richardson level r can be (re)started up to level $r + 1$. This allows for added control of the Richardson extrapolation loop.

Energy reconstruction POST is a complementary post-processing program for PB3D output. Among other things, it is worth mentioning that in POST *energy reconstruction* is performed, by which the following is meant: The eigenvector can be used to calculate the individual terms that constitute the plasma potential as well as kinetic energy. Not only does this provide a final and thorough check on consistency[5] through checking whether the

[4] For example, for Simpson's 3/8 rule, the coefficients of quadrature c_i in $\int f(\psi)\,d\psi \approx \frac{3}{8}\Delta\psi \sum_i c_i f_i = I_r$ are given by $1\ 3\ 3\ 2\ 3\ 3\ 2\ \cdots 2\ 3\ 3\ 1$, and have to be modified to $3\ 3\ 2\ 3\ 2\ \cdots 2\ 3\ 3$ for K_r.

[5] Naturally, these terms do end up in the matrices **A** and **B** of the generalized eigenvalue equation (eq. 4.27) through the vectorial and tensorial perturbation variables discussed in the previous paragraphs, but only after algebraic manipulations that do not preserve their individuality.

Rayleigh Quotient Λ from eq. 4.3 is equal to the eigenvalue λ, it also allows for the individual inspection of these terms to ascertain their individual strengths, for example to see whether an instability is current- or pressure-driven.

4.4 Verification

The PB3D is verified by comparing it with other numerical codes, as well as using criteria of physical consistency. In a first subsection, the axisymmetric equilibrium model CBM18 is discussed, which is then used in subsec. 2 to perform verification for axisymmetric configurations. Subsequently, this is extended to a 3-D configuration in subsec. 3.

The codes HELENA [Mik+97] and VMEC [Hir83] yield the equilibrium configuration, where HELENA is axisymmetric and VMEC is 3-D. For stability comparison, MISHKA [Mik+97] is used, which is a general-n code that employs axisymmetric HELENA equilibria, as well as COBRA [Sán+00], which is an infinity-n stability code that makes use of an eikonal formulation and investigates the stability of 3-D VMEC equilibria by solving the Ballooning equation. The numerical tool ELITE [Wil+02], referenced to in the introduction, is not compared with directly, but ELITE has been verified extensively with MISHKA itself.

Note that all stability results concern the most unstable mode and are stated using MISHKA normalization, using the major radius at the magnetic axis and the toroidal magnetic field on axis.

1 - CBM18 Equilibrium Model

The axisymmetric circular tokamak model called CBM18 is used, which is designed to be ballooning unstable[6] through a steep pressure gradient [FJS10]. This model is used in HELENA format as well as ported to the VMEC format. Fig. 4.2a shows pressure p and safety factor q, that are flux quantities, with dependence only on ψ. A poloidal cross-section of this circular tokamak model is shown as well in fig. 4.2b.

2 - Axisymmetric verification

The PB3D results for CBM18 are directly compared to the results given by the numerical code MISHKA. In these simulations, the fast version of PB3D is used with 500 normal grid points, since increasing it beyond that number only marginally changes the results. In the Richardson extrapola-

[6] Careful verification using peeling cases has to wait for a correct implementation of the vacuum term ξ^{vac} subsection 1.

Figure 4.2
Safety factor, pressure profile and cross-section for CBM18.

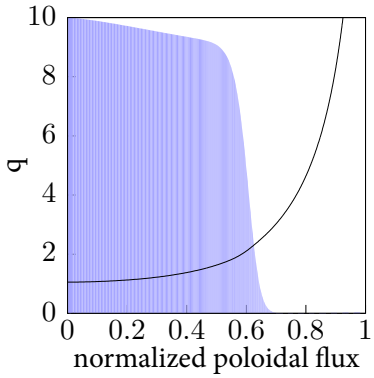

(a) The flux quantities safety factor q (solid line) and the pressure p (shaded, normalized to value at magnetic axis).

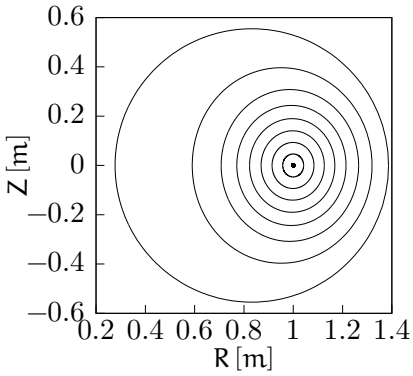

(b) Shifted-circle circular cross-section, showing magnetic axis, plasma edge, and seven equidistant internal flux surfaces.

tion loop, the number of parallel grid points is automatically increased in the fundamental interval $-\pi \ldots \pi$ until a relative error of 10^{-10} is reached. The number of poloidal harmonics, on the other hand, is manually increased until convergence of the most unstable eigenvalue was reached. In this axisymmetric case, the field line label α has no influence. Furthermore, COBRA [Sán+00] is also used to give the limit of $n \to \infty$. The results are plot in fig. 4.3.

Figure 4.3
Comparison between results from PB3D (squares), MISHKA (crosses) and COBRA (dashed line).

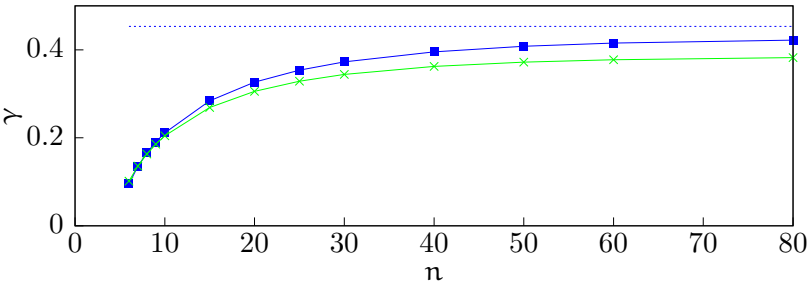

(*continued caption*) At every value for the primary mode number n, the number of secondary modes m is adjusted until convergence is reached, where the fast version of PB3D automatically sets the optimal resonating range.

There is good agreement with simulations done with the numerical codes ELITE and GATO in [FJS10, fig. 6], taking into account a factor 1.5 due to the difference in normalization for the growth rate, due to the usage of $\frac{R}{B} = 1.5\frac{m}{T}$ instead of $1.0\frac{m}{T}$. Furthermore, there is similar behavior of increasing instability for higher n in both cases, i.e. for more localized modes. This is a consequence of the ability of the mode to become better

and better localized in the regions of bad curvature. Also, it can be seen that they have the same marginal point, i.e. the mode number n for which there is marginal stability. However, PB3D gives slightly more unstable results, but this is explained by the fact that the problems solved are basically of different nature between the two codes, due to the high-n approximation employed in the former code as compared to the general-n approach in the latter, which affects the different terms in a different way. In fact, the exact same phenomenon can be observed for ELITE, for example in [Wil+02, fig. 4], with a relative difference similar to the 10% obtained here. Furthermore, COBRA uses the infinite-n assumption, which makes it represent the limiting case, as can be seen from the figure.

Subsequently, fig. 4.4 shows a comparison of the mode structure between PB3D and MISHKA simulations for a CBM18 run with $n = 10$, using 30 Fourier modes with optimally chosen m. In fig. 4.4a, it can be seen that the individual Fourier mode amplitudes $X_m(\psi)$ as well as the global envelope show a Maxwellian structure around the pressure drop, as expected from infinity-n theory [CHT79]. Furthermore, the destabilizing ballooning effect is obtained through the normal displacement of the individual modes with mode numbers m, each resonating on its own rational surface $q \approx \frac{m}{n}$ (not shown). In figs. 4.4b and 4.4c, a visual comparison is displayed between PB3D and MISHKA of the global mode structure of $X(\psi, \theta)$ in a poloidal cross-section.

Finally, the energy reconstruction discussed in the paragraph concerning the post-processing driver, is employed as a check on physical consistency: In fig. 4.5, a comparison is made between the calculated eigenvalue λ and the ratio of potential to kinetic energies in the Rayleigh Quotient Λ through energy reconstruction for different numbers of normal grid points (fig. 4.5a) and in the discretization of the eigenvector (fig. 4.5b). It can be seen that the energy reconstruction improves for increasing number of equilibrium grid points, but that the improvement for increasing the grid points of the discretization of the eigenvector only works up to the same order as the number of grid points in the underlying equilibrium model.

3 - 3-D verification

The VMEC version of CBM18 has been adapted to a 3-D version through varying the poloidal cross-section radius $a(\zeta)$ toroidally by 10% over the whole toroidal range $\zeta = 0 \ldots 2\pi$, meaning that $\frac{\alpha(0)}{\alpha(\pi)} = 1.1$. The pressure profile and safety factor is unchanged and the position of the magnetic axis approximately so. Admittedly artificial, what matters is that this test case is 3-D.

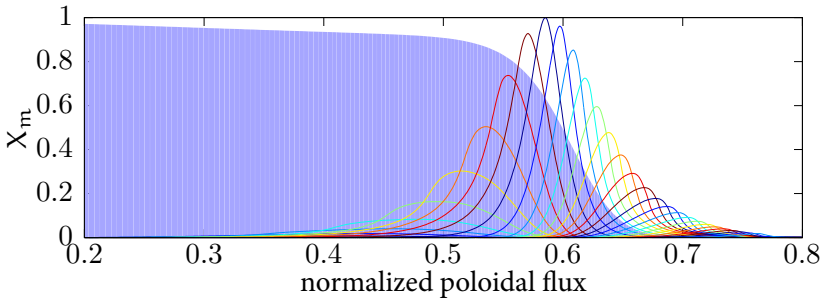

(a) Modes X_m at midplane and pressure p (shaded, normalized to value at magnetic axis)

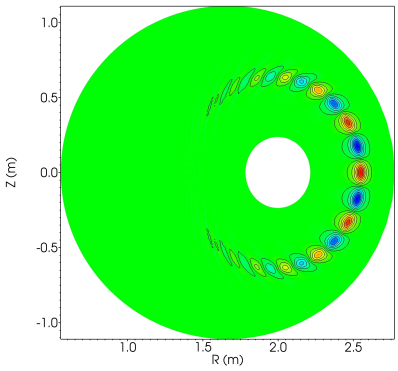

(b) Global mode structure in poloidal cut $\zeta = 0$ for PB3D.

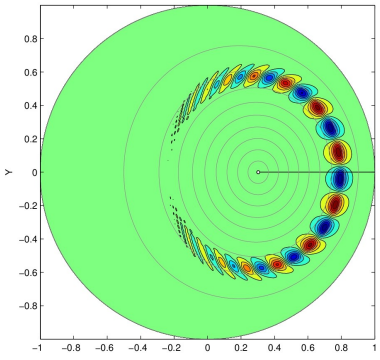

(c) And for MISHKA. (G. Huijsmans)

Figure 4.4
Most unstable mode for a simulation of the stability of CBM18 using $n = 10$ and 30 modes m.

This is reflected in a change of most unstable growth rate,[7] which is seen in fig. 4.6, showing the results from PB3D and COBRA, as well as the results copied from the axisymmetric case, which is referred to as the *large* case.

Also, a *small* case is provided, which corresponds to the axisymmetric configuration with a cross section equal to the smaller end of the modified 3-D case with constant radius equal to $a\,(\pi)$ of the 3-D case. This small case was designed to have the same pressure profile as the large case, and the same safety factor. It is not directly evident why the small case is slightly more unstable in the limit $n \to \infty$ but with the marginal n-value higher than the

[7] It should be mentioned that other types of toroidal modifications, such as by squishing and expanding just the height or major radius, or applying a twist, have been tested and confirmed to generally lead to qualitative similar results. The same counts for toroidal modifications with more periods. The physical investigations of these configurations will be a subject of further work.

Figure 4.5
Energy reconstruction as a function of the number of grid points in the VMEC equilibrium model and in the discretization of the eigenvector.

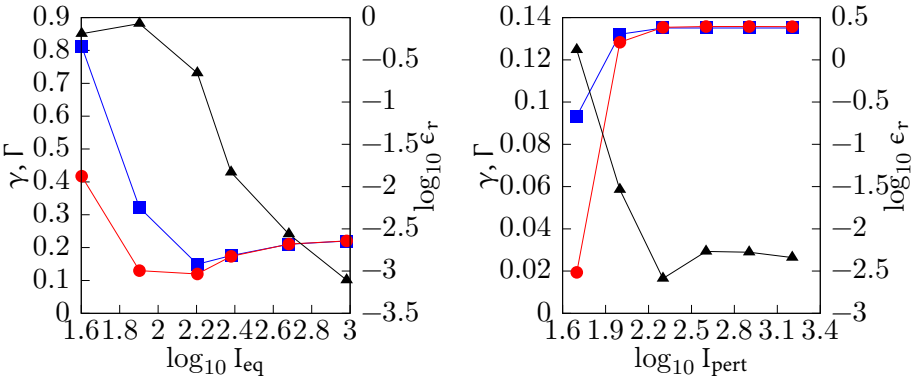

(a) Varying points I_{eq} in VMEC equilibrium.

(b) Varying points I_{pert} in discretization.

(*continued caption*) The number of grid points of either the discretization of the eigenvector or the VMEC equilibrium that is not varied, is kept constant at 500, and the simulations were done using n =10, with 20 modes m. At left axis, squares show $\gamma = \sqrt{-\lambda}$ and circles show reconstructed $\Gamma = \sqrt{-\Lambda}$. At right axis, triangles show the relative difference ϵ_{rel} in logarithmic scale.

Figure 4.6
Comparison between 3-D results from PB3D (triangles) and COBRA (dashed line), as well as the original large (L) axisymmetric results (PB3D with squares and COBRA with dashed line from figure 4.6), and results for the smaller (S) axisymmetric version (PB3D with circles and COBRA with dashed line).

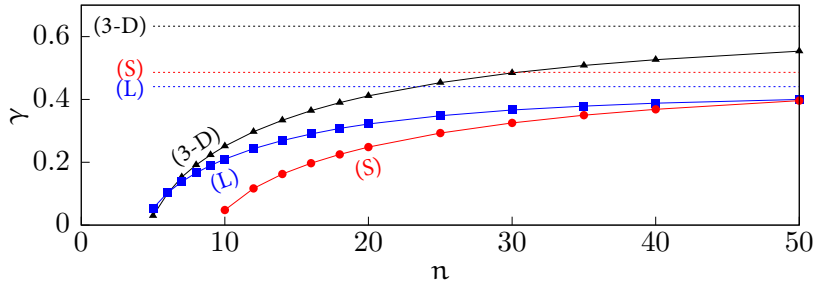

(*continued caption*) Again, the primary mode n is varied and for every value of it, the number of secondary modes m is adjusted until convergence is reached, where the fast version of PB3D automatically sets the most resonating range. The 3-D result is more unstable than either the small or big CBM18 axisymmetric result.

large case, but in figure 4.7 the energy reconstruction is provided. In this figure, the relative contributions of six components of the plasma potential energy are plot, corresponding to the normal and geodesic components of the line-bending energy which is always stabilizing; the ballooning term (proportional to the pressure gradient) and the peeling term (proportional to the parallel current), which can be destabilizing. (See for example [Fre87, eq. 8.87].) It can be seen that the difference between the large and small case is indeed quantitative.

Now, curiously, it can be seen that the PB3D results for the 3-D equilibrium are more unstable than either the small and large cases, an effect also observed in COBRA. To investigate this, the energy reconstruction is also displayed in figure 4.7. The main difference now is the large destabilizing normal component of the ballooning term, and the reduced compensation by stabilizing line bending. And though the geodesic components of both the ballooning and kink term are even slightly stabilizing, perhaps contrary to expectations, due to the toroidal change that has been created by merging the two axisymmetric cases, this is a far smaller effect.

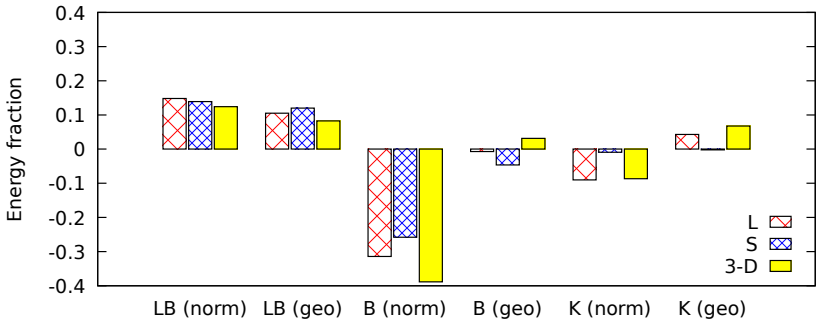

Figure 4.7
Comparison of potential energy terms for $n = 20$. These consist of the stabilizing line bending energy (LB) and the potentially destabilizing ballooning term (B) and kink term (K), displaying the normal components and geodesic components individually.

(*continued caption*) This is done for the large (L) and small (S) axisymmetric cases, and the hybrid 3-D case, described above.

Admittedly, it is an artificial test case, but clearly 3-D results can in some cases deviate strongly from axisymmetric ones PB3D provides the tool to study this.

Finally, contrary to the axisymmetric case, for these 3-D configurations, a discussion regarding the influence of the field-line label α and the limits θ_{max} on the parallel bounding box $-\theta_{max} \leqslant \theta \leqslant \theta_{max}$ is important, which will also provide a check on physical consistency: Namely, α can be understood as the base of the magnetic field lines, i.e. the toroidal position ζ_0 at the midplane $\theta = 0$. As the entire flux surface is covered by the field lines, along which is integrated in the magnetic average modes (eq. 4.13), the parallel integration should range from $-\infty \ldots \infty$. It should therefore be expected that the field line label α have no influence on the final results.

Fig. 4.8a shows how well this is approximated in practice using a parallel bounding box of finite size. It can clearly be seen that the results for small bounding boxes are strongly dependent on α, which reflects that the modes are artificially confined to only use the information of a limited subspace of the 2-D flux surfaces. For larger sizes of bounding boxes—and correspondingly larger number of parallel points—the difference, however, falls

of linearly with the size as can be seen in fig. 4.8b.

Figure 4.8
The influence of the bounding box in the parallel direction θ_{max}.

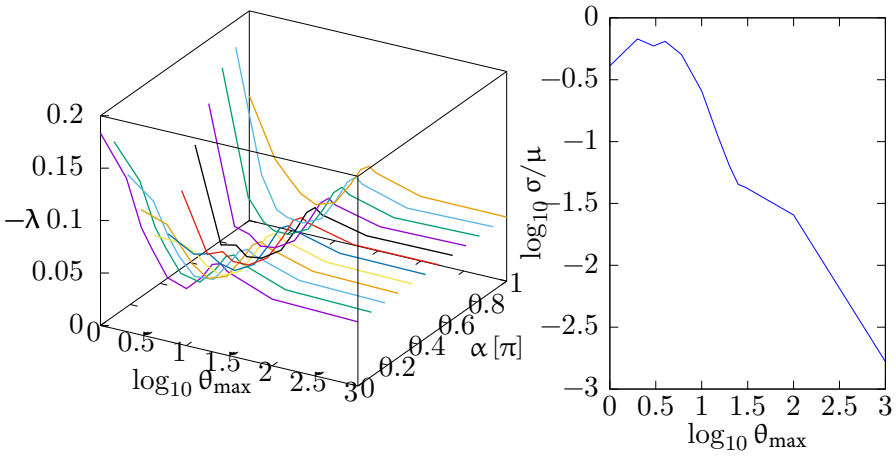

(a) eigenvalues for different field line labels α and different bounding box sizes θ_{max}, showing convergence for large box sizes.

(b) Evolution of the standard deviation σ divided by the average μ, as a function of the box size θ_{max}.

4.5 Summary

The new 3-D linear ideal high-n MHD stability code PB3D is presented, which simulates the high-n ideal linear MHD stability in 3-D magnetic configurations including edge effects. Typical high-n modes that appear are peeling-ballooning modes, which have been linked to, for example, ELM cycling phenomena observed, as well as RMP techniques that break the axisymmetry of plasma for controlling them. It is expected that 3-D configurations offer can offer exciting new insights, such as possible new ranges in parameter space of enhanced stability. Furthermore, it is important that edge effects are taking into account correctly.

This paper focused on verifying the PB3D code using checks on physical consistency as well as by comparing results with MISHKA and COBRA. Good qualitative agreement is found and the quantitative differences are explained through differences in assumptions between these numerical codes. Furthermore, since MISHKA and COBRA have each been extensively benchmarked with other codes (such as ELITE, GATO for MISHKA, or TERPSICHORE for COBRA), this verification exercise has provided further confirmation of the correctness of the approach used in PB3D and its

implementation. A first proof of the capabilities of the code is also presented with some non-intuitive results considering 3-D effects, with the aim of providing a numerical tool that can be used to study them. Further work will focus on the applications of the code and extracting physical results.

Acknowledgments

This research was sponsored in part by DGICYT (Dirección General de Investigaciones Científicas y Tecnológicas) of Spain under Project No. ENE2015-68265

ITER is the Nuclear Facility INB no. 174. The views and opinions expressed herein do not necessarily reflect those of the ITER Organization

Chapter 5

Modification of Stability by Toroidal Field Ripple

Chapter 4 presented the new numerical code PB3D, dedicated to the study of 3-D edge high-n stability through ideal linear MHD. For verification by comparison with other, established numerical codes, a test case was used that is accepted by the community. With PB3D now functional and verified, more realistic applications can be treated.

In this chapter a first real application is treated: The influence on stability by a toroidal field ripple in a realistic tokamak geometry. This is a common example of a situation where the axisymmetric approximation of tokamak geometry is often insufficient, as even though the ripples induced by the discreteness of the toroidal field coils are small, they are found to have a large effect on plasma properties, such as a reduction of the pressure at the top of the pedestal. [Sai+07a; Sai+07b; Ura+06].

The specific investigation of the effects of toroidal ripple on stability is the subject of this chapter. It is done through first considering the influence of pedestal pressure profile steepness of a typical axisymmetric H-mode configuration on its stability. Afterwards, these axisymmetric equilibria are modified by a toroidal ripple of prescribed amplitude and it is observed how this changes the stability boundaries.

Comparisons with the COBRA numerical code [Sán+00] are provided, as well as with experimental results from above references. The $n \to \infty$ results from COBRA are found to be in general agreement with the ones from PB3D, and there is qualitative agreement with the experiments, with the same trends observed.

abstract

The new numerical code **PB3D** (**P**eeling-**B**allooning in **3**-**D**) presented in [Wey+16] is used to investigate the influence of the toroidal field ripple on the stability properties of high-confinement equilibria. From axisymmetric studies it has been shown that often the stability limits of the pressure in the H-mode pedestal in tokamaks are dictated by the peeling-ballooning stability boundaries [Sny+02]. However, from experience it is also known that a toroidal field ripple, resulting from the discreteness of the toroidal field coils, can have a strong destabilizing influence on these equilibria [Sai+07b]. Therefore, the 3-D high-n philosophy of PB3D make it suitable for investigating this topic. It is found here that toroidal ripple effects are indeed important, and that there is qualitative agreement with the same trends observed as in the experimental results from the previous reference. Also, comparisons with $n \to \infty$ results from COBRA [Sán+00] are done. The COBRA results are similar but slightly more unstable.

5.1 Introduction

The influence on stability by a toroidal field ripple is an important problem in tokamaks, which are often described using axisymmetric models. The dominant component of the magnetic field, however, is generated using toroidal field coils, and these are of an inherently discrete nature through which they introduce a toroidal ripple. In fact, it is observed that these ripples can have a strong influence on the stability of the plasma, despite their apparently diminutive sizes: As a rule of thumb, for any well-confining tokamak the modulation of the toroidal magnetic field should be no more than about a percent. For ITER, for example, the toroidal field coils induce a ripple of 1%, which leads to unacceptably large fast particle losses for the Q=5 scenario. Therefore, it was amended to $0.3 - 0.4\%$ using ferritic insets [Sai+07a]. These low values indicates already that 3-D effects are of importance and it is one of the aims of this paper to analyze this in a computational way.

The numerical code PB3D [Wey+16] is employed, which uses ideal linear magnetohydrodynamics (MHD) with the *high*-n assumption, where n

quantifies how much a normal mode is localized along the magnetic field lines of toroidal confinement devices in a fluted shape. For axisymmetric configurations, they have been found important for stability considerations, through so-called *peeling-ballooning* modes. *Edge-Localized Modes* (ELMs), for example, which periodically release energy to the confinement device edges, can be understood in terms of peeling-ballooning instabilities [WM99]. They can be driven by both a pressure gradient and a parallel current, and the perturbation of the plasma edge can be important. In PB3D, therefore, like in the numerical code ELITE [Wil+02], the plasma edge is allowed to be perturbed.

The example of the toroidal field ripple treated here, however, indicates that it is also important to include 3-D effects, and there are many more examples that will not be discussed, such as the stability of stellarators, that are inherently 3-D, and the deliberate breaking of axisymmetry through perturbation coils for ELM control. PB3D is designed specifically for these 3-D effects, as it does not employ any assumptions such as axisymmetry. At the same time, it is also capable of including the influence of the edge perturbation.

In a first section the equilibrium model is described, as well as its 3-D ripple modifications. Afterwards, section 5.3 treats the simulation results of a study where width and height of the pedestal pressure profile were varied for this axisymmetric model, to investigate the influence of the pedestal. Subsequently, the 3-D modified equilibria are used, to see how strong an influence the ripple can have on the stability properties in section 5.4. Discussions of the results are provided within these two sections. Finally, conclusions are stated.

5.2 The Equilibrium Model

The equilibrium model considered as the base for the simulations performed in this work is a representation of a so-called *high-confinement* (H-mode) configuration. These H-mode configurations are characterized by the presence of a steep pressure gradient at the edge of the plasma, the *pedestal*. The pedestal is formed by the stabilization of turbulence inside the separatrix [Ter00]. Its steep gradient is welcome in fusion plasmas as it increases the achievable temperature in the plasma core, ultimately benefiting the fusion yield.

At the same time, however, steep pressure gradients are a source of free energy for plasma instabilities such as the interchange modes and the bal-

looning modes described through MHD, where the former can be thought of as analogous to the Rayleigh-Taylor instability when a heavy fluid is placed on top of a lighter one, and the latter as a localized version of it. Via neoclassical effects, these gradients also drive larger bootstrap currents close to the edge, which can drive kink modes and their more-localized variants called peeling modes, also described through MHD [Wil+02].

1 - Equilibrium description

The equilibria used in this work are modeled after the JET geometry. They are D-shaped, contain a pedestal and are produced by the HELENA equilibrium code [Mik+97]. In this first study, it is chosen to start with a simplified description of the plasma shape using inverse aspect ratio ϵ, ellipticity σ and triangularity τ. The D-shape is then provided through the common expression [GKP10]:

$$\begin{cases} R = R_0 + a\cos\left(\theta + \tau\sin\theta\right), \\ Z = Z_0 + a\sigma\sin\theta, \end{cases} \tag{5.1}$$

where the boundary is chosen slightly to the inside of the separatrix, as the approximation of closed flux surfaces is used in the equilibrium codes as well as PB3D. Here, R and Z are the cylindrical variables, a is the minor radius and R_0 and Z_0 are the position of the geometric axis, that differ from the magnetic axis through the Shafranov shift, but Z_0 is commonly chosen zero. For these JET-like equilibria the inverse aspect ratio $\epsilon \equiv \frac{a}{R_0}$, is chosen to be $\epsilon = 0.32$, the major radius $R_0 = 2.96\text{m}$, the ellipticity $\sigma = 1.7$, the triangularity $\tau = 0.3$, the magnetic field on the magnetic axis $B_m = 2.1\text{T}$, the toroidal current $I_0 = 1.3\text{MA}$ and the poloidal beta $\beta_p = 1$. The effect of the X-point plasma shape, which is known to be necessary for H-mode formation, is not included here for computational simplicity but will be considered in the future.

The pedestal, subsequently, is modeled using a parameter that describes its height as well as a parameter for its width. These parameters are then used in an analytic expression for the pressure gradient in the flux coordinate defined as $s \equiv \sqrt{\left(\psi/\psi_{\text{edge}}\right)}$ where $\psi(s)$ is the poloidal flux between the magnetic axis and a certain flux surface s:

$$\frac{dp}{ds} \propto -2s\left(1 - s^2\right) + \left(\frac{dp}{ds}\right)_{\text{ped}}, \tag{5.2}$$

where the second term represents a pedestal with height characterized by a

factor H_{ped} and situated at $s_a \leqslant s \leqslant s_b$, with in this model $1 \leqslant s_b$:

$$\left(\frac{dp}{ds}\right)_{ped} = \begin{cases} 0 & \text{for } s < s_a \ , \\ -H_{ped}\, 2s \left[3\left(\frac{s-s_a}{s_b-s_a}\right)^2 - 2\left(\frac{s-s_a}{s_b-s_a}\right)^3\right]^{0.03} & \text{else .} \end{cases} \tag{5.3}$$

Viewed in terms of ψ, this function is almost square, rising quickly to its maximum value in the interval $s_a \leqslant s \leqslant 1$ corresponding to the pedestal range. This implies that in this region the pressure gradient is almost constant. A definition of the plasma pedestal pressure gradient as a function of the poloidal flux would therefore be the most rigorous definition.

However, as this is not very intuitive, here the gradient of the pedestal pressure is considered as a function of the plasma radius at the midplane $R(\theta = 0, \psi)$, measured in kPa/cm. As the pedestal is situated close to the plasma edge, the relation between the plasma radius and the poloidal flux is approximately given by

$$R(\theta = 0, \psi) \approx R_0 + as = R_0 + a\sqrt{\frac{\psi}{\psi_{edge}}} \ , \tag{5.4}$$

which leads to an expression for the pressure gradient:

$$\frac{dp}{dR} \approx -\frac{p_0}{a} 2sH_{ped} \ , \tag{5.5}$$

indicating an almost direct proportionality between pressure gradient and the H_{ped} factor, as in the pedestal $s \lesssim 1$. Furthermore, p_0 is a normalization factor for the pressure. It is chosen such that the total toroidal current and poloidal beta are kept constant. As a consequence, the total 3-D integrated pressure is also constant, so that the total thermal energy in the plasma is constant and contributions from the main plasma to the stability limits are avoided. In practice, the values of the pedestal pressure gradients are calculated from the results of the simulations and tabulated below.

Finally, to complete the description of the equilibrium, either the safety factor q can be described, which is defined as the average ratio between the number of times that a magnetic field line travels in the toroidal direction compared to the poloidal direction, or the toroidal current. As stated in the previous paragraph, it is chosen here for the latter, and a formulation similar to equation 5.2 is used, but without the pedestal modification.

2 - Axisymmetric equilibria

In this work, multiple pedestal heights and widths are used. These are summarized in table 5.1. Note again that the pressure profiles are rescaled globally in order to keep the total 3-D integrated pressure constant. Also note that due to the formulation of the pressure profile through its derivative, changing the width $(s_b - s_a)$ while keeping the pedestal height constant, requires adjusting the height parameter slightly. More precisely, the quantity

$$\int_1^{s_a} \frac{dp}{ds}\, ds\,, \tag{5.6}$$

is kept constant and in this case equal to the value corresponding to $H_{ped} = 1.5$, $s_a = 0.95$. In all simulations, $s_b = 1.1$ is used.

Table 5.1
The parameters of the H-mode equilibria chosen in this work: The pedestal height parameters with corresponding pressure, and the pedestal widths with corresponding heights (see main text) and pressure. Also shown are the pressure gradients in the pedestal. The case with height 1.5 corresponds to the case with width 0.95.

pedestal height variation (with $s_a = 0.95$, $s_b = 1.1$)

H_{ped} [ ]	0.3	0.4	0.5	0.6	0.7	0.8	1.0	1.5	2.0	4.0
p [kPa]	11	14	15	17	19	20	23	27	30	37
$\frac{dp}{dR}\left[\frac{kPa}{cm}\right]$	2.3	2.9	3.2	3.6	4.0	4.2	4.8	5.7	6.3	7.7

pedestal widths variation (with $s_b = 1.1$)

$(s_b - s_a)$ [ ]	0.19	0.18	0.17	0.16	0.15	0.14
H_{ped} [ ]	0.77	0.88	1.0	1.2	1.5	1.9
p [kPa]	29	28	28	27	27	26
$\frac{dp}{dR}\left[\frac{kPa}{cm}\right]$	3.4	3.8	4.2	4.8	5.6	6.9

In figures 5.1 and 5.2, the pressure profiles are plotted as a function of the flux label s mentioned above, for the multiple pedestal heights, respectively widths. Note again that the global pressure profiles are rescaled to have the same global integrated pressure, to keep the total thermal energy in the plasma constant; An effect mostly visible for the pedestals with higher top pressures. Also, the accompanying safety factors are plotted, with the same color coding. The safety factors are given only as an indication, and though they are very similar, it can be seen, for example, that the cases with steepest pedestals also have the strongest magnetic shear S, which through its definition as

$$S = \frac{dq}{dr}\frac{r}{q}\,, \tag{5.7}$$

with r a flux function such as ψ or s, is related to the slope of the q-profile in the graph. This is a consequence of the fact that the toroidal current profile is kept constant for the different cases, so that through the force balance in the normal direction (i.e. the direction normal to the magnetic flux surfaces) a stronger (negative) gradient in pressure is compensated by a stronger (positive) shear of the magnetic field lines.

In the field-aligned (ψ, θ, φ) coordinate system, for example, with ψ from above and θ and φ straight-field poloidal and toroidal coordinates and $\mathcal{J}$ the Jacobian, the normal force balance becomes:

$$\frac{dp}{d\psi} = \mathcal{J}\left(j^{\theta}B^{\varphi} - j^{\varphi}B^{\theta}\right) . \tag{5.8}$$

Making use of the expression for the magnetic field in this coordinate system

$$\mathbf{B} = \frac{1}{\mathcal{J}}\left(\boldsymbol{e}_{\theta} + q\boldsymbol{e}_{\varphi}\right) , \tag{5.9}$$

as can be seen from [Wey+14, eq. 6], for example, the force balance reduces to

$$-j^{\varphi} = \frac{dp}{d\psi} + \frac{q}{\mathcal{J}}\frac{\partial}{\partial\psi}\left(\frac{R^2 q}{\mathcal{J}}\right) , \tag{5.10}$$

for the axisymmetric case, indeed relating $\frac{dp}{d\psi}$ to $\frac{dq}{d\psi}$.

Finally, in figure 5.3 a typical cross section is plotted. Note that the lines of constant poloidal angle differ from what would be expected from a geometrical angle and that they are additionally strongly deformed around the pedestal region.

3 - 3-D modified equilibria

The equilibria presented in the previous subsection differ in their pedestal steepness, either through the height or through the width. These equilibria are modified in a 3-D manner by applying a toroidal ripple on the cross-section shape. In this work, this is done in a systematic manner by considering the cylindrical coordinates R and Z that describe the boundary, and modulating them in such a way that the boundary is modified at each point in the direction perpendicular to the surface at that point. By considering the following expression for the contravariant unit vector in the direction corresponding to the ψ coordinate mentioned before:

$$\nabla\psi = \frac{R}{\mathcal{J}}\left(Z_{\theta}\nabla R - R_{\theta}\nabla Z\right) , \tag{5.11}$$

the unit vector in the normal direction can be found as a function of the orthogonal unit vectors in the R and Z direction.

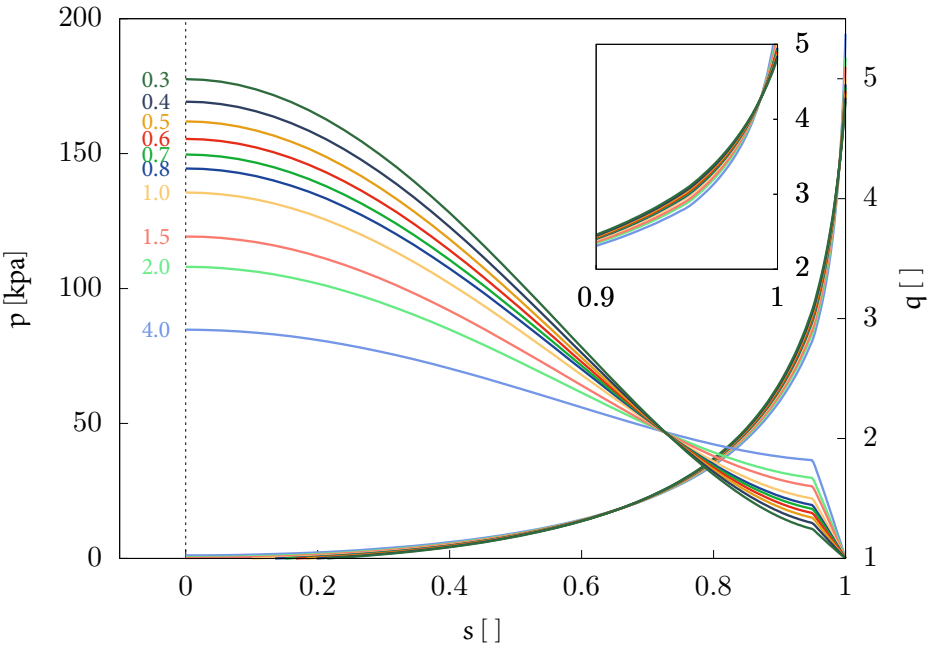

Figure 5.1
(left) Pressure profiles decreasing as a function of the flux label s for different pedestal heights indicated by factors $H_{ped.}$ (right) the corresponding safety factors increasing as a function of s with the same color code and there is an inset at top. The 3-D integral of the pressure is the same for all the cases.

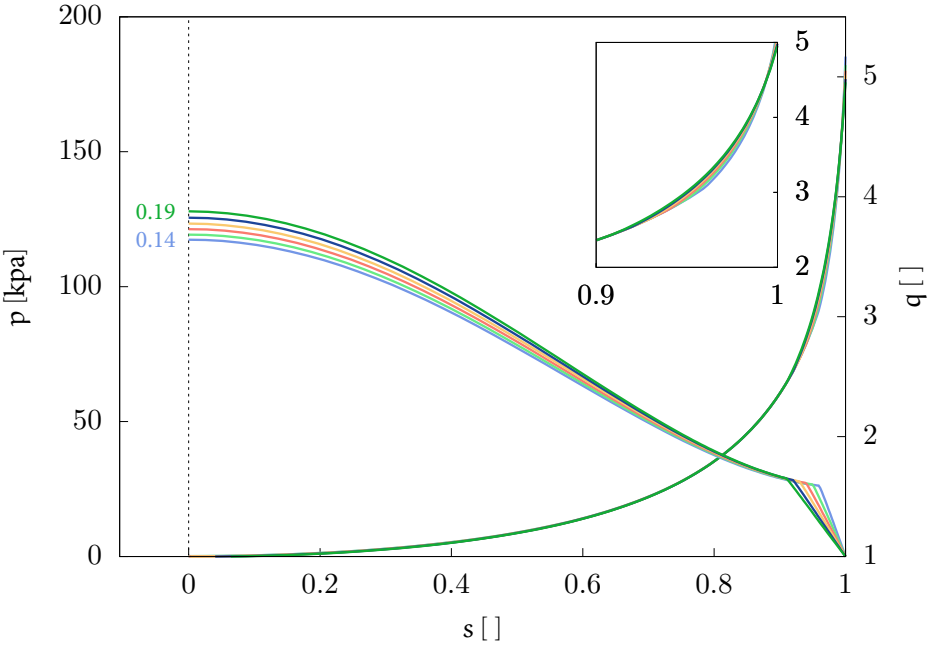

Figure 5.2
(left) Pressure profiles decreasing as a function of the flux label s for different pedestal widths indicated by $(s_b - s_a)$. (right) the corresponding safety factors increasing as a function of s with the same color code and there is an inset on top. Only the labels for 0.14 and 0.19 have been included for clarity. The 3-D integral of the pressure is the same for all the cases.

Superimposed on this, the modulation itself is multiplied by an array of terms with a particular poloidal mode number M and toroidal mode

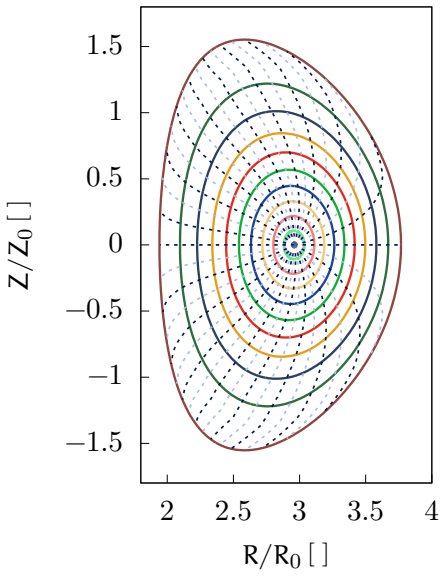

Figure 5.3
Cross section for the axisymmetric H-mode equilibria with pedestal height 1.0. Plot are the projection of 11 equidistantly spaced flux surfaces $s = \text{const.}$ with spacing 0.1 (solid) and 36 equidistantly spaced surfaces of straight-field lines poloidal angle $\theta = \text{const.}$ with spacing 10° (dashed) on the poloidal plane.

number N. The resulting expression for the modification of the unit vector $\hat{\mathbf{r}}$ is then given by:

$$\hat{\mathbf{r}} \quad \rightarrow \quad \hat{\mathbf{r}} + \Delta_R \hat{\mathbf{R}} + \Delta_Z \hat{\mathbf{Z}} \,, \tag{5.12}$$

with the two factors Δ_R and Δ_Z given by:

$$\begin{cases} \Delta_R = \dfrac{Z_\theta}{\sqrt{R_\theta^2 + Z_\theta^2}} \displaystyle\sum_i \left[R_i^c \cos\left(M_i\theta - N_i\varphi\right) + R_i^s \sin\left(M_i\theta - N_i\varphi\right) \right] , \\ \Delta_Z = \dfrac{-R_\theta}{\sqrt{R_\theta^2 + Z_\theta^2}} \displaystyle\sum_i \left[Z_i^c \cos\left(M_i\theta - N_i\varphi\right) + Z_i^s \sin\left(M_i\theta - N_i\varphi\right) \right] , \end{cases} \tag{5.13}$$

where the subscript θ denotes the poloidal derivative, but i is an index. Note that this Fourier description allows for arbitrary shapes of the 3-D modification. For instance, they could be aligned with the plasma safety factor which, on a sidenote, can be used for the study of resonant perturbation for ELM control. In this work, the following choice for the modulation is made, motivated by experimental observations for the JET tokamak [Sai+07a, fig. 2]:

$$\Delta_{R,Z} \propto \left(\frac{1 + \cos\theta}{2} \right)^3 \cos\left(16\varphi\right) , \tag{5.14}$$

which results in Fourier coefficients $\delta_i^c = R_i^c = Z_i^c$ and $\delta_i^s = R_i^s = Z_i^s$ from table 5.2. Note that $\delta_i^s = 0$ implies that stellarator symmetry is preserved,

as defined in [DH98]. For the global proportionality constant multiplying this expression, multiple values are investigated. This is discussed in section 5.4.

Table 5.2
The Fourier coefficients chosen to represent the toroidal field ripple in this work. Note that stellarator symmetry is preserved.

	$i = 1$	$i = 2, 3$	$i = 4, 5$	$i = 6, 7$
δ_i^c	0.3125	0.234375	0.09375	0.015625
δ_i^s	0.0	0.0	0.0	0.0
M_i	0	1,-1	2,-2	3,-3
N_i	16	16	16	16

Practically, the modification of the boundary shape is done in a new PB3D module, that takes the HELENA equilibria that are used to generate the axisymmetric equilibria, calculates the Fourier coefficients of the cylindrical coordinates R and Z that describe the edge, and convolutes them with the appropriate modulation Fourier series in an automated way. After that, the results are transformed to a Fourier series in another coordinate appropriate for exportation to the VMEC equilibrium code [Hir83], that is able to handle 3-D cases. Whereas HELENA and PB3D use field-aligned angular coordinates, the philosophy of VMEC is based on the optimal deformation of the poloidal angle in order to minize the Fourier base. As an input, however, it requires the Fourier modes of the edge in the geometrical poloidal and toroidal coordinates.

In figure 5.4, an exaggerated modulation of the cross-section is shown through the extremal values and through varying the toroidal angle over a fundamental half-period $0 < \theta < 10°$ of the ripple and plotting the projection of 36 equidistantly spaced points on the plasma edge in the field-aligned poloidal coordinate, though not all are visible. Shown also for comparison is the projection of the edge surface from figure 5.3. Furthermore, in figure 5.5 associated 3-D rendering of the modified equilibrium is presented. Note that the ripple is indeed situated at the outboard of the configuration, around $\theta = 0$.

5.3 The Pedestal

As stated in the introduction, the pedestal is the steep part of the pressure profile close to the plasma edge. It is a welcome consequence of the turbulence suppression inside the separatrix obtained in H-mode, but it is

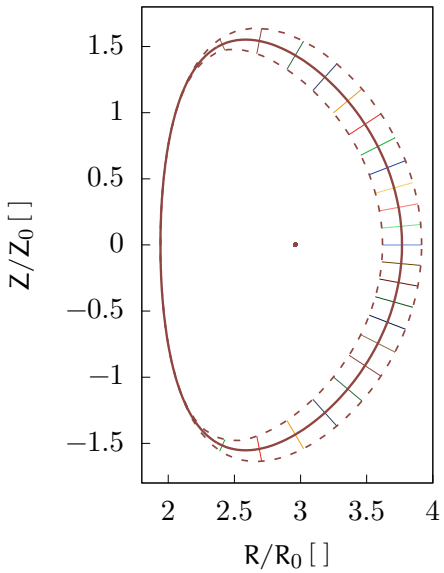

Figure 5.4
Extremal cross sections (dashed) for the 3-D modified H-mode equilibria with pedestal height 1.0, exaggerated between ten- and a hundred-fold, compared to the axisymmetric case (solid). Shown also are 36 equidistantly spaced points with spacing 10° on the edge in the field-aligned poloidal angle, though some cannot be distinguished.

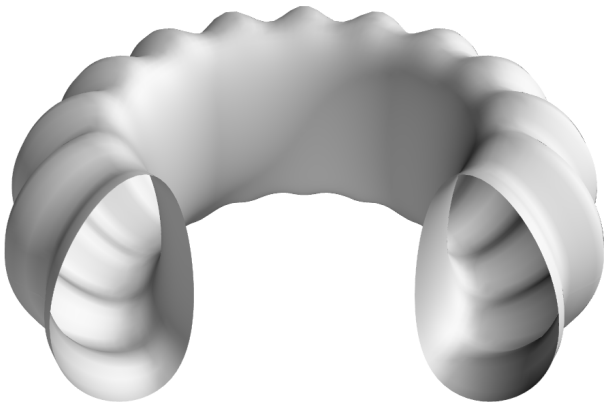

Figure 5.5
3-D rendering of the edge surface of an equilibrium configuration perturbed by a toroidal ripple, exaggerated between ten- and a hundred-fold, with a quarter of the toroidal range cut.

also a source of free energy for ballooning modes. It is of interest, therefore, to vary the pedestal parameters in an equilibrium configuration and investigate the influence this has on the high-n stability.

Both the pedestal height and width were varied independently, and the growth rate of the resulting instabilities were computed as a function of the principal mode number n, which appears in the formulation for the plasma perturbation ξ used by PB3D:

$$\xi(\alpha, \psi, \theta) = \sum_{m} \hat{\xi}_m(\psi)\, e^{i[n\alpha + (nq - m)\theta]}, \tag{5.15}$$

where the (α, ψ, θ) coordinate system is used: ψ is the normal coordinate

defined above, θ is the coordinate parallel to the magnetic field lines and $\alpha \equiv \varphi - q\theta$ is the geodesic coordinate, which indicates on which field line in a flux surface one is situated. The flutedness condition translates to $n \gg 1$ and $nq - m \sim \mathcal{O}(1)$ through which it can be argued that, to lowest order, the modes can be decoupled in the geodesic direction α, which means in practice that the simulations for different values of n can be done independently [Wey+14, fig. 1]. This is also the reason why n does not appear as a subscript in equation 5.15.

As there certainly is coupling in the parallel direction θ, multiple secondary mode numbers m have to be taken into account, however, and in PB3D this is done by considering a fixed number M of them, and at every flux surface the range $\overline{m} - \frac{M}{2} < m < \overline{m} + \frac{M}{2}$ is taken, with $\overline{m} = qn$. In all the results presented here, convergence was achieved in the parameter M by choosing it high enough, by which it is meant that the resulting growth rate did not change by more than 10^{-3} for further increases in M. For the other factors, such as number of points in the normal and parallel grids, the same was done.

The results for the axisymmetric simulations are summarized in figure 5.6, which shows the normalized growth rate as a function of the principal mode number n, for the different pedestal height factors H_{ped}, and in figure 5.7, for different pedestal widths. Note that the equilibria with pedestal heights lower than 0.8 and pedestal widths wider than 0.18 are stable.

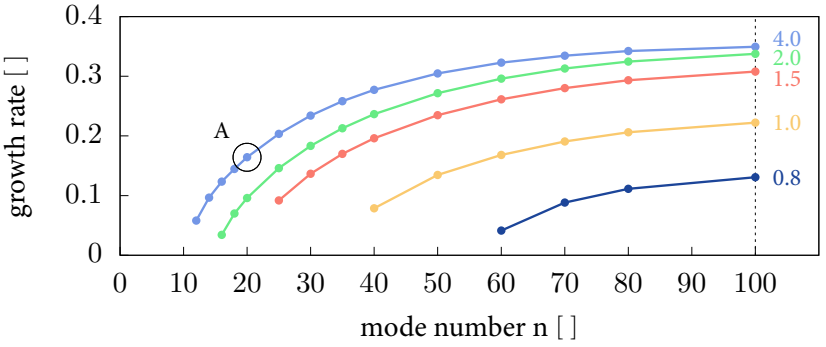

Figure 5.6
Growth rate for the axisymmetric H-mode equilibria with different pedestal heights, normalized to Alfvén time on the magnetic axis.

This puts the critical pressure gradient at the pedestal for the axisymmetric case at a value of about $\frac{dp}{ds} \approx 3.5 \frac{kPa}{cm}$, as can be seen in figure 5.8, that serves as a summary for the axisymmetric simulations where height or width of pedestal were varied. It shows the most unstable growth rate as a function of the pedestal pressure gradient, as well as the marginally unstable primary mode number n (i.e. the lowest n that is unstable). There is a good match between the marginally unstable primary mode number, as well as the growth rate, for both types of simulations, which reflects the

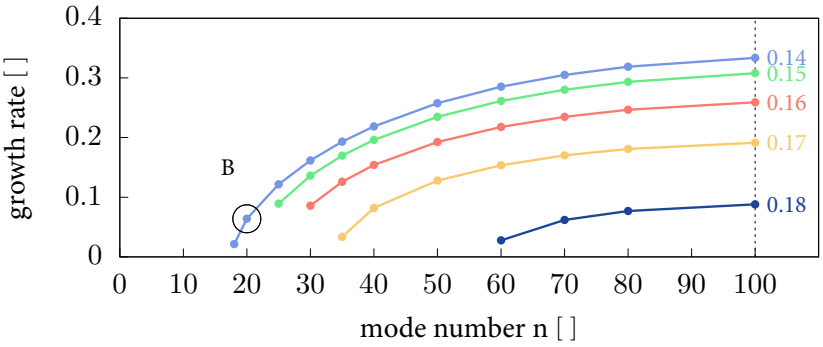

Figure 5.7
Growth rate for the axisymmetric H-mode equilibria with different pedestal widths, normalized to Alfvén time on the magnetic axis.

fact that it is really the pressure gradient that drives these instabilities.

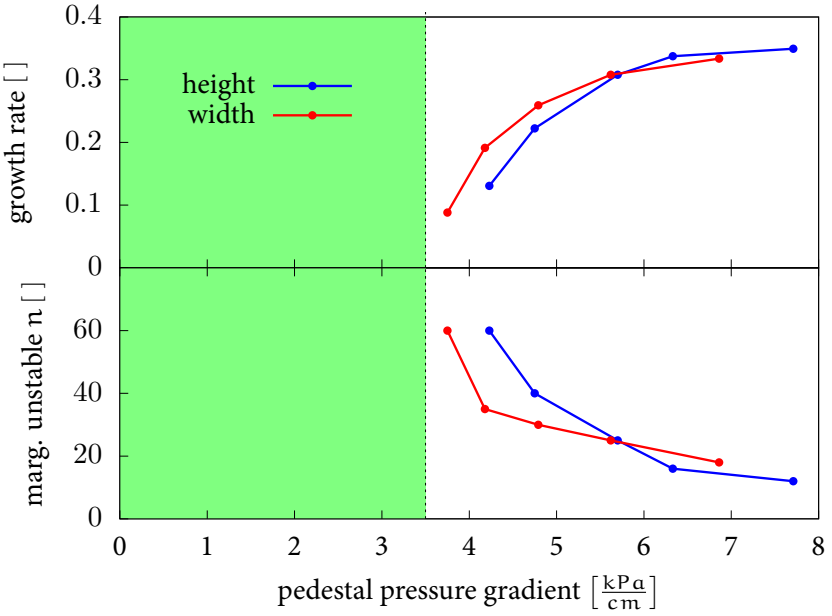

Figure 5.8
(top) Growth rate for the axisymmetric H-mode equilibria versus pedestal pressure gradient, normalized to Alfvén time on the magnetic axis. (bottom) The marginal primary mode number n. The blue lines correspond to the variation of pedestal height, red to width. The green area is stable.

Instructive is therefore figure 5.9 that shows the mode structure of the normal component of the perturbation at the midplane $\theta = 0$, as well as the normalized pressure profile. The two cases shown also indicated to by circles in figures 5.6 and 5.7: (A) $H_{ped} = 4.0$, $(s_b - s_a) = 0.15$ and (B) $H_{ped} = 2.5$, $(s_b - s_a) = 0.14$, both with primary mode number $n = 20$. Note how these unstable modes are localized around the region where the pressure gradient is highest and how they deviate noticeably from a Gaussian shape around the top of the pedestal. These structures are typical of ballooning modes, where furthermore each individual Fourier mode resonates around its resonant surface where $q \approx \frac{m}{n}$. This can also be verified in figure 5.10,

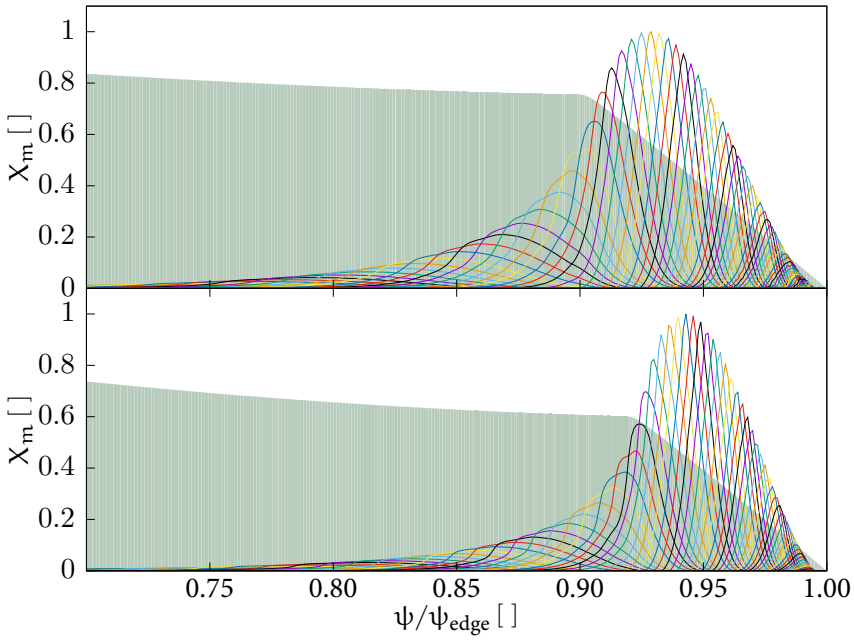

Figure 5.9
Mode structure of normal component of perturbation at the midplane $\theta = 0$ for cases A with $H_{ped} = 4.0$, $(s_b - s_a) = 0.15$ (top) and B with $H_{ped} = 2.5$, $(s_b - s_a) = 0.14$ (bottom). The different colors serve to tell apart the different Fourier modes. Also shown are the normalized pressure profiles.

which shows the fraction of energy carried by the different terms in the plasma potential energy. The normal ballooning term dominates.

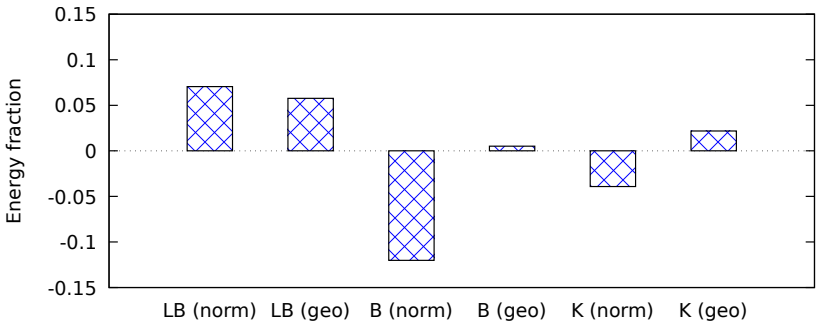

Figure 5.10
Comparison of potential energy terms for $n = 20$. These consist of the stabilizing line bending energy (LB) and the potentially destabilizing ballooning term (B) and kink term (K), displaying the normal components and geodesic components individually.

(*continued caption*) These are the components in the directions normal to the flux surfaces, respectively on the magnetic flux surfaces, but normal to the magnetic field.

5.4 Influence of Ripple on Stability

Here it is investigated how much the stability boundaries change when a toroidal ripple is applied. What this means is that it is looked at how strong a ripple is necessary to drive the previously stable cases with pedestal height factors shown in table 5.1, unstable, i.e. how much the green zone in figure 5.8 shrinks as a function of ripple amplitude. This will illustrate the destabilizing influence these ripples can have.

Here only the simulation results for a single representative high primary mode number n are shown, as it is assumed that the instabilities are of the ballooning type as in the previous section, which are most unstable for mode numbers approaching the infinite limit. Later, this will be verified by plotting the mode structure in figure 5.11. In practice, $n = 50$ is chosen as it is high enough to be not fundamentally different from the infinite limit, while it is still low enough so that the resolution in the normal direction does not need to be unrealistically high and simulation times are not longer than they need to be.

As the simulations done here are 3-D in nature, there is an additional factor that has to be taken into account: the range along the parallel variable θ. Whereas for the axisymmetric simulations of the previous section, the entire field lines can be covered by ranging over a fundamental period $0 \ldots 2\pi$, for 3-D cases in theory this only happens by ranging over $-\infty \ldots \infty$. In practice, it was tested numerically that choosing it from $-10\pi \ldots 10\pi$ was sufficient.

Presented in table 5.3 are the normalized growth rates for the different pedestal heights and ripple amplitudes δr. For comparison, also shown whether the results of the $n \to \infty$ ballooning code COBRA [Sán+00] are stable or unstable, which gives an upper limit to instability. From this table, it is directly clear that the presence of a ripple indeed lowers the stability boundary, so that equilibria with pedestal heights that were previously stable can be driven unstable. Also, the $n \to \infty$ limit provided by COBRA are comparable to the PB3D results, but often give some overestimation of the instability of the configurations, indicating that intermediate primary mode numbers n, taken into account in the PB3D code, are important. And in any case, kinetic effects are also expected to kick in long before n can become so large. Many of them, such as the Finite Larmor Radius effect, are stabilizing.

Furthermore, in figure 5.11 it can be seen that the resulting unstable modes are still driven by pressure gradients, with indeed a ballooning mode

Table 5.3
Growth rates (in black, above) for the 3-D ripple modified H-mode equilibria for different pedestal heights and ripple amplitudes δr, compared to the results from COBRA (in red, below), normalized to Alfvén time on the magnetic axis.

Growth rate (normalized to Alfvén time on magnetic axis)											
δr [cm]	0.0	0.3	0.6	0.9	1.2	1.5	1.8	2.1	2.4	2.7	3.0
$2.9\frac{\text{kPa}}{\text{cm}}$	$\oplus$	$\oplus$	$\oplus$	$\oplus$	$\oplus$	$\oplus$	$\oplus$	$\oplus$	$\oplus$	$\oplus$	$\oplus$
$3.2\frac{\text{kPa}}{\text{cm}}$	$\oplus$	$\oplus$	$\oplus$	$\oplus$	$\oplus$	$\oplus$	$\oplus$	$\odot$	$\odot$	0.18	0.27
								0.09	0.14	0.18	0.22
$3.6\frac{\text{kPa}}{\text{cm}}$	$\odot$	$\odot$	$\odot$	$\odot$	$\odot$	$\odot$	0.09	0.13	0.17	0.21	0.35
	0.06	0.03	0.06	0.09	0.12	0.15	0.18	0.21	0.24	0.27	0.30
$4.0\frac{\text{kPa}}{\text{cm}}$	$\odot$	0.12	0.13	0.14	0.15	0.17	0.19	0.21	0.24	0.27	0.40
	0.18	0.17	0.18	0.19	0.21	0.23	0.25	0.28	0.30	0.32	0.35

(*continued caption*) The $\oplus$ symbols denote configurations stable in both the PB3D and COBRA results, whereas the configurations indicated by $\odot$ are stable in the PB3D simulations, but not in the COBRA $n \to \infty$ limit. Growth rates of the order or smaller than about 0.05 should not be given too much importance.

structure at the midplane $\theta = 0$, where the case is plot for a large ripple of amplitude 3cm, pedestal height factor $H_{\text{ped}} = 0.7$ with pressure gradient $4\frac{\text{kPa}}{\text{cm}}$, and primary mode number $n = 50$. This is the configuration that would be driven unstable first by an increasing ripple. Note from the figure, however, that the toroidal ripple also modifies the mode structure quite drastically when comparing it to the standard ballooning picture such as shown in figure 5.9 for a lower primary mode number n, where the most destabilizing perturbation is situated around the entire pedestal region. Curiously, but not entirely unexpected, the localization is now much stronger around the region most affected by displacement through the toroidal ripple. In fact, the region where the destabilizing perturbation really becomes peaked, lies entirely inside the last 3cm of the plasma closest to the edge.

It is interesting also to compare these computational results with the experimental results from [Sai+07b] for JET and [Ura+06] for JT-60U. The JET tokamak is unique in that its toroidal field ripple can be modified through changing the currents in the generating coils. In the experiments referred to in the paper, the ripple intensity was varied from the standard (very low) 0.08% up to 1%. Among other things, it was found that a major effect an increasing ripple has is to decrease the density in the pedestal. Furthermore, the electron temperature remained largely constant and the ion temperature was raised somewhat, but not enough to offset the decrease

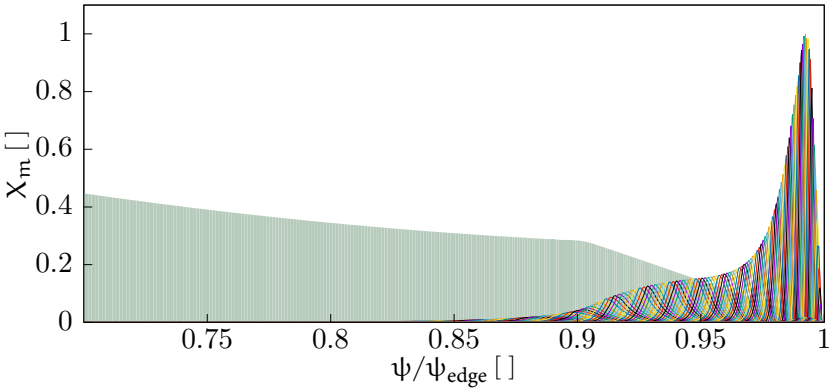

Figure 5.11
Mode structure of normal component of perturbation at the midplane $\theta = 0$ with primary mode number $n = 50$ for a case perturbed by a toroidal ripple of amplitude 3cm with $H_{ped} = 0.7$, $(s_b - s_a) = 0.15$.

(*continued caption*) The different colors serve to tell apart the different Fourier modes. Also shown are the normalized pressure profiles. By comparing this with figure 5.9, the influence of the ripple can be noted.

in density. In the one-fluid MHD model, this then results in a marked decrease of pressure. It was also found that the loss of thermal energy in the plasma at ripple intensity of 1% was about 20% compared to the low ripple intensity of 0.08% and the pedestal height was reduced to half its original size.

In the second reference, similar experiments were done, on the JT-60U tokamak. The ripple intensity was varied by varying the plasma minor and major radii, from 0.4% to 2%. Also there, a decrease of pedestal pressure was found as a function of the ripple intensity. To be more precise, the conclusion could be drawn that the pedestal pressure attainable was also decreased by a factor 2 [Ura+06, fig. 4].

To compare these results directly with the computational results obtained here is not trivial. The configurations simulated here, for example, do not contain an X-point geometry, the presence of which is known to have a stabilizing effect. Also, though keeping the poloidal beta and toroidal current constant for the different pedestal top pressures is useful for the study performed in this work as it avoids contributions from the main plasma to the edge stability, it is a poor model for what really happens in a real tokamak. Closer to the experimental situation would probably be keeping the ratio between plasma energy and pedestal energy constant. Subsequently, in order to generate equilibria, the pressure profiles were described through equation 5.2, as well as the safety factors, using values of the same order of magnitude as the experimental situations (pedestal widths of a few cm and top pressures around 10 to 20kPa). For a realistic comparison with experimental results, this would need to be improved with more detailed

knowledge of experimental profiles. And finally, there is the issue of comparing toroidal field ripples with deformation of the plasma boundary. The ITER definition used in [Sai+07b], for example, is given by

$$\delta_{BT} \equiv \frac{\max B_{tor} - \min B_{tor}}{\max B_{tor} + \min B_{tor}} , \tag{5.16}$$

and how exactly this translates to a modification in the plasma shape is an active topic of research. See for example [Tur12; Tur+13].

However, though it is clearly difficult to provide a realistic comparison between experimental results and simulation results, and though this is not the topic of this work, it can certainly be checked whether the general trends between the two are at least consistent, which is what is done in the remainder of this section. The important assumption is therefore made that the ripple in toroidal field strength is directly and linearly related to the ripple in the plasma minor radius, which is the parameter used here.

Before going on, to justify this assumption somewhat, observe that in linear perturbative MHD the perturbation to the magnetic field due to a plasma perturbation $\boldsymbol{\xi} = X\frac{\nabla\psi}{|\nabla\psi|^2}$ that is purely normal to the flux surfaces, is given by

$$\mathbf{Q} = \nabla \times \left(X\frac{\nabla\psi}{|\nabla\psi|^2} \times \mathbf{B} \right) , \tag{5.17}$$

which in the (ψ, θ, φ) coordinate system can be rewritten to

$$\begin{aligned} \mathcal{J}\mathbf{Q} = &\left(\frac{\partial X}{\partial \theta} + q\frac{\partial X}{\partial \varphi} \right) \boldsymbol{e}_\psi + \left(q\Theta^\theta \frac{\partial X}{\partial \varphi} - \frac{\partial X}{\partial \psi} \right) \boldsymbol{e}_\theta - \\ &- \left(\frac{\partial}{\partial \psi}(qX) + q\frac{\partial}{\partial \theta}\left(X\Theta^\theta\right) \right) \boldsymbol{e}_\varphi , \end{aligned} \tag{5.18}$$

with Θ^θ defined as $\frac{\nabla\theta\cdot\nabla\psi}{|\nabla\psi|^2}$, serving as a measure of the non-orthogonality of the coordinates.

Now, in the case of the H-mode equilibria studied here, the safety factor grows very fast in the pedestal near the plasma edge, much faster than the other variations. Therefore, the dominant term in the toroidal component of above equation becomes

$$\mathcal{J}Q^\varphi \approx -q'X , \tag{5.19}$$

which can be rewritten for axisymmetric (before the perturbation) equilibria making use of the well-known expression for the safety factor

$$q = \frac{\mathcal{J}B_{tor}}{R} , \tag{5.20}$$

to

$$\frac{\delta B_{tor}}{B_{tor}} \approx -\frac{1}{q}\frac{dq}{d\psi}\,|\nabla\psi|\,\delta r\,, \tag{5.21}$$

where $\delta B_{tor} = \frac{Q^{\varphi}}{R}$ is the absolute toroidal field change and δr the absolute normal plasma displacement. Note how the shear defined in equation 5.7 appears naturally, which is quite logical, as the shear just expresses how much the average direction of the magnetic fields changes towards the next flux surface, so when the surfaces are deformed, they experience this rotation of their average direction. In fact, for a circular plasma, the proportionality constant becomes *exactly* the (negative inverse of the) shear. The deviation in general axisymmetric configurations is mostly due to effects of non-circularity.

The proportionality factor between $\frac{\delta B_{tor}}{B_{tor}}$ and δr is plotted in figure 5.12 for 10 equidistant values in the range $s = 0.9 \ldots 1.0$, for the case $H_{ped} = 1.5$ and $(s_b - s_a) = 0.15$. Also shown shaded and rescaled is the factor $\left(\frac{1+\cos\theta}{2}\right)^3$ used in the poloidal modulation of the displacement, from equation 5.14. Note the jump in difference between the profiles corresponding to positions in ($s < 0.95$) and out ($0.95 < s < 1$)the pedestal region. Furthermore, from this figure, it can be argued that the approximation made through using the poloidal modulation of the displacement is a justifiable approximation for the accuracy aimed at in this work, and that the ripple amplitudes up to 3cm are roughly equivalent to a ripple in the toroidal magnetic field up to 2%, the same order of magnitude as the ripples treated in the experiments.

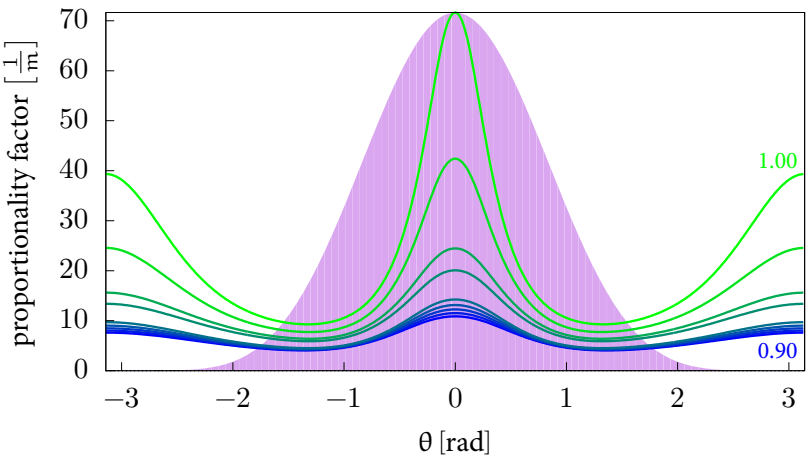

Figure 5.12 Proportionality factor between toroidal field ripple $\frac{\delta B_{tor}}{B_{tor}}$ and normal plasma displacement δr, with the factor -1 left out. Also shown is the modulation of the plasma displacement from equation 5.14.

However, to back this up a little bit more, some simulations were done

with ripple-modified profiles which had the shape prescribed by equation 5.21, with a deviation within 10^{-8}. The results were not qualitatively different.

Assuming now a direct correspondence between the displacement of the plasma boundary and the toroidal magnetic field ripple, the results from [Sai+07b] can finally be seen to be consistent with the results from this work. Indeed, especially figure 7 from that reference is interesting, which shows a reduction of the pedestal pressure as a function of the toroidal field ripple. The difference between the case with minimal toroidal field ripple and the case with a 1% ripple was about 30% to 50%. Interpreting this decrease of pedestal top pressure as the destabilization of peeling-ballooning modes for pedestal top pressures larger than half the original value, consider figure 5.13 that shows for the configuration that is marginally stable for each ripple how much the pedestal top pressure is, which is an equivalent. The situation that

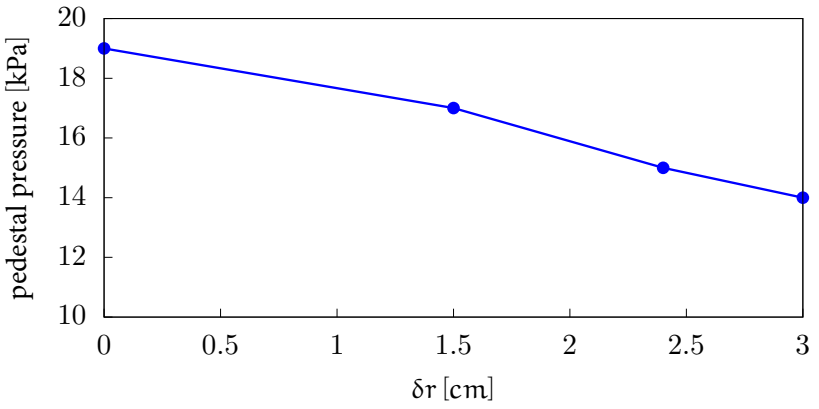

Figure 5.13
Maximum stable pedestal top pressure for various ripple amplitudes. The pedestal width is about 5cm. Can be compared to the scatter plot of [Sai+07b, fig. 7] keeping in mind the reservations described in the text.

was marginally stable before applying a ripple had a pedestal top pressure of 19kPa and a pressure gradient of about $4.0\frac{\text{kPa}}{\text{cm}}$ ($H_{\text{ped}} = 0.7$ in table 5.1), whereas for a ripple $\delta r = 3\text{cm}$, the first configuration that is stable has a pedestal top pressure 14kPa and pressure gradient $2.9\frac{\text{kPa}}{\text{cm}}$ ($H_{\text{ped}} = 0.4$). This is a reduction of about 30%, comparable to experimental results to within a factor of maybe 2, if the conversion between plasma displacement and toroidal magnetic field ripple is taken to be $70\frac{\%}{\text{m}}$, from figure 5.12. Also, as stated above, this was the conclusion drawn from figure 2 in [Ura+06], as well.

5.5 Conclusions

In this work the focus was on the interplay between pedestal top pressure and stability and the modification of this stability by applying a toroidal ripple. This is of interest as toroidal ripples are unavoidable due to construction limitations for tokamak toroidal field coils.

By using the new high-n stability code PB3D, which is capable of treating fully 3-D situations while taking into account the effects of a possibly perturbed plasma surface, first the influence of the pedestal pressure gradient steepness was investigated for configurations that represented an axisymmetric H-mode equilibrium. This was done by considering equilibrium configurations with varying pedestal height and constant width, and others with varying width and constant height. The results from these simulations indicated that the pedestal pressure gradient is indeed the driving factor behind the instabilities that can occur and that these instabilities are of the ballooning type, in accordance with the standard picture.

Next, the influence of a toroidal ripple was shown by calculating the stability of H-mode configurations with different pedestal heights that had been modified by a 3-D toroidal ripple of a somewhat realistic shape and with different ripple amplitudes. It was seen that, indeed, even small ripples (i.e. of a few centimeters in JET dimensions) are of importance, and that employing an axisymmetric approximation is not really justified, however often done. Furthermore, qualitative agreement with experimental results from both the JET and JT-60U tokamak was found, where the varying level of degradation of the maximum attainable pedestal pressure gradient by a varying intensity of toroidal field ripple was also observed.

This confirms the view that peeling-ballooning stability considerations are indeed of importance in the determination of pedestal height and gradient, implying that these are limited by the high-n MHD stability.

Chapter 6

Evaluation and Discussion

Assess the importance / the effect of 3-D effects on MHD stability in magnetic fusion devices.

Repeated above is the main research goal of this work. First of all it drove the development of a theoretical framework specifically suited towards the description of high-n modes in general 3-D configurations, while correctly taking into account the influence of perturbing the plasma edge. Once this was completed, a numerical code, named PB3D (Peeling-Ballooning in 3-D) was designed and written, for the purpose of solving the system of equations provided by the theory. PB3D, then, enabled the study of exactly these 3-D effects and after verification of the PB3D results for standard test-cases with other, established numerical codes, a first realistic case was investigated where 3-D effects play an important role: The study of the influence of a toroidal ripple on the confinement properties of an H-mode plasma.

In this chapter the research questions that related to these activities are shortly discussed and an evaluation is given. Afterwards, some words follow as suggestions for further work.

6.1 Theoretical Framework

Question 1 *How can the ideal high-n MHD stability be theoretically described for fully 3-D equilibria while allowing for edge effects?*

Previously, work had already been done for the full 3-D treatment of high-n modes, as well as work on a high-n stability treatment for axisymmetric equilibria with possible edge perturbations. However, the combina-

tion of a full 3-D approach with a treatment of an edge perturbation in a dedicated manner for high-n modes, did not yet exist, and this motivated the research in this doctoral work. The creation of a dedicated, fully 3-D edge ideal linear high-n stability theory was a novel contribution of this work.

The energy principle was used, which combines the established theory of ideal linear MHD, where perturbations of equilibrium situations are considered, with normal mode analysis where the complex frequency of each mode describes whether it is stable or unstable. On this basis a theoretical framework was built, applying scale analysis in this parameter n. This allowed for a reduction of the complexity of the problem, through the removal of one of the three dimensions. As a result, the stability of the normal modes considered was described through a system of coupled 1-D ordinary differential equations in the dimension corresponding to the direction normal to the flux surfaces, containing eigenvalues corresponding to the square of their complex frequencies.

One consequence of removing the dimension corresponding to the direction perpendicular to the magnetic field lines but lying in the flux surfaces, was that the resulting problem is inherently of the same complexity of the 2-D (axisymmetric) problem, as the problems considered before. However, where in the 2-D case the interpretation used was that only a toroidal cross-section needs to be considered, through the 3-D case treated here, it was shown that a more general interpretation is that the stability for different field lines can be decoupled, and that their stability results from integrating certain quantities along them.

The other major ingredient of the theoretical framework was the correct inclusion of the effects related to stability of possible plasma edge perturbations. This was one of the reasons why a Fourier series description was used, combined with the reduction of the stabilizing effect of the vacuum assumed to surround the plasma, to a term related to the plasma perturbation at the edge. The final term, related to a possible steady-state skin current in the plasma edge, which conventional theory allows for, was shown to be unimportant in the high-n case.

With this approach a theoretical framework was constructed that allows for the analysis of the stability of high-n edge modes that are field-aligned. Although this does represent a restriction of the applicability, it may be expected to be a useful approximation in many cases, as the experiments indeed generally show very good correlation of magnetic perturbations along the field lines. The reduction of the dimensionality to one equiva-

lent to a 2-D system makes a numerical implementation of the problem a doable task from the point of computational resources. For this reason, the theoretical framework was judged to be a good basis for the further work of this thesis.

6.2 The PB3D Numerical Code

Question 2 *What is an efficient way of implementing this stability theory in a numerical code?*

The coupled system of 1-D ordinary differential equations, resulting from the theoretical framework, was used as the focus of a the numerical code PB3D. To solve it numerically the technique of finite differences was used to reduce the differential operators. The resulting system of equations has an algebraic form and can be written as a generalized Eigenvalue equation

$$\mathbf{AX} = \lambda \mathbf{BX} \,, \tag{4.27}$$

where the matrix $\mathbf{A}$ refers to the potential energy perturbation of the plasma perturbation with kinetic energy given by the matrix $\mathbf{B}$. The eigenvector of this system, $\mathbf{X}$, contains the components of the plasma perturbation perpendicular to the flux surfaces, sampled on the numerical grid used, and has as corresponding eigenvalue the square of the complex frequency of the mode: $\lambda = \omega^2$, so that $\lambda > 0$ denotes stability and $\lambda < 0$ instability.

The PB3D numerical code was designed with the goal of efficiency in mind as its intended usage includes parameter scans. It was written in modern Fortran, making use of a number of external libraries that were selected for their efficiency. For example, the HDF5 framework was used for data storage and to provide restart capacity. Furthermore, SLEPC, built on the PETSC framework, was used to numerically solve the generalized eigenvalue equation. And the whole code was parallelized using the technology of MPI, so that it can run on multiple processors.

The equilibrium configurations of which stability is to be calculated are provided through the output of other numerical codes, and PB3D was designed in modular fashion to be able to read both VMEC and HELENA equilibrium data, but this can be extended to other formats. As stated above, it was chosen to store the PB3D output itself in the HDF5 format, so that it can, for example, be post-processed in order to provide visual and numerical output. One of the post-processing capabilities that is worth mentioning is the possibility of reintroducing the solution eigenvector in

the equations in order to gain information about the individual terms of the potential and kinetic energy in a process called *energy reconstruction*.

Finally, PB3D makes use of a numerical technique called *Richardson extrapolation*, which provides successively better approximations to the eigenvalues through the inclusion of more and more discretization points. Furthermore, it yields a way of extrapolating the results for different orders of approximation in order to reduce the discretization errors to still lower orders.

This implementation of PB3D was found to be sufficiently efficient for it to be used smoothly in parameter scans. Furthermore, its modular design allows it to be extended or improved easily in the future.

Question 3 *How does PB3D compare to other codes in terms of verification and validation?*

In order to verify the results obtained by PB3D, two techniques were employed here: checks of physical consistency and comparison with other, established numerical codes. The former kind included assessing the influence of simulation parameters as well as the use of energy reconstruction, while the latter kind referred to comparisons with the 2-D global stability code MISHKA and the 3-D $n \to \infty$ code COBRA. The physical ranges of applicability of these two codes show overlap with that of PB3D: For MISHKA, the equilibrium configurations of which stability is calculated has to be restricted to axisymmetry, and for COBRA only the infinite limit of n can be considered, for modes that do not perturb the edge. The conclusions that could be drawn were positive: The physical consistency tests behaved as expected, and PB3D produces similar stability limits as the other codes, as well as similar mode structures.

The validation issue, on the other hand, would typically involve comparison with experiment. Considering the time scales, this is somewhat outside the scope of this work, so therefore it will happen at a later stage. On a side note, the speed of PB3D is a topic that has been extensively kept in mind during its design, as well as during the implementation. However, detailed optimization is also an issue that is to be addressed afterwards. Here it is also worth repeating that the high-n nature of the perturbations considered, that led to the reduction of the number of dimensions by one, so that the stability could be described by a coupled system of 1-D ordinary differential equations, has a very positive factor on the speed in any case.

6.3 Realistic Application

Question 4 *What is the influence of a toroidal ripple on the stability boundaries of a realistic tokamak, from the ideal linear stability point of view?*

After having designed and created the PB3D code, and after having verified that the results for specified test cases were consistent with physical criteria and other numerical codes, it was time to start working with it on realistic applications. More precisely, it was chosen to focus on one first realistic application as a proof of concept: The influence on stability of toroidal ripple effects. These effects result from the discreteness of the toroidal field coils in tokamaks, which are generally modeled using the assumption of axisymmetry, and are one of the major causes of actual departure from this axisymmetry in reality. Furthermore, it has been observed in reality that, indeed, the ripple size has an influence on the stability–larger than might be expected. This has also been shown in the simulations performed here: Varying the pedestal pressure profile steepness of a typical axisymmetric *high-confinement* (H-mode) case, its stability changed, as steeper pedestals ultimately drove a ballooning mode unstable. Furthermore, pedestal heights that were previously found to be stable in the axisymmetric configurations, could be driven unstable rather easily by applying a ripple to modify the equilibrium in a 3-D way.

It was found that a ripple of only a few percent could decrease the maximum attainable pressure gradient by a factor 30-40%. A similar trend was therefore observed as in the experiments done on the JET and JT-60U tokamaks, which both showed a reduction of about half of the pedestal top pressure height for the case of a strong ripple, compared to the case of a very weak ripple. This served as an indication that the high-n stability indeed plays a role in limiting the maximum attainable pedestal pressure steepness. Also, it hinted at the usefulness of having a tool such as PB3D. Therefore, as a first application, the study of the influence of a toroidal ripple on the high-n pedestal stability was judged a success.

The study of many more consequences of 3-D effects on stability is now possible, thanks to this new numerical tool PB3D, and their importance can be assessed. In section 1.4, some suggestions were already given, that are now repeated here:

Suggestion 1 *Apart from toroidal ripple, what happens with the modification of ideal linear stability by other kinds of 3-D perturbations, such as RMP coils? Specifically, what is the importance of the actual shape of the 3-D modification?*

Suggestion 2 *Are there any extra (un)stable regions of parameter space that exist for 3-D equilibria, similar to the regions defined by peeling and ballooning stability for axisymmetric cases?*

Some final words can be said about these suggestions. To perform the simulations for the study of the influence of a toroidal ripple on the linear ideal edge stability, for example, a new module was created in PB3D, that is able to perturb axisymmetric HELENA equilibria and export them to the 3-D equilibrium code VMEC. Moreover, this module is able to do this for perturbations of general forms. For the study of RMP coils, for example, realistic geometries could be taken into account. This way, it can be investigated whether experimental findings concerning the placement and shape of RMP coils can be observed from theory as well.

Furthermore, VMEC can be run in free-boundary mode, where the shape of the boundary is allowed to be modified. This would lead to even more realistic configurations. PB3D does not have limitations concerning boundary perturbations. The combination of HELENA axisymmetric equilibria with VMEC 3-D perturbed equilibria could be a successful one.

Also, the energy reconstruction functionality of PB3D could be useful to investigate which are the terms that are driving an instability, and how stabilization of instabilities happens through other terms. This way, studies could be designed that, for example, search for the optimal shape of a 3-D perturbation for destabilization.

The next developments of PB3D, as well as information about it, can be found at the project homepage:

`https://pb3d.github.io/`

Curriculum Vitae

30 December 1987	born in Heusden-Zolder, Belgium
2005 – 2008	**Bachelor of science** electrical and mechanical engineering *University of Leuven*
2008 – 2010	**Master of science** energy engineering *University of Leuven*
2010 – 2012	**Master of science** nuclear fusion science and technology (European Erasmus Mundus program) *Ghent University* *Universidad Carlos III de Madrid* *Université de Lorraine*
2012 – 2016	**Doctor of Philosophy (Ph.D.)** (European Doctoral College) *Universidad Carlos III de Madrid* *Eindhoven University of Technology* *ITER Organization*
2017 – 2018	**Post-doctoral researcher** (Monaco post-doctoral fellow) *ITER Organization*

Publications (peer-reviewed)

2014 **Physics of Plasmas** (21.4)

T. Weyens, L. Sánchez, L. García, A. Loarte and G. Huijsmans

3D linear peeling-ballooning theory in magnetic fusion devices

(doi: 10.1063/1.4871859)

2016 **Journal of Computational Physics**

T. Weyens, L. Sánchez, L. García, A. Loarte and G. Huijsmans

PB3D: A new code for edge 3-D ideal linear peeling-ballooning stability

(doi: 10.1016/j.jcp.2016.10.054)

Publications (conferences)

2014 **European Physical Society (EPS)** - Berlin

3-D peeling-ballooning theory in magnetic fusion devices

2015 **American Physical Society (APS)** - Savannah

PB3D: a new code for 3D ideal linear peeling-ballooning stability

2016 **European Physical Society (EPS)** - Leuven

Verifying PB3D: a new code for 3D ideal linear peeling-ballooning stability

References

[And+90] D. V. Anderson et al. "TERPSICHORE: A Three-Dimensional Ideal Magnetohydrodynamic Stability Program". In: *Scientific Computing on Supercomputers II*. Ed. by J. T. Devreese and P. E. Van Camp. Boston, MA: Springer US, 1990, pp. 159–174. ISBN: 978-1-4613-0659-7. DOI: 10.1007/978-1-4613-0659-7_8.

[And+91] D. V. Anderson et al. "The Terpsichore code for the stability analysis of magnetically confined fusion plasmas". In: *Supercomputer* 8.CRPP-ARTICLE-1991-031 (1991), pp. 32–35.

[AW05] G. G. B. Arfken and H. J. Weber. *Mathematical Methods for Physicists*. Academic Press, 2005. ISBN: 9780120598762.

[Bel08] P. M. Bellan. *Fundamentals of plasma physics*. Cambridge University Press, 2008. ISBN: 9780521528009.

[Ber+58] I. B. Bernstein et al. "An Energy Principle for Hydromagnetic Stability Problems". In: *Proceedings of the Royal Society A* 244.1236 (Feb. 1958), pp. 17–40. DOI: 10.1098/rspa.1958.0023.

[BO99] C. M. Bender and S. A. Orszag. *Advanced Mathematical Methods for Scientists and Engineers I: Asymptotic Methods and Perturbation Theory*. Advanced Mathematical Methods for Scientists and Engineers. Springer, 1999. ISBN: 9780387989310.

[Boo05] A. H. Boozer. "Physics of magnetically confined plasmas". In: *Rev. Mod. Phys.* 76 (4 Jan. 2005), pp. 1071–1141. DOI: 10.1103/RevModPhys.76.1071.

[Bra65] S. I Braginskii. "Transport processes in a plasma". In: *Reviews of plasma physics* 1 (1965), p. 205.

[Cha+13] I. T. Chapman et al. "Towards understanding edge localised mode mitigation by resonant magnetic perturbations in MAST". In: *Physics of Plasmas (1994-present)* 20.5 (2013), p. 056101.

[Cha97] M. S. Chance. "Vacuum calculations in azimuthally symmetric geometry". In: *Physics of Plasmas* 4.6 (1997), p. 2161. DOI: 10.1063/1.872380.

[CHT79] J. W. Connor, R. J. Hastie, and J. B. Taylor. "High Mode Number Stability of an Axisymmetric Toroidal Plasma". In: *Proceedings of the Royal Society A* 365.1720 (Feb. 1979), pp. 1–17. DOI: 10.1098/rspa.1979.0001.

[Con+98] J. W. Connor et al. "Magnetohydrodynamic stability of tokamak edge plasmas". In: *Physics of Plasmas* 5.7 (1998), p. 2687. DOI: 10.1063/1.872956.

[Cor82a] D. Correa-Restrepo. "Resistive Ballooning Modes in Three-Dimensional Configurations". In: *IAEA-CN* 3.41 (1982), p. 519.

[Cor82b] D. Correa-Restrepo. "Resistive ballooning modes in three-dimensional configurations". In: *Zeitschrift Naturforschung Teil A* 37 (1982), p. 848.

[Cor99] D. Correa-Restrepo. "Resistive ballooning modes near the edge of toroidal configurations". In: *Physics of Plasmas* 6.2 (1999), p. 530. DOI: 10.1063/1.873197.

[DB03] G. Dahlquist and Å. Björck. *Numerical Methods*. Dover Books on Mathematics. Dover Publications, 2003. ISBN: 9780486428079.

[Deg+97] L. Degtyarev et al. "The KINX ideal MHD stability code for axisymmetric plasmas with separatrix". In: *Computer Physics Communications* 103.1 (June 1997), pp. 10–27. DOI: 10.1016/s0010-4655(97)00037-4.

[DG83] R. L. Dewar and A. H. Glasser. "Ballooning mode spectrum in general toroidal systems". In: *Physics of Fluids* 26.10 (1983), pp. 3038–3052.

[DH98] R. L. Dewar and S. R. Hudson. "Stellarator symmetry". In: *Physica D: Nonlinear Phenomena* 112.1 (1998), pp. 275–280. ISSN: 0167-2789. DOI: http://dx.doi.org/10.1016/S0167-2789(97)00216-9.

[Eva+06] T. E. Evans et al. "Edge stability and transport control with resonant magnetic perturbations in collisionless tokamak plasmas". In: *Nature Physics* 2.6 (June 2006), pp. 419–423. DOI: 10.1038/nphys312.

[FJS10] N. M. Ferraro, S. C. Jardin, and P. B. Snyder. "Ideal and resistive edge stability calculations with M3D-C1". In: *Physics of Plasmas* 17.10, 102508 (2010). DOI: http://dx.doi.org/10.1063/1.3492727.

[Fre08] J. P Freidberg. *Plasma Physics and Fusion Energy*. Cambridge University Press, 2008. ISBN: 9781139462150.

[Fre82] J. P. Freidberg. "Ideal magnetohydrodynamic theory of magnetic fusion systems". In: *Reviews of Modern Physics* 54.3 (July 1982), pp. 801–902. DOI: 10.1103/revmodphys.54.801.

[Fre87] J. P. Freidberg. *Ideal magnetohydrodynamics*. Modern perspectives in energy. Plenum Press, 1987. ISBN: 9780306425127.

[Fri08] A. Fridman. *Plasma Chemistry*. Cambridge University Press, 2008. ISBN: 9781139471732.

[GJ68] J. M. Greene and J. L. Johnson. "Interchange instabilities in ideal hydromagnetic theory". In: *Plasma Physics* 10.8 (Jan. 1968), pp. 729–745. DOI: 10.1088/0032-1028/10/8/301.

[GKP10] Johan P Goedbloed, Rony Keppens, and Stefaan Poedts. *Advanced magnetohydrodynamics: with applications to laboratory and astrophysical plasmas*. Cambridge University Press, 2010.

[GP04] J. P. Goedbloed and S. Poedts. *Principles of Magnetohydrodynamics: With Applications to Laboratory and Astrophysical Plasmas*. Cambridge University Press, 2004. ISBN: 9780521626071.

[Har04] S. Harris. *An introduction to the theory of the Boltzmann equation*. Courier Corporation, 2004. ISBN: 9780486438313.

[HC07] G. T. A. Huysmans and O. Czarny. "MHD stability in X-point geometry: simulation of ELMs". In: *Nuclear Fusion* 47.7 (2007), p. 659.

[Heg14] C. C. Hegna. "Effects of a weakly 3-D equilibrium on ideal magnetohydrodynamic instabilities". In: *Physics of Plasmas (1994-present)* 21.7 (2014), p. 072502.

[Hir83] S. P. Hirshman. "Steepest-descent moment method for three-dimensional magnetohydrodynamic equilibria". In: *Phys. Fluids* 26.12 (1983), p. 3553. DOI: 10.1063/1.864116.

[HM03] R. D. Hazeltine and J. D. Meiss. *Plasma Confinement*. Dover books on physics. Courier Corporation, 2003. ISBN: 9780486432427.

[HN13] P. Helander and S. L. Newton. "Ideal magnetohydrodynamic stability of configurations without nested flux surfaces". In: *Physics of Plasmas (1994-present)* 20.6 (2013), p. 062504.

[HN90] R. D. Hazeltine and W. A. Newcomb. "Inversion of the ballooning transformation". In: *Physics of Fluids B* 2.1 (1990), pp. 7–10. DOI: http://dx.doi.org/10.1063/1.859490.

[Huy05] G. T. A. Huysmans. "ELMs: MHD instabilities at the transport barrier". In: *Plasma Phys. Control. Fusion* 47.12B (Dec. 2005), B165–B178. DOI: 10.1088/0741-3335/47/12b/s13.

[IEA] IEA. "World Energy Outlook 2015". In: (). DOI: http://dx.doi.org/10.1787/weo-2015-en.

[Jac98] J. D. Jackson. *Classical Electrodynamics*. Wiley, 1998. ISBN: 9780471309321.

[Jar10] S. Jardin. *Computational methods in plasma physics*. CRC Press, 2010.

[Ker+98] W. Kerner et al. "CASTOR: Normal-Mode Analysis of Resistive {MHD} Plasmas". In: *Journal of Computational Physics* 142.2 (1998), pp. 271–303. ISSN: 0021-9991. DOI: http://dx.doi.org/10.1006/jcph.1998.5910.

[LL83] Allen J Lichtenberg and Michael A Lieberman. "Regular and Chaotic Dynamics, vol. 38 of". In: *Applied Mathematical Sciences* (1983).

[Loa+14] A. Loarte et al. "Progress on the application of ELM control schemes to ITER scenarios from the non-active phase to DT operation". In: *Nucl. Fusion* 54.3 (Feb. 2014), p. 033007. DOI: 10.1088/0029-5515/54/3/033007.

[Lor75] D. Lortz. "The general "peeling" instability". In: *Nucl. Fusion* 15.1 (Feb. 1975), pp. 49–54. DOI: 10.1088/0029-5515/15/1/007.

[Mac08] D. MacKay. *Sustainable Energy-without the hot air*. UIT Cambridge, 2008.

[Mer60] C. Mercier. "A necessary condition for hydromagnetic stability of plasma with axial symmetry". In: *Nucl. Fusion* 1.1 (Sept. 1960), pp. 47–53. DOI: 10.1088/0029-5515/1/1/004.

[Mik+97] A. B. Mikhailovskii et al. "Optimization of computational MHD normal-mode analysis for tokamaks". In: *Plasma Physics Reports* 23.10 (1997), pp. 844–857.

[Nüh96] C. Nührenberg. "Global ideal magnetohydrodynamic stability analysis for the configurational space of Wendelstein 7–X". In: *Physics of Plasmas (1994-present)* 3.6 (1996), pp. 2401–2410.

[Pea+69] N. J. Peacock et al. "Measurement of the electron temperature by Thomson scattering in tokamak T3". In: *Nature* 224.5218 (1969), pp. 448–490.

[Pre07] William H Press. *Numerical recipes 3rd edition: The art of scientific computing*. Cambridge university press, 2007.

[RBB05] D. Reiter, M. Baelmans, and P. Börner. "The EIRENE and B2-EIRENE codes". In: *Fusion Science and Technology* 47.2 (2005), pp. 172–186.

[Sai+07a] G. Saibene et al. "The H-mode pedestal, ELMs and TF ripple effects in JT-60U/JET dimensionless identity experiments". In: *Nuclear Fusion* 47.8 (2007), p. 969.

[Sai+07b] G. Saibene et al. "Toroidal field ripple effects on H-modes in JET and implications for ITER". In: *Proc. 34th EPS Conf. on Plasma Physics Controlled Fusion (Warsaw, Poland, 2007)*. 2007.

[Sán+00] R. Sánchez et al. "COBRA: An Optimized Code for Fast Analysis of Ideal Ballooning Stability of Three-Dimensional Magnetic Equilibria". In: *Journal of Computational Physics* 161.2 (July 2000), pp. 576–588. DOI: 10.1006/jcph.2000.6514.

[Sch93] C. Schwab. "Ideal magnetohydrodynamics: Global mode analysis of three-dimensional plasma configurations". In: *Physics of Fluids B* 5.9 (1993), pp. 3195–3206. DOI: http://dx.doi.org/10.1063/1.860656.

[Sny+02] P. .B Snyder et al. "Edge localized modes and the pedestal: A model based on coupled peeling-ballooning modes". In: *Physics of Plasmas* 9.5 (2002), p. 2037. DOI: 10.1063/1.1449463.

[Sny+04] P. .B Snyder et al. "ELMs and constraints on the H-mode pedestal: peeling-ballooning stability calculation and comparison with experiment". In: *Nucl. Fusion* 44.2 (Feb. 2004), pp. 320–328. DOI: 10.1088/0029-5515/44/2/014.

[Sta10] W. M Stacey. *Fusion: an introduction to the physics and technology of magnetic confinement fusion*. John Wiley & Sons, 2010.

[Ter00] P. W. Terry. "Suppression of turbulence and transport by sheared flow". In: *Rev. Mod. Phys.* 72 (1 Jan. 2000), pp. 109–165. DOI: 10.1103/RevModPhys.72.109.

[Tur+13] A. D. Turnbull et al. "Comparisons of linear and nonlinear plasma response models for non-axisymmetric perturbationsa)". In: *Physics of Plasmas (1994-present)* 20.5 (2013), p. 056114.

[Tur12] A. D. Turnbull. "Plasma response models for non-axisymmetric perturbations". In: *Nuclear Fusion* 52.5 (2012), p. 054016.

[Ura+06] H. Urano et al. “The roles of plasma rotation and toroidal field ripple on the H-mode pedestal structure in JT-60U”. In: *Plasma physics and controlled fusion* 48.5A (2006), A193.

[Web12] A. J. Webster. “Magnetohydrodynamic tokamak plasma edge stability”. In: *Nucl. Fusion* 52.11 (Nov. 2012), p. 114023. DOI: 10.1088/0029-5515/52/11/114023.

[Wes78] J. A. Wesson. “Hydromagnetic stability of tokamaks”. In: *Nucl. Fusion* 18.1 (Jan. 1978), pp. 87–132. DOI: 10.1088/0029-5515/18/1/010.

[Wey+14] T. Weyens et al. “Three-dimensional linear peeling-ballooning theory in magnetic fusion devices”. In: *Physics of Plasmas* 21.4 (Apr. 2014), p. 042507. DOI: 10.1063/1.4871859.

[Wey+16] T. Weyens et al. “PB3D: A new code for edge 3-D ideal linear peeling-ballooning stability”. In: *Journal of Computational Physics* (2016). ISSN: 0021-9991. DOI: 10.1016/j.jcp.2016.10.054.

[Wil+02] H. R. Wilson et al. “Numerical studies of edge localized instabilities in tokamaks”. In: *Physics of Plasmas* 9.4 (2002), p. 1277. DOI: 10.1063/1.1459058.

[WM99] H. R. Wilson and R. L. Miller. “Access to second stability region for coupled peeling-ballooning modes in tokamaks”. In: *Physics of Plasmas* 6.3 (1999), p. 873. DOI: 10.1063/1.873326.

[Zha11] Zhengqiu Zhang. “An improvement to the Brent’s method”. In: *International Journal of Experimental Algorithms* 2.1 (2011), pp. 21–26.

Index